28
KARLSRUHE TRANSACTIONS
ON BIOMEDICAL ENGINEERING

MARÍA DEL CARMEN MARTÍNEZ ANTÓN

Local Impedance Characterization for Scar and Fibrosis Detection

Towards a New Substrate Assessment for Atrial Mapping

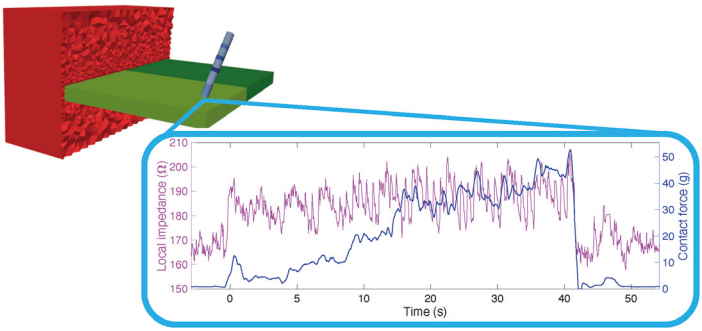

Scientific Publishing

María del Carmen Martínez Antón

Local Impedance Characterization for Scar and Fibrosis Detection

Towards a New Substrate Assessment for Atrial Mapping

Vol. 28
Karlsruhe Transactions on Biomedical Engineering

Editor:
Karlsruhe Institute of Technology (KIT)
Institute of Biomedical Engineering

Eine Übersicht aller bisher in dieser Schriftenreihe erschienenen Bände finden Sie am Ende des Buchs.

Local Impedance Characterization for Scar and Fibrosis Detection

Towards a New Substrate Assessment for Atrial Mapping

by
María del Carmen Martínez Antón

KIT Scientific Publishing

Karlsruher Institut für Technologie
Institut für Biomedizinische Technik

Local Impedance Characterization for Scar and Fibrosis Detection:
Towards a New Substrate Assessment for Atrial Mapping

Zur Erlangung des akademischen Grades eines Doktor-Ingenieurs
von der KIT-Fakultät für Elektrotechnik und Informationstechnik des
Karlsruher Instituts für Technologie (KIT) genehmigte Dissertation

von María del Carmen Martínez Antón, M.Sc.

Tag der mündlichen Prüfung: 25. April 2024
Hauptreferent: Prof. Dr. rer. nat. Olaf Dössel
1. Korreferent: PD Dr. med. Armin Luik
2. Korreferent: PD Dr.-Ing. Axel Loewe

Impressum

Scientific Publishing

Karlsruher Institut für Technologie (KIT)
KIT Scientific Publishing
Straße am Forum 2
D-76131 Karlsruhe

www.ksp.kit.edu

Print on Demand 2024 – Gedruckt auf FSC-zertifiziertem Papier

ISSN 1864-5933
ISBN 978-3-7315-1368-1
DOI 10.5445/KSP/1000171038

Abstract

Atrial fibrillation is a heart condition that causes an irregular and abnormally fast heart rate, as well as a multifactorial and progressive cardiac disease with different manifestations in each patient. The treatment of such illness remains a challenge, especially on those patients showing severe remodelling of the cardiac substrate. Regions of scar and fibrotic tissue have been identified as a potential driving region of arrhythmic activity during AF, so the ablation of these areas represents a standard treatment. High density mapping techniques can provide important information about low voltage and slow conduction zones, both characteristics of arrhythmogenic areas. However, these modalities remain showing discordances in the location and extent of arrhythmogenic areas.

Recently, local impedance (LI) measurements have gained attention as they are expected to distinguish between healthy and scar tissue independently from the atrial rhythm, which can improve the understanding of underlying substrate modifications. A new generation of ablation catheters incorporates the option of LI recordings as a novel technique to characterize the process of lesion formation. To extend this technology towards a mapping system implementation, a better understanding on how different factors are influencing LI measurements is needed. For that, two approaches were followed during this work: *in silico* investigations with different catheters and tissue settings, and *in vitro* experiments to support simulated studies.

By performing *in silico* studies that can relate to commonly seen clinical scenarios, we were able to predict and understand how different factors contribute to measured LI values. A 3D model of the ablation catheters with the DirectSense™ technology was employed in different scenarios reported in the clinics, such as the introduction of the catheter in a steerable sheath, or the variation of the catheter-tissue distance, angle, and force. LI data from recruited

patients at the Städtisches Klinikum Karlsruhe allowed the validation of the simulation setting.

Later, this *in silico* setting was extended to multielectrode catheters. Simulating the impact of several design parameters in LI, such as stimulation and measurement bipolar pairs, inter-electrode distance, or electrode shape and size, tissue conductivities were reconstructed to account for scarred tissue patterns.

Lately, *in vitro* experiments with a mapping catheter were performed built on the previous simulated findings. Various contact impedance recordings in tissue phantom demonstrated statistical significance when comparing the measurements between electrodes in direct catheter-tissue contact and floating in saline.

During this work, the potential capabilities of LI measurements were proven and paved the way towards its use as a surrogate for detection of fibrotic areas in cardiac mapping, complementing commonly used techniques based on electrogram (EGM) analysis.

Zusammenfassung

Vorhofflimmern (VHF) ist eine Herzerkrankung, die eine unregelmäßige und abnorm schnelle Herzfrequenz verursacht. Beim VHF handelt sich um eine multifaktorielle und fortschreitende Erkrankung, die sich bei jedem Patienten unterschiedlich manifestiert. Die Therapie dieser Erkrankung stellt nach wie vor eine Herausforderung dar, insbesondere bei Patienten mit stark verändertem Herzgewebe. Da fibrotisches und vernarbtes Gewebe als potenzielle Auslöser von VHF identifiziert sind, erfolgt die Behandlung standardmäßig durch die Ablation der betroffenen Gewebebereiche. Hochauflösende Kartierungstechniken können wertvolle Informationen über Bereiche mit niedriger Spannung und langsamer Reizleitung liefern, welche beide Charakteristika von arrhythmogenem Gewebe sind. Allerdings zeigt die Analyse dieser Modalitäten Inkonsistenzen bezüglich der Lokalisation und Ausdehnung des arrhythmogenen Gewebes.

Aus diesem Grund hat die Messung der lokalen Impedanz (LI) in letzter Zeit immer mehr an Bedeutung gewonnen. Eine neue Generation von Ablationskathetern bietet die Möglichkeit der LI-Messung als eine neue Methode zur Charakterisierung des Prozesses der Läsionsbildung. Es wird davon ausgegangen, das mit dieser Methode unabhängig vom Vorhofrhythmus zwischen gesundem und vernarbtem Gewebe unterschieden werden kann, wodurch das Verständnis der zugrunde liegende Substratveränderungen verbessert wird. Um ein praktikables Kartierungssystem für diese neue Funktion zu implementieren, benötigt man umfassende Kenntnisse über den Einfluss verschiedener Faktoren auf die LI-Messung. Deshalb wurden in dieser Arbeit zwei Ansätze verfolgt: *in silico*-Simulationen verschiedener Katheter und Gewebeeinstellungen, sowie *in vitro*-Experimente zur Unterstützung klinischer und simulierter Studien.

Durch die Durchführung von *in silico*-Studien, konnten wir vorhersagen und verstehen, wie verschiedene Faktoren zu den gemessenen LI-Werten beitragen. Ein 3D-Modell des Ablationskatheters mit der DirectSense™ Technologie wurde in verschiedenen klinisch relevanten Szenarien eingesetzt. Es wurde beispielsweise die Einführung des Katheters in eine steuerbare Hülle oder die Variation des Abstands zwischen Katheter und Gewebe, des Winkels, sowie der Kraft berücksichtigt. Die Validierung der Simulationen erfolgte anhand von Patientendaten des Städtischen Klinikums Karlsruhe.

Später wurde die *in silico*-Analyse auf die Betrachtung von Multielektrodenkathetern erweitert. Es wurden verschiedene Designparameter von LI, wie bipolare Injektions- und Messpaare, Elektrodenabstand, -form und -größe sowie Katheteranordnung, simuliert, um die Gewebeleitfähigkeiten unter Berücksichtigung fibrotischer Strukturen zu rekonstruieren.

Im nächsten Schritt wurden die *in silico*-Erkenntnisse auf *in vitro*-Experimente übertragen. Es wurden Kontaktexperimente mit einem Multielektrodenkatheter und einem Gewebephantom durchgeführt. Dabei zeigten sich statistisch signifikante Unterschiede in den Impedanzmessungen von Elektroden in direktem Kontakt mit dem Gewebe und ohne Kontakt.

Zusammenfassend wurden mit dieser Arbeit die potenziellen Vorzüge von LI-Messungen demonstriert und dazu beigetragen, den Weg für den Einsatz von LI-Messungen in der Herzkartierung von narbem Gewebe, ergänzend zur Auswertung von Elektrogrammen, zu ebnen.

Resumen

La fibrilación auricular (FA) es una afección cardiovascular que provoca una frecuencia cardiaca irregular y anormalmente rápida, así como una enfermedad multifactorial y progresiva con diferentes manifestaciones en cada paciente. El tratamiento de dicha enfermedad sigue siendo un reto, especialmente en aquellos pacientes que presentan un remodelado severo del sustrato cardiaco. Las regiones de tejido cicatricial y fibrótico se han identificado como una posible región impulsora de la actividad arrítmica durante la FA, representando por ello la ablación de dichas zonas un tratamiento estándar. Las técnicas de mapeo de alta densidad pueden proporcionar información importante sobre las zonas de bajo voltaje y conducción lenta, ambas características de estas zonas impulsoras. Sin embargo, estas modalidades siguen mostrando discordancias en la localización y extensión de las zonas arritmogénicas.
Recientemente, las mediciones de impedancia local (LI) han ganado atención en el campo, ya que se espera que sean capaces de discernir entre miocardio sano y cicatricial independientemente del ritmo auricular, lo que podría mejorar la comprensión de las modificaciones subyacentes del sustrato.

Una nueva generación de catéteres de ablación incorpora la opción de registros LI como técnica novedosa para caracterizar el proceso de formación de la lesión. Para implementar un sistema de mapeo viable que incluya esta nueva función, es necesario comprender mejor cómo influyen distintos factores en las mediciones de LI. Para ello, durante este trabajo se siguieron dos enfoques diferentes: simulaciones con diferentes catéteres y configuraciones tisulares, y experimentos *in vitro* para apoyar los estudios simulados.

Mediante la realización de estudios *in silico* que pueden relacionarse con lo que se observa en la práctica clínica, hemos podido predecir y comprender mejor cómo contribuyen los distintos factores a los valores de LI medidos. Se empleó

un modelo tridimensional de los catéteres de ablación que incluyen la tecnología DirectSense™ en diferentes situaciones clínicas, tales como la introducción del catéter en una vaina orientable o la variación de la distancia entre el catéter y el tejido, el ángulo y la fuerza. Los datos de pacientes reclutados en el Städtisches Klinikum Karlsruhe permitieron la validación del escenario de simulación.

Posteriormente, esta configuración *in silico* se amplió a los catéteres multielectrodo de mapeo. Simulando el impacto de varios parámetros del diseño en la medición de LI, tales como los pares bipolares de inyección y medición, la distancia entre electrodos, la forma y el tamaño de los electrodos o la disposición del catéter, se reconstruyeron las conductividades tisulares para definir los patrones fibróticos.

A continuación, como siguiente paso hacia un sistema de mapeo de impedancia multielectrodo se llevaron a cabo experimentos *in vitro* con catéteres de mapeo basados en los resultados obtenidos de las simulaciones. Experimentos de contacto en fantomas tisulares se realizaron con un catéter circular de mapeo, demostrando significación estadística al comparar las mediciones de impedancia entre los electrodos situados en contacto directo con el tejido y aquellos sin contacto que flotaban en el tanque de solución salina.

Este trabajo aporta nuevos conocimientos sobre el diseño de este sistema de cartografía de impedancia. Durante esta tesis, se demostró el potencial de las mediciones de LI y se allanó el camino hacia su uso como característica de detección de áreas fibróticas, complementando a técnicas más extendidas en la electrofisiología cardíaca como los electrogramas.

Acknowledgments

The chance to work during the last 3.5 years in the Institute of Biomedical Engineering (IBT) at the Karlsruhe Institute of Technology (KIT) really changed my understanding of "team work". The always welcoming and helpful team has made this time remarkably special for me with such an open and collaborative environment.

Firstly, I would like to thank Prof. Dr. rer. nat. Olaf Dössel for giving me the opportunity to pursue my PhD here: The IBT would not be the same without the flexible and trustworthy workplace you established over the years. Thank you for the always on point discussions and the independence you have taught me. I am truly grateful to be the last one of an extensive and productive list of successful PhD graduations. Two years after the "official" retirement, the "true" time to relax has finally come. Of course, additionally I would like to thank PD Dr.-Ing. Axel Loewe for adopting me as part of his team over the past two years and always have an open door for discussions. Thank you for never giving up on me and my fear to talk in public - it was a real pleasure to learn from you.

And of course, all my IBT colleagues also deserve a huge thank you. For the collaboration, fun and laughs, corona experiences, lunch times, conferences, "nappieren-times", and after-work hours in the offices. Many many (x10000) thanks. To Cristian and Paty, for being the best ESpanish ESpeakers I could have chosen to share this experience with. [Aun no saben lo inteligentes (y graciosos) que somos en español, pero lo importante es que nosotros sí lo tengamos muy presente. Gracias por ser los hermanos intercontinentales que me han mantenido a flote, por abrirme a esta visión del mundo y por compartir penas y sufrimientos con el choque cultural. Nunca sabremos si las casualidades existieron, pero qué bonita ha sido]. To Lorena, for making possible the best crazy office combination I could have asked for, always being there for me,

understanding my German no matter what, and agreeing to become a Santa / Beach hacker at any time. To Laura, for being my day-to-day helping hand, the best impedance team leader, the sister I never had, and the best German teacher ever. To Tobi, aka Deutschpolizist, for accepting to move to the hottest and crazy office, having always a shoulder for my tears, and (not less important) restarting my computer at least once a week during my secondments. To Steph, for being my favourite student sharing the best party working nights first, and becoming the best support as PhD baby for the last and most stressful period afterwards. To Joni, for the hugs without asking whenever I needed them, and your never-ending help and support with everything I could need. To Joshi, for the breaks sharing ups and downs of BEING DESTROYED by life and so annoyed by rules. To Miriam, for never giving up with my German and be my "Pony-Haar-Buddy". To Moritz and Silvia, for always having a dark welcoming spot for my power naps and taking care of me when I most needed it. To Ciro and Domenico, - because arriving last does not mean you are less important - for making life at IBT way funnier since you two are around. And all other colleagues and employees who made life at IBT easier and special. I am not forgetting those who shared their best moments at IBT but had to leave for good. To Debbie for still being the wee baby we all need to have around to hug, watch movies, and laugh. To Jorge, for the countless hours we have spent with a mug of coffee saving the world, the happy moments at Casal or staring at Encanto, for your unofficial but incredibly valuable supervision, and always finding my ideas interesting enough to give them a try. [No saber decir que no quizás fue lo que nos hizo ser amigos, pero de esta tarea no me arrepiento.] To Claudia, for always having an open door to comprehension and support and sharing your last IBT moments with the same smile we met at the beginning. To Eki, for being the first person who made life at IBT easier with zumba, ice creams, and German lessons. This work would have not been possible without the fruitful performance of many students through Bachelor's and Master's theses, as well as student research projects: Lena Heinemann, Andreas Heinkele, Nansi Caslli, and Franziska Sophie Stolte. Thanks for allowing me to supervise you, be part of your academic path, and teaching me how to be a better mentor.

However, this thesis would have not be the same without collaboration. First of all, I would like to deeply thank PD Dr. med. Armin Luik for the always open door at the Städtisches Klinikum Karlsruhe. Without your help and dedication, none of this would have been possible. I want to thank the dedicated

support by Annika Haas for always having the time to answer my thousand of clinical questions. And thanks to Carina Jäger for the long explanations about Rhythmia and the patience with the protocols that so much time saved me when she was not around. One day at the hospital was always the most productive electrophysiology lesson and I am sure I will miss that.

This work was supported by the European Union's Horizon 2020 research and innovation programme under the Marie Skłodowska-Curie grant agreement n°860974. I am grateful for the financial support and all the experiences I could live thanks to the PersonalizeAF consortium. Without the 15-players dream team we are now, PhD life would definitely have been tougher. Starting with never-ending online workshops and far-from-home PhD experiences has definitely make us grow in such different ways. Thanks for the laughs, (the tears), the video calls, and the insane amount of trips. Thank you: Marilu, Eric, Sachal, Teresa, Narimane, Victor, Carlos, Albert, Thomas, Özan, Sergio, and Alex. Many thanks also goes to the principal investigators for the fruitful discussions and throughout feedback given over the last years, especially to Prof. Cristiana Corsi, Prof. Blanca Rodríguez, and Prof. María Guillem for being such nice and powerful role models for us. Thanks to the people that share some time with us at IBT or accepted me in their institutions during these years.

A special overseas thanks goes to Dr. Sarah Gutbrod for being my mentor, supervisor, team leader, and friend. You always knew what to say to guide me through research and how to make me feel at home. Thanks to the hard work and infinite patience of Dr.-Ing Tobias Oesterlein for making this experience possible. To the whole R&D Rhythmia Department of Boston Scientific Cardiology in Cambridge/Waltham for being the most friendly environment to develop a critical thinking. And especially to Nili, Amanda, Sowmya, Matt, Thomas, Marianna, Megan, and Rudy for being an "extra safe" space.

And last but not least, thanks to the people that made life in Karlsruhe a little bit sweeter. To Nicole, criaturchen, for always having the dinner ready when I needed "Joey-time". To the JRC-KA Women's Football Team (and Herwin!) for always welcoming me back when I was not in Karlsruhe for 6 months in a row and being such a friendly group to keep my mind far from KIT. Thanks to Martina, Ken, and Richard for sharing a WG at different times during my PhD phase and not running away from my temperamental mood when a deadline or several trips in a row where approaching. [Gracias a Carlota y María, por

llegar en el peor de los momentos y sacarme de casa los días de solete, hacerme reír con los mismos chistes de mierda que haría yo y responder a mis "TÍA." cuando más lo he necesitado.] To the people we met thanks to research and collaboration. Thanks, Rebecca, for being such an amazing friend and making everything so easy. To BSICoS' crew for still making me feel at home no matter where in the world we meet. I would love to thanks my friends and family, but for that to be real [necesitamos cambiar de idioma. Gracias por estar ahí aun sin comprender realmente lo que hago y tener siempre una palabra motivadora que agranda la importancia de este proyecto. No ha sido una experiencia fácil, pero siempre habéis estado ahí en el momento de volver a casa y recargar energías. Gracias Marta por sacarme de viaje, por acogerme en Fallas, por que nada haya cambiado 12 años después. Gracias Danae, Eva, Iris y Laura, por el apoyo en distintos puntos geográficos y perseguirme por el mundo cuando habéis podido. Gracias Alba, Andrea, Cris, Elena, Lola, María, Marta y Vero por escuchar mis locuritas y la comprensión cuando no he llegado a todo. Gracias a Peña la Garza y nuevas aliadas por seguir unidas a pesar de los tiempos. Gracias, Estela y Cris, por seguir haciéndome sentir que no me equivoqué al elegir empezar este camino en BSICoS. Gracias, Comando Zaragoza (Natalia, Iván, Marina's, Elena, Anna, Adrià, Roberto, Álvaro, Raquel, Judit, Cristina) aka segundo Erasmus, por hacer de Boston nuestra casa, hogar, y (especialmente mi) familia elegida.

Y finalmente, gracias Mamá y Papá por todo. La Maripili y el Josean. Por la paciencia cuando la mía se ha visto apagada por el cansancio, por levantar el culo del sofá, dejar la comodidad de los findes Calatayud-Zaragoza y perseguirme por el mundo, y por haber confiado siempre en que podría con esto y más. No sé si después de esto ya será el momento de volver cerca del nido, pero sé que haga lo que haga vais a seguir apoyándome. And last, but not least, to me. Quién te iba a decir a los 15, cuando nada tenía sentido, que encontrarías el camino viviendo en cuatro países en menos de dos años, otros idiomas, pasando muchíííísimas horas (y días) completamente sola, pero siempre iluminada por esa risa y esa actitud de niña ilusionada que tantos problemas te causaba y a la que ahora no te imaginarías renunciar sin dejar atrás tu esencia. Gracias por no tirar la toalla nunca, pero especialmente durante estos oscuros inviernos en soledad, por seguir adelante a pesar de sentirte cada día más perdida, y haber conseguido llegar hasta aquí fuerte y valiente. En tres días cumplimos 30, y terminar esta etapa priorizándote es sin duda el mejor regalo, enhorabuena.]

Contents

Abbreviations

AE	ablation energy 43
AF	atrial fibrillation i, 1, 12 ff., 17 f., 38, 41 f., 55, 79 f., 83, 123
AFlut	atrial flutter 12, 14, 38, 42, 83
AP	action potential 10
AV	atrio-ventricular 11
BT	body temperature 60
Ca^{2+}	calcium 10, 27
CF	contact force . 38, 41–46, 48 f., 80, 82, 84 ff., 88 f., 119
CS	coronary sinus 9, 16, 137
CV	conduction velocity 1, 13, 49
EAMS	electroanatomical mapping system . . . . . 15 f.
ECG	electrocardiogram 15
EGM	electrogram ii, 2 f., 17 ff., 37, 40, 44, 49, 92, 105, 123 f., 134, 151
EIT	electrical impedance tomography 31 ff., 103 ff., 117 ff., 121, 123 f.
EP Lab	laboratory of electrophysiology 14
ETC	electrode-tissue-coverage 43
FTI	Force-Time Integral 38, 43
GI	generator impedance 40, 42
HPSD	high-power and short-duration 42, 46
K^+	potassium 10, 27
kHz	kilohertz . 24, 44, 60 ff., 72, 77, 83, 93, 95, 107, 111 f., 126, 135
KIT	Karlsruher Institut für Technologie 103, 133

LA	left atrium . . . . . 7, 9, 11 f., 15, 41, 43, 47, 83 f.
LAA	left atrial appendage 9
LAT	local activation time . . . . . 17 f.
LGE-MRI	Late Gadolinium Enhancement Magnetic Resonance Imaging 1, 43, 49
LI	local impedance . . . . . i f., 2 f., 19, 32, 37–50, 53–56, 62–78, 80, 82–86, 88 f., 91 f., 95–98, 103 ff., 120 f., 123 f., 128 ff., 133–136, 143, 146, 148, 151 f.
LIPV	left inferior pulmonary vein 7, 9
LSPV	left superior pulmonary vein 7, 9
LV	left ventricle 41, 47
MiFi	IntellaNav MiFi™ OI 39–48
Na^+	sodium 10, 27
NaCl	sodium chloride16, 22 ff., 55, 57 f., 60, 62 ff., 70 ff., 76 f.
PFA	pulse field ablation 42, 45
PV	pulmonary vein 7, 9, 12, 14, 43, 49, 55, 59, 68 f., 75 f., 78, 123
PVI	pulmonary vein isolation 14, 40–43, 47, 80
RA	right atrium . . . . . 7, 9, 11 f., 41, 47
RF	radio frequency . . . . . 37 f., 41 ff., 46, 49, 56
RIPV	right inferior pulmonary vein 7, 9
RSPV	right superior pulmonary vein 7, 9
RV	right ventricle 41, 47
SA	sinoatrial . . . . . 10 f.
StPt	IntellaNav Stablepoint™ 39, 41, 43, 45–48
TMV	transmembrane voltage 10

Chapter 1

Introduction

1.1 Motivation

The prevalence of atrial arrhythmias such as atrial fibrillation (AF) is ca. 60 million cases worldwide, contributing to more than 8 million disability-adjusted life years globally [1]. This heart condition causes an irregular and often abnormally fast heart rate and despite 1% of the population suffering from AF, the treatments remain challenging for those patients with severe remodeling of the atrial tissue.

Currently, the most common treatment for recurring patients is catheter ablation. This intervention consists on the introduction of catheters through the vein in the groin to reach the atria and perform ablation lesions. Systematically, the procedure includes the isolation of the pulmonary veins, although more personalized treatments are becoming the objective. It was recently discovered that arrhythmogenic substrate areas are linked with certain levels of scar and fibrosis developed in the cardiac tissue. Targeting those areas prone to cause ectopic beats or reentry circuits, maintaining the arrhythmia may help characterizing the substrate and improving patient outcomes.

Nowadays, electroanatomical voltage mapping, conduction velocity (CV) mapping and Late Gadolinium Enhancement Magnetic Resonance Imaging (LGE-MRI) are different modalities for characterizing atrial substrate. However, these approaches have different disadvantages, such as electrogram-based features being wave dependent, or toxicity and high costs linked to LGE-MRI.

Previous studies, as the ones carried out by Gunawardene et al. [2] and Segreti et al. [3], have already proven the potential use of local impedance (LI) as a novel approach to characterize atrial myocardium. This novel feature, as well as the impedance drop, can distinguish between areas characterized as low, intermediate, and high voltage, which makes impedance measurements of interest. Althought LI can account for differences in the conductivity of diseased tissue, several confounding factors, such as the effect of other overlapping insulator elements or the intra-patient dependency, must be understood. At the moment, its use has been limited to clinical ablation assessment and thus causing a lack of studies regarding the potential advantages and drawbacks of implementing local impedance measurements as supplementary technique in mapping systems.

1.2 Objective

This work focuses on enhancing LI as a surrogate for atrial substrate towards a better understanding of its potential to complement current existing methods, such as electrogram (EGM)-based substrate mapping. The combination of *in silico* and *in vitro* studies conducted throughout this research opens up the possibility of implementing LI measurements in electroanatomical mapping system technologies thanks to its independence to time changing depolarization patterns.

1.3 Structure of this Thesis

This thesis is structured in several parts. Part I comprises two chapters that provide the reader with the medical and mathematical fundamental knowledge required for comprehending the broader scope of this doctoral thesis. Part II includes Chapter 4, which dives into the topic of LI and reviews the State of the Art of this emerging feature and its use in cardiac electrophysiology.

Starting the innovative part of the topic, this work is organized in three main parts. To begin with Part III, *in silico* LI methods are introduced in three different studies. Firstly, a simulation framework with clinically available ablation catheters was developed and validated with *in vitro* and *in human* experiments to give insights into several influencing factors in Chapter 5. Secondly, the effect

of applying catheter-tissue contact force was evaluated in Chapter 6. In third place, Chapter 7 extends this simulated framework to a multielectrode catheter approach.

The Part IV of this thesis focuses on an *in silico* electrical impedance tomography technique to reconstruct atrial tissue conductivity. Exploring several electrode configurations in a circular catheter setting, this method was employed in *in silico* tissue model in Chapter 8. Lastly, in Chapter 9, the ability of LI to identify non-fully transmural low conductivity areas in comparison to EGM features in an *in silico* framework is demonstrated.

Finally, Part V of this thesis explores the potential of LI as surrogate for atrial substrate using *in vitro* experiments recorded with a clinically available multielectrode mapping catheter in Chapter 10.

To conclude, Chapter 11 describes an outlook for future projects as well as general conclusions derived from the findings of this thesis.

PART I

FUNDAMENTALS

Chapter 2

Medical Fundamentals

2.1 Cardiac Anatomy and Electrophysiology

The heart, located in the mediastinum and slightly to the left of the sternum, serves as the main organ of the human circulatory system. It is a vital organ responsible for pumping blood throughout the body. As depicted in Figure 2.1, the heart is comprised of four chambers – two atria and two ventricles – interconnected by arteries, veins, and valves that ensure the unidirectional flow of blood.

The right atrium (RA) receives deoxygenated blood from the systemic circulation through the superior and inferior vena cava and transfers it to the right ventricle via the tricuspid valve. From there, the right ventricle pumps the blood to the pulmonary circulation through the pulmonary artery, where it is oxygenated in the lungs. The oxygenated blood returns to the left atrium (LA) through the four pulmonary veins (PVs): left superior pulmonary vein (LSPV), left inferior pulmonary vein (LIPV), right superior pulmonary vein (RSPV), and right inferior pulmonary vein (RIPV), as illustrated in Figure 2.2. The blood then passes through the mitral valve and is pumped back to the systemic circulation by the left ventricle through the aorta, distributing oxygen to the cells. This cycle repeats as deoxygenated blood returns to the right atrium [4, 5].

To fulfill its circulatory function effectively, the heart contracts rhythmically. The myocardium, the cardiac muscle, consists of three layers: the subendocardium, the midmyocardium, and the subepicardium. The subendocardium lines the inner surface of the cardiac walls, the subepicardium is the outermost layer [6], and the midmyocardium lies in between both. The endocardium refers to the internal face of the myocardium, whereas the external surface of the heart is known as the epicardium. The myocardium wall thickness varies among the different heart chambers. The left ventricular myocardium wall measures 12-15 mm in thickness [7], the right ventricle wall decreases to 3-5 mm [8], while the atrial wall thickness ranges between 2-5 mm [9].

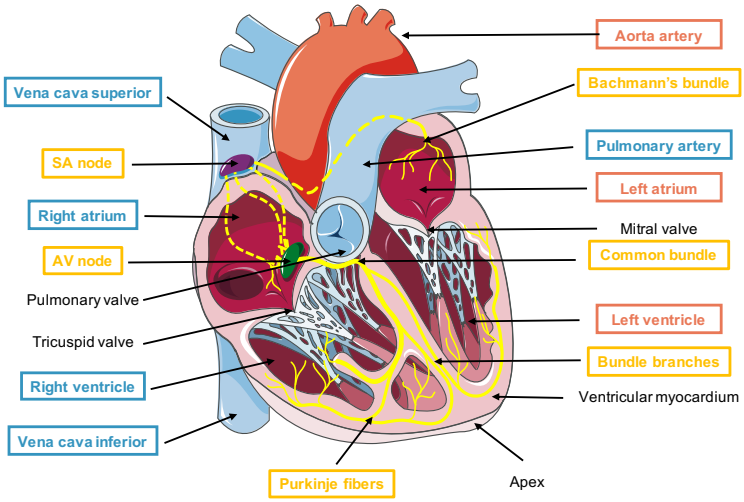

Figure 2.1: Cross-section schematic representation of the human heart anatomy viewed from the anterior position. Left and right atrium, left and right ventricle, the four cardiac valves, and great vessels are labeled in red when carrying oxygenated blood and in blue in the case of deoxygenated blood. Parts involved in the electrical conduction system of the heart are labeled in yellow. Parts of the figure were modified from previously available pictures from Servier Medical Art by Servier, licensed under a Creative Commons Attribution 3.0 Unported License.

2.1.1 Atrial Anatomy

The RA and the LA are separated by the inter-atrial septum, which prevents the mixing of deoxygenated and oxygenated blood. The RA is larger and has thinner walls than the LA. It comprises two parts, the smooth region, which includes the septum and the right atrial appendage, and the rough region formed by the pectinate muscles in the posterior wall [5]. On the posterior wall of the RA, a bundle of small veins converges to form the coronary sinus (CS). The CS serves as a drainage pathway for the blood that has supplied the heart muscle with nutrients and oxygen, playing an important role in cardiac electrophysiology [10].

On the other hand, the LA is often divided into 11 anatomical regions, as depicted in Figure 2.2. The four PVs (RSPV, RIPV, LSPV, and LIPV) transport oxygenated blood from the lungs to the LA. The LA wall is divided into six areas: the roof, septal wall, anterior wall, posterior wall, lateral wall, and inferior wall. Additionally, a small ear-shaped cavity called the left atrial appendage (LAA) is located at the top left of the LA, which is prone to the accumulation of blood clots [11], particularly in people who suffer from heart conditions such as arrhythmias or mitral valve diseases. The thickness of the LA is non-uniform along its wall, becoming thinner as it approaches the LAA [9].

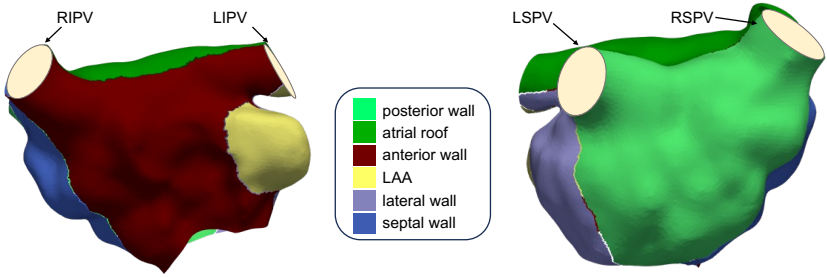

Figure 2.2: 3D representation of the anatomical regions of the LA viewed from the anterior and posterior positions in the left and right panel, respectively. Figure generated from a LA geometry included in the dataset [12] licensed under a Creative Commons Attribution 4.0 International License.

2.1.2 Cardiac Electrophysiology

The so-called cardiac action potential (AP), a special type of electrical signal that travels along a cell membrane as a wave to transmit a signal, initiates the contraction of the cardiomyocytes. Part of these cells, known as pacemaker cells, trigger the electrical impulse that propagates through the excitable cells. The main and primary pacemaker of the heart is the sinoatrial (SA) node, whose cells generate around 80 APs per minute in rest. Adjacent cardiomyocytes are electrically coupled through gap junctions, enabling the propagation of the AP through the myocardium.

Figure 2.3 illustrates the stages of the AP for a myocardial cell. The resting potential, achieved when the cardiomyocytes are not being electrically stimulated, is set at -90 mV (Phase 4) due to the physiological distribution of ions in the intra- and extracellular medium across the cell membrane. It means that the intracellular space is negatively charged in relation to the extracellular space, but ions can move across the membrane through specific ion channels that open and close responding to changes in membrane potential or certain proteins associated with a channel. If a neighbouring cell is depolarized, high amounts of sodium (Na^+) and potassium (K^+) ions flow through , causing an increase in the transmembrane voltage (TMV). When the threshold of -70 mV is reached, fast sodium channels open and Na^+ ions flow into the cell, raising the voltage quickly (Phase 0). These channels will gradually close after the TMV reaches -40 mV. However, there is an overshoot of 20-30 mV due to the opening of the potassium channels, which causes K^+ ions to leave the cell, repolarizing slightly the membrane (Phase 1). The cellular potential forms then a plateau for around 200 ms at 0 mV while calcium channels open and calcium (Ca^{2+}) ions flow towards the intracellular space (Phase 2). This phase is the longest one and unique among excitable cells. As the calcium channels close, the K^+ efflux prevails and the TMV comes back to the resting potential of -90 mV. This is known as the rapid repolarization phase (Phase 3), and together with the plateau phase, it constitutes the period in which the cell is in the absolute refractory period, meaning that no additional electrical stimulus can trigger a new activation regardless of its intensity. [13–17].

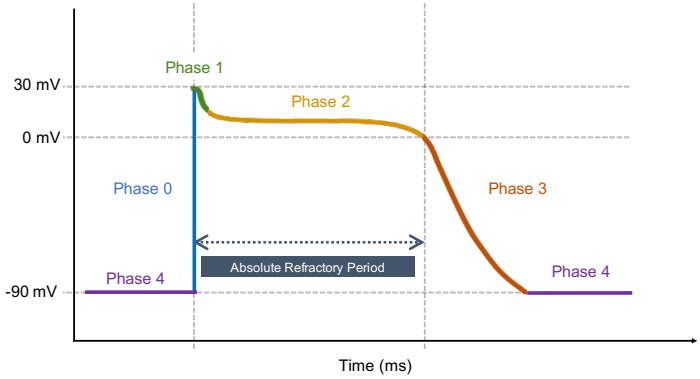

Figure 2.3: Graphical representation of a cardiac AP depicting its phases and the absolute refractory period. Inspired by [18].

2.1.3 Propagation of the Physiological Excitation

The transmission of electrical impulses through the heart ensures coordinated contractions of the myocardium. The process begins at the sinoatrial node in the RA, as shown in Figure 2.1. From the SA node, the impulses propagate across the atria, reaching the Bachmann's bundle part in the LA and causing atrial contraction. Simultaneously, the impulse travels to the atrio-ventricular (AV) node, which briefly delays the signal, allowing the atria to fully contract and fill the ventricles. From the AV node, the electrical signals navigate through the common bundle (or bundle of His) and its branches, rapidly transmitting the impulses throughout the ventricular myocardium, ultimately reaching the Purkinje fibers. [17, 19].

2.1.4 Atrial Arrhythmias

In the previous section, the heart was assumed to function physiologically. Atrial arrhythmias refer to the irregular heart rhythms that originate in the atria. In pathological cases, atrial tissue parameters are altered, resulting in disrupted electrical signals that characterize coordinated cardiac activity and enabling the atria to sustain abnormal heart rhythms. These conditions usually exhibit

a mismatch in contraction rate between the atria and the ventricles, leading to irregular, fast and disorganized electrical activity. Affecting millions of people globally, atrial arrhythmias, including atrial flutter (AFlut) and atrial fibrillation (AF), pose significant implications for cardiovascular health as they can increase the risk of stroke and heart failure. This introduction aims to provide a brief overview of the most common atrial arrhythmias, setting the basics for a deeper exploration of their diagnosis and treatment approaches.

Atrial Flutter

AFlut involves a rapid but still organized electrical circuit around anatomical or structural obstacles, often called reentry circuit and defined as a continuous repetitive propagation of an excitatory wave traveling in a circular path to reactivate the origin site [20]. It results in a regular but often fast heart rate ranging from 240 to 350 bpm. It can be classified as typical or atypical, depending on the location of the reentering conduction loop.
In typical AFlut, the reentry circuit is located in the RA between the inferior vena cava and the tricuspid valve, while atypical AFlut encompasses all other repetitive circuits reentering in both the LA and the RA, including frequent circuits involving the mitral valve or the PVs. This type of arrhythmia is commonly associated with patients who have undergone unsuccessful catheter ablation procedures, and the presence of scar tissue or incomplete lesions contributes to the sustainability of the reentry. [21, 22].

Atrial Fibrillation

AF is characterized by rapid and chaotic electrical activity, leading to an irregular and often fast high rate ranging 180 to 360 bpm. This abnormal rhythm causes highly uncoordinated atrial activation and inefficient atrial contractions. AF is the most prevalent cardiac arrhythmia worldwide, affecting approximately 2% of adults. However, successful treatments for this arrhythmia remain a challenge for both patients and healthcare systems. In contrast to AFlut, AF is typically initiated and sustained by focal triggers within the PVs [23], as well as rotational and multi-wavelet reentrant patterns. The former cause responds to the evidence that PVs are capable of generating reentrant ectopic activity [24].

The latter theory proposes that AF can self-perpetuate by multiple wavelets, which may spatially meander around available atrial tissue [25]. AF can be classified as paroxysmal, with sudden and self-terminating episodes within a week, or persistent, requiring intervention because of its longer duration. [21, 26, 27]. The mechanisms underlying the development and perpetuation of AF are not yet fully understood. Pathophysiological changes in the atria lead to the emergence of an arrhythmogenic substrate, giving rise to abnormal electrical activities such as ectopic foci, reentrant waves, and rotors, as depicted in Figure 2.4. These changes are associated with electrical, structural and autonomic remodeling, which modify the atrial substrate. Atrial fibrosis, a major structural alteration, plays a significant role in the initiation and sustainability of AF. Atrial fibrosis can arise from natural factors like aging or pathological reasons such as chronic inflammation or long-standing atrial arrhythmias. These fibrotic changes facilitate cardiac arrhythmias by creating an optimal substrate for initiating and sustaining reentrant circuits. Fibrotic areas in atrial tissue exhibit decreased electrical propagation due to tissue composition heterogeneity, comprising myofibroblasts and collagen fibers alongside cardiac myocytes in fibrotic cardiac tissue. Atrial fibrosis is classified mainly based on its extent, pattern and distribution. Compact fibrosis is electrically non-conductive but not significantly arrhythmogenic, whereas patchy, interstitial, and diffuse fibrosis can cause reduced conduction velocity (CV) or lead to the formation of unidirectional blocks. [28–31].

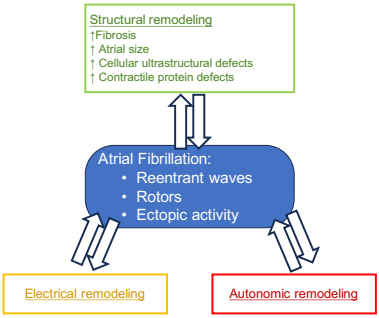

Figure 2.4: Scheme of the main remodeling types affecting AF. In this work we will mainly focus on characterizing the structural remodeling and how it is expressed in the atrial tissue properties.

2.1.5 Treatment Methods for Atrial Fibrillation

Current therapies for AF, classified into pharmacotherapy and ablation procedures, focus on alleviating and reducing symptoms. The patient's age, symptom severity, and presence of underlying heart conditions guide the choice of treatment strategy. Pharmacological treatment involves rate control, like with β-blockers, anticoagulation, rhythm control, and addressing any underlying disorders. Drug therapy aims to achieve cardioversion, maintain sinus rhythm during chronic therapy, and facilitate transformation to AFlut. Antiarrhythmic drug selection for AF considers factors such as safety, efficacy, and costs. Despite medication, AF may persist in some patients, necessitating catheter ablation as further treatment. [28, 32].

Catheter ablation

An ablation procedure is a minimally invasive surgery aimed at halting arrhythmic electrical circuits by creating scar lesions at certain locations on the cardiac tissue. Scar tissue lacks the ability to conduct electrical impulses, thereby impeding the formation of undesirable heart rhythms after the procedure. In AF, the most commonly employed catheter ablation therapy is the isolation of the PVs due to their tendency to host focal triggers [33]. This procedure, known as pulmonary vein isolation (PVI), can be performed using radiofrequency energy to heat up the tissue or a single-shot cryo balloon to freeze it. These two techniques had shown comparable outcomes until now [34, 35]. More recently, pulsed field ablation has emerged as an alternative [36], combining a high frequency train of pulses with a single shot technique.

2.2 Electrophysiological Study

Ablation procedures are carried out inside of the laboratory of electrophysiology (EP Lab), often as part of a longer intervention known as an electrophysiological study, aimed at diagnosing the specific type of arrhythmia beforehand. The medical technology that can be found within an EP Lab is extensive and varied. Figure 2.5 shows how a typical EP Lab is equipped, including an X-ray system to

localize catheters, electrogram displays, an electroanatomical mapping system (EAMS), or the electrocardiogram (ECG) leads on the patient to monitor their electrical activity while being on the operating table.

An electrophysiological study, a specialized medical procedure conducted by cardiologists, involves the insertion of catheters into the heart via the vena femoralis located near the patient's groin, enabling the measurement and mapping of intra-cardiac electrical signals. When access to the LA is required, a transeptal needle punctures the inter-atrial septum, thereby facilitating the placement of diagnostic and mapping catheters with the aid of a steerable sheath. During the study, particularly in cases of substrate-based arrhythmias, the heart's electrical pathways are analyzed. To address this, mapping procedures may precede the intervention to precisely locate any abnormal arrhythmia maintenance circuit. By meticulously identifying the origins of the arrhythmia, electrophysiologists can create a targeted treatment plan.

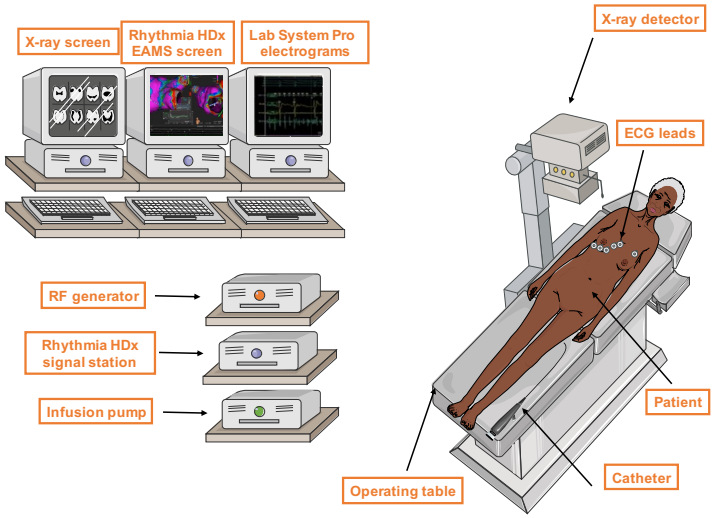

Figure 2.5: Illustration depicting an electrophysiology laboratory, featuring a representative catheter and the three primary screens: an EAMS system, a recording system, and X-ray localization. Parts of the figure were modified from previously available pictures from Servier Medical Art by Servier, licensed under a Creative Commons Attribution 3.0 Unported License.

The typical set of catheters employed in EAMS procedures includes a CS catheter, an ablation catheter such as IntellaNav MiFi™ OI, or IntellaNav Stablepoint™ (Boston Scientific, Marlborough, MA, USA), and a mapping catheter such as the LASSO™ (Biosense Webster, Irvine, CA, USA), the Advisor™ HD Grid (Abbott, Chicago, IL, USA) or the IntellaMap Orion™ (Boston Scientific, Marlborough, MA, USA) (see Figure 2.6). Positioned at the CS ostium, the CS catheter is a linear catheter equipped with 8 or 10 electrodes, providing a stable reference to record the atrial rhythm at a fixed location.

The mapping catheter includes a larger amount of electrodes, commonly configured in settings of 16, 32, or 64 electrode arrays, and arranged in distinct geometric patterns such as flat circular designs (e.g. Lasso, Figure 2.6 (a)), flat grids (e.g. HD Grid, Figure 2.6 (b)), or closed baskets (e.g. Orion, Figure 2.6 (c)). These electrodes are tracked via magnetic or impedance sensors. Using these locations, the endocardial wall can be reconstructed as the convex hull. Additionally, these electrodes capture intra-atrial electrical signals over time, information that is projected onto this shell and color-encoded, resulting in a cardiac chamber geometry commonly referred to as a map. This map serves as a valuable support during ablation procedures involving an ablation catheter.

They are then held at various locations in a stable position with contact to the wall while mapping information is acquired, either manually or by automatic point collection.

Typically in a linear form, the ablation catheter comprises a variable number of electrodes, including optional mini-electrodes like in the IntellaNav MiFi™ OI (Figure 2.6 (d)), or additional features such as force sensors, as seen in the IntellaNav Stablepoint™ (Figure 2.6 (e)), to ensure effective catheter-tissue contact. Once potential arrhythmia-driving regions are identified, the ablation catheter is introduced into the chamber, facilitated by a trans-septal steerable sheath. Such catheter is employed to create lesions with any of the aforementioned techniques. If using radio frequency ablation, an irrigation pump usually flushes sodium chloride (NaCl) solution through the ablation catheter to cool the electrode and avoid overheating the area.

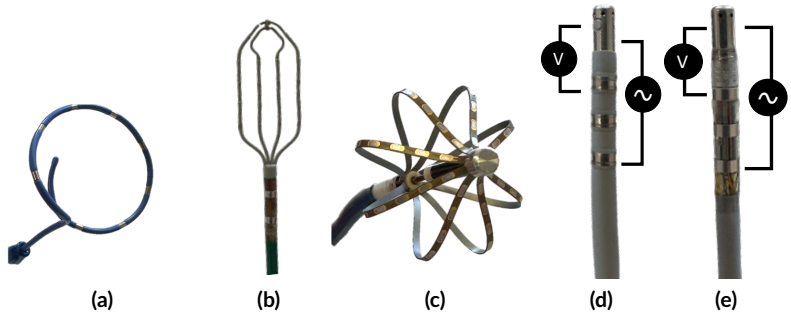

Figure 2.6: Picture of some of the mapping (a-c) and ablation (d-e) catheters available in the market:(a) LASSO™ (Biosense Webster, Irvine, CA, USA), (b) HD Grid (Abbott, Chicago, IL, USA), (c) IntellaMap Orion™ (Boston Scientific, Marlborough, MA, USA), (d) IntellaNav MiFi™ OI (Boston Scientific, Marlborough, MA, USA), and (e) IntellaNav Stablepoint™ (Boston Scientific, Marlborough, MA, USA).

2.2.1 Electroanatomical Mapping

The resulting color-coded representation of the heart chamber's geometry is referred to as a map. In such maps, the information that can be represented is diverse, such as excitation propagation, electrogram (EGM) amplitude, or conduction velocity. Recent progress in the field has led to a shift in the focus towards targeting the underlying atrial substrate responsible for initiating and sustaining AF. In addition to these established maps, there is a growing interest among electrophysiologists in better characterization of atrial substrate.

2.2.1.1 Electrograms

The electrical signal measured at electrodes on intra-cardiac catheters is referred to as EGMs, which can be recorded either in unipolar or bipolar configurations.

Unipolar EGMs are acquired between one single electrode in direct tissue contact with reference to an external electrode at ground potential (or Wilson Central Terminal). Their key advantage lies in their direct assessment of local activation times (LATs); however, they are more susceptible to interference from electrical artifacts. Bipolar EGMs, the most common waveform used

in electrophysiology studies, measure the extracellular potential difference between two adjacent electrode recordings. This technique offers relative insensitivity to remote electrical activity and electrical noise, but their amplitude is strongly influenced by the direction of the wavefront and may sometimes yield flat signals. Moreover, their morphology relies not only on inter-electrode spacing but also on conduction velocity and the direction of fibrillation waves, factors that can substantially differ from beat-to-beat in AF recordings.

Recent years have seen an emerging interest in omnipolar EGMs, stemming from their capacity to transcend the directional dependence of recording electrodes. Computed within a clique [37] that calculates all potential bipolar combinations, omnipolar EGMs determine the difference in amplitude from the most significant bipolar direction. [38, 39].

2.2.1.2 Local Activation Time and Voltage Mapping

Electroanatomical maps visually represent information derived from EGM parameters, including LATs and voltage measurements. In repetitive atrial rhythms, LAT mapping is the standard approach to describe excitation propagation. This method depicts the activation time at each recording point relative to a designated reference, enabling the visualization of activation patterns that can aid in identifying areas of slow conduction. Typically, LATs are calculated from EGMs by selecting the moment when the maximum rate of rise of the transmembrane potential coincides with the steepest negative slope of unipolar EGM. While LAT mapping proves effective when EGMs exhibit a single negative deflection, it may pose challenges when dealing with fractionated signals or multiple electrical interferences.

Voltage maps, widely utilized as well, offer insights into peak-to-peak amplitudes of EGMs across various locations within the atrial tissue. Although both unipolar and bipolar EGMs are influenced by a multitude of variables, low endocardial bipolar voltages are considered as surrogate indicators of fibrotic tissue. These low-voltage areas are increasingly becoming targets for ablation in the context of AF. Existing literature outlines several voltage thresholds associated with scar tissue, such as 0.5 mV, 0.2 mV, or 0.05 mV for posterior left atrial wall, or 0.1 mV for dense scar tissue. However, validation of these thresholds remains difficult, and outcomes of ablation guided by low-voltage

areas exhibit discrepant results, potentially attributed to catheter parameters like inter-electrode distance or electrode size and shape [38].

2.2.2 Local Impedance

EGMs and voltage maps are prone to vary between patients and over time due to their dependency on the propagation wave. As an alternative approach, various technologies have attempted to measure the resistive load at the catheter-tissue interface via impedance, aiming for assessing real-time radio frequency ablation delivery. In the past, radiofrequency generators measured transthoracic impedance by connecting an ablation catheter tip electrode to a reference skin electrode. However, significant impedance variation in the torso through other organs, particularly the lungs, has limited its use as a good measure [40].

The DirectSense™ technology [40], integrated into the Rhythmia HDx electroanatomical mapping system, aims to provide a local impedance (LI) measurement on an ablation catheter without requiring a reference skin electrode. It injects a non-stimulating alternating (5 μA) current at 14.6 kHz between two intra-cardiac electrodes and measures the potential difference between two other intra-cardiac electrodes. The potential field is influenced by the conductive properties of the materials surrounding these electrodes. The so-called LI is calculated using Ohm's Law as the ratio of the measured potential difference to the injected current amplitude, and it is expressed in ohms (Ω).

As of now, only the two ablation catheters manufactured by Boston Scientific (Marlborough, MA, USA) include this technology, although their internal circuits differ. Both circuits are illustrated in Figure 2.6 (d) and (e). The IntellaNav MiFi™ OI employs a four-terminal circuit, where the current is injected from the distal tip electrode to the proximal ring electrode. The voltage is measured between the distal ring electrode and each of the three mini electrodes, resulting in three LI measurements. In the clinical setup, only the maximum value among the three is displayed, as it is considered to be the most likely to be facing the tissue. In contrast, the IntellaNav Stablepoint™ uses a three-terminal circuit where the current is injected from the distal tip electrode and the proximal ring electrode. In this case, the voltage is measured between the distal tip electrode, which is shared with the injection circuit, and the distal ring electrode.

Chapter 3

Mathematical and Technical Fundamentals

The following introduces theoretical knowledge about the technical concepts used in this thesis. It is a summary of the mathematical model of the cardiac electrical properties, electrophysiology and impedance tomography techniques employed in this work.

3.1 Electrical Conductivity and Permittivity

The electrical properties of biological tissue control the interactions between the incident electromagnetic field and the components of biological tissue. The electrical conductivity of tissues, which measures the density and mobility of ions transported in the intra- or extracellular space under an externally applied electric field, plays a crucial role. Additionally, tissue permittivity serves as a measure of the tissue's capacity to store electric energy through electric dipoles [41].

The electrical conductivity σ and the complex permittivity ε express the characteristic response of a material to an externally applied electric field $\boldsymbol{E}$. For anisotropic materials, both σ and ε are tensors with different values in all axes. Throughout this thesis, only isotropic tissue conductivity is considered as first approach to the study of local impedance in atrial tissue characterization, and

thus, both tensors can be reduced to scalar values due to their same value in all directions. The conductivity σ describes the capability of the material to conduct electricity and it is expressed in S/m. The complex permittivity ε reflects the frequency dependency of materials to causally change its polarization [42]. It can be represented by a phase difference that characterizes the capacity to store electrical surface charges and is expressed with the unit F/m. The permittivity of a material ε is usually expressed as the complete expression compound by the relative permittivity ε_r and the permittivity of free space ε_0:

$$\varepsilon = \varepsilon_0 \cdot \varepsilon_{\mathbf{r}}. \tag{3.1}$$

The former associates the electrical field $\boldsymbol{E}$ with the electrical displacement field $\boldsymbol{D}$:

$$\boldsymbol{D} = \varepsilon_0 \varepsilon_{\mathrm{r}} \boldsymbol{E}, \tag{3.2}$$

consisting of a real ε' and an imaginary part ε'':

$$\varepsilon_{\mathrm{r}} = \varepsilon' - \mathrm{j}\varepsilon'', \tag{3.3}$$

with j as the imaginary unit [42–44].

3.1.1 Conductivity of Aqueous Solutions

An aqueous solution consists of deionized water serving as a solvent in which one or more solutes can dissolve, including solids, fluids, or gases. This study particularly focuses on aqueous electrolyte solutions, especially sodium chloride (NaCl) solutions, due to its extended use in irrigation catheters and its similarity to blood plasma [45]. Solutions are characterized by the concentration of the solute i in the solvent. The molar concentration c_i, commonly known as molarity, is expressed as the ratio of the amount of substance n_i to the total volume of the solution V:

$$c_i = \frac{n_i}{V}, \tag{3.4}$$

usually expressed in mol/l or mol/m^3. Alternatively, solutions can be frequently also specified by the mass fraction w_i, which is determined as the ratio of the mass of the solute m_i to the total mass of the solution m:

$$w_i = \frac{m_i}{m}. \tag{3.5}$$

Additionally, the molecular weight M_i relates the mass m_i with the amount of substance n_i as:

$$n_i = \frac{m_i}{M_i}. \tag{3.6}$$

Knowing the molecular weight of a solute i, the solvent, and their respective densities ρ, mass fraction and molar concentration can be computed indistinctly.

The molecular weight of NaCl is given as $M_{NaCl} = 58.44\ g/mol$.

The behavior of these kind of electrolyte solutions is compound by two clearly separate dependencies, as illustrated in Figure 3.1. At low concentrations, the conductivity increases linearly with the concentration. For higher concentrations, the trend changes and the conductivity decreases with increasing concentration. The initial linear increase is caused from an increase in the quantity of ions' availability to conduct current. The decrease in conductivity for higher concentrations may be caused by a lower number of ions available for the transport of current, mainly due to the formation of ions of opposite charge around a central ion or the degree of dissociation that decreases with higher concentrations in weak electrolytes [46].

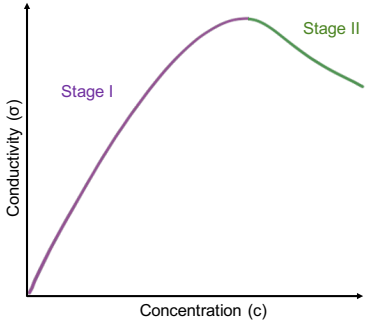

Figure 3.1: Conductivity σ as a function of the electrolyte concentration c. Two separate stages are observed: in purple, a linear increase for low concentrations is followed by a decrease at higher solute concentrations, in green. Inspired by [46].

The *in vitro* experiments explained later in this work were performed at linearly increasing conductivity concentrations (Stage I in Figure 3.1) with increase in concentration.

In addition to the concentration, temperature is also key to the conductivity of the electrolyte solution. Higher temperature causes greater ion mobility, which increases the conductivity. Throughout this thesis, the employed saline solutions are considered to be at body temperature of 35-37 °C. In the specific case of Chapter 5, the conductivity was studied separately and the corresponding temperatures of each sample are specified. The working frequency of the applied electrical field influences the conductivity of the solution as explained by the Debye-Falkenhagen effect [42]. In this work, due to the working frequencies of the catheters and mapping systems studied, only frequencies in the range of kilohertz (kHz) were employed. Thus, the impact of frequencies in the megahertz (MHz) range can be neglected for aqueous NaCl solutions.

3.1.2 Dielectric Properties of Biological Tissue

Simplifying, the human body is compound of cells and the extracellular space, which is the aqueous liquid plus scaffold in between. Their microscopic properties can be modeled in a first approximation as an equivalent circuit with a resistor and a capacitance, depicted in Figure 3.2 and known as the RC circuit [44].

In this equivalence, only the passive electric properties are taken into account and other currents, such as the ones from the ion channels, are not included. Scaling up to the macroscopic perspective, it should be noted that due to the frequency dependence of the dielectric constant of biological tissue, the capacitance C is frequency dependent. Therefore, the equivalent circuit including a constant C is only valid in a limited frequency range. Usually, the impedance has a real part, which is determined through tissue conductivity, and an imaginary part that can be obtained from the permittivity [44].

In Figure 3.3, the model proposed by Cole and Cole [47] is depicted, where the intra- and the extracellular impedance are modeled in parallel. The extracellular impedance is described as a solely resistor R_e, whereas the cellular impedance is represented by a serial combination of an intracellular resistor R_i and the transmembrane capacitance C_m.

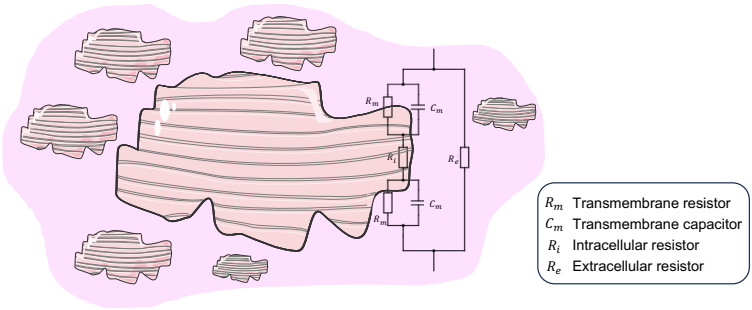

Figure 3.2: Equivalent circuit of the microscopic cellular properties modeled as an RC circuit. R_m, R_i, and R_e are resistors linked to the membrane, intra- and extracelular space, respectively, whereas C_m represents the transmembrane capacitor. Adapted from [44] based on available pictures from Servier Medical Art by Servier, licensed under a Creative Commons Attribution 3.0 Unported License.

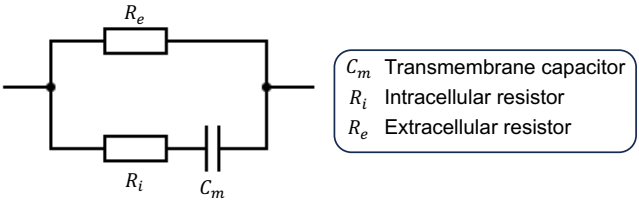

Figure 3.3: Equivalent circuit proposed by Cole and Cole of biological tissue. Reproduced from [47].

Thanks to the measurements taken by Gabriel and Gabriel [48] using different biological tissue samples (see Figure 3.4), dielectric properties of tissue can be expressed depending on the frequency response. Tissue impedance may vary depending on the biological properties, such as in the case of atrial tissue, where for instance the extracellular properties can change due to the increase of fibrosis and thus, impacts on the impedance measured. The direct increase of tissue conductivity with increasing frequency is mainly associated with Maxwell-Wagner effects, and more specifically to the interfacial ionic polarization at the cell membranes. At low frequencies and direct currents, the cell membrane exhibits poor conductivity and the current goes mainly towards

the extracellular space. However, at higher frequencies, the capacitive properties of the cell membrane come into play and the current can also flow through them, causing an increase in conductivity. This phenomenon in known as β-dispersion and results in conductivity and permittivity changes within the frequency range of 1 kHz to several MHz [42].

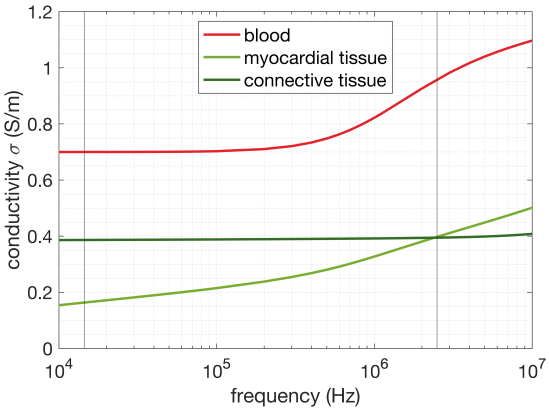

Figure 3.4: Conductivity of blood, myocardial tissue, and connective tissue between 10 kHz and 10 MHz. Vertical lines mark the frequencies used for electrical impedance tomography (EIT) reconstruction in this work $f_1 = 14.5$ kHz and $f_2 = 2.5$ MHz. Figure from [46] with data from [49, 50].

3.2 Cardiac Modeling

3.2.1 Electrophysiology of the Cell

The ionic mechanisms behind an action potential initiation were mathematically described for the first time in 1952 by Hodgkin and Huxley [51]. The authors modeled a giant squid axon as an electrical circuit as the one depicted in Figure 3.5, where the cell membrane represents a capacitor and the ion channels variable conductances in parallel. Some particular ions can cross through ion channels flowing with the electrochemical gradient, which is represented by

voltage sources. Ion pumps, on the contrary, simulate current sources. The difference between the intracellular potential ϕ_i and the extracellular potential ϕ_e constitutes the transmembrane voltage V_m. The transmembrane voltage is determined in the electrical circuit by the addition of all positive and negative currents across the membrane. The membrane current is then the sum of the ionic currents and the capacitive current, as stated in Equation (3.7).

$$I_m = C_m \frac{dV_m}{dt} + \Sigma I_\chi \tag{3.7}$$

where I_m is the total current across the cell membrane, C_m the capacitance of the cellular membrane, $\frac{dV_m}{dt}$ represents the derivative of the transmembrane voltage with respect to the time, and I_χ is the ion current flow for a particular ion species, namely sodium (Na^+), potassium (K^+), and calcium (Ca^{2+}).

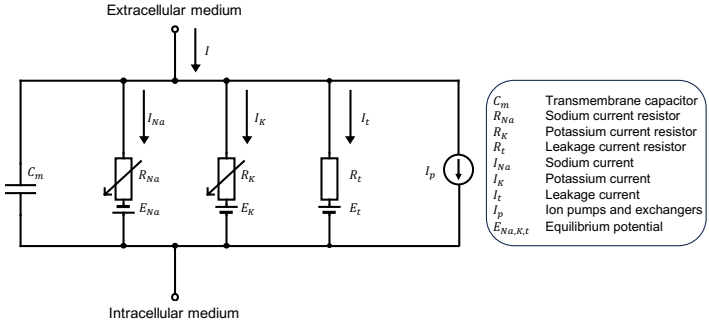

Figure 3.5: Components of Hodgkin-Huxley model representing the electrophysiology of the cell. The cellular membrane is represented by a capacitance C_m, R_{Na} and R_K vary with time and membrane potential, and ion pumps and exchangers are represented by current sources I_p. Leak ion channels are represented by linear terms. Inspired by [51].

In the formulation from 1952, channel conductance is regulated by gates, which can range in state probability of opening between zero and one. Since each cell contains thousands of ion channels, the current flow generated by each ion species through a channel is expressed as stated in Equation (3.8).

$$I_\chi = \bar{g}_\chi \prod_n \eta_n \left(V_m - E_\chi\right) \tag{3.8}$$

where $\bar{g}_\chi$ is the maximum conductance of the given channel, and $\prod_n \eta_n$ the product of all gating variables.

Since Hodgkin and Huxley in 1952, several cellular models of not only atrial [52, 53], but also ventricular [54–56] or human-induced pluripotent stem cell-derived cardiomyocytes [57] have been formulated. In 1998, Courtemanche et al. [52] proposed a specific model for human atrial myocytes which represent the electrophysiological behavior. With nonlinear-coupled ordinary differential equations, the different ionic currents and the transmembrane voltage can be obtained as described in Equation (3.9).

$$\frac{dV_m}{dt} = \frac{-\left(I_{\text{ion}} + I_{\text{stim}}\right)}{C_m} \tag{3.9}$$

where C_m represents the membrane capacity, I_{stim} an optional external stimulus current, and I_{ion} is the ionic current across the membrane calculated as the sum of each single ionic current utilized in the model. A schematic representation of currents, pumps, and exchangers of the model is depicted in Figure 3.6.

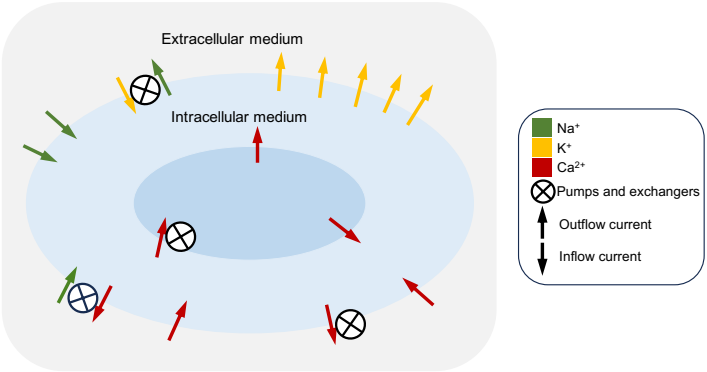

Figure 3.6: Simplified schema of currents, pumps, and exchangers of the Courtemanche model. Arrows indicate currents flow, whose ions involved are color coded meaning yellow, red, and green potassium, calcium, and sodium, respectively. Intra- and extracellular space are depicted in blue and grey, respectively. Inspired by [52].

Each single ionic current can be described by Ohm's law and calculated as the product of the ion channel conductance and an ion specific voltage multiplied by gating variables. These variables are incorporated to describe the open probability of a channel in the cell membrane, which defines whether a specific ion can flow from the extra- to the intracellular space or the opposite. By resolving the ordinary differential equations, an action potential in response to an external stimulus can be obtained through time.

3.2.2 Tissue and Organ Modeling

Courtemanche described a model capable of representing the electrophysiology of a single cell. To describe the excitation and propagation across the cardiac tissue, mono- or bidomain models were proposed.

The bidomain model introduced by Tung et al. [58] represents the most detailed and accurate representation of cardiac excitation propagation on tissue level up to date. It assumes cardiac tissue to be composed of two computational domains, namely the intra- and the extracellular space, which coexist and occupy the same geometrical space. Using Poisson equations, the potentials in either domain can be calculated.

$$\nabla \cdot (\sigma_i \nabla \phi_i) = \beta I_m \tag{3.10}$$

$$\nabla \cdot (\sigma_e \nabla \phi_e) = -\beta I_m - I_{e,s} \tag{3.11}$$

$$I_m = C_m \frac{\partial V_m}{\partial t} + I_{\text{ion}}(V_m, v) - I_{\text{trans}} \tag{3.12}$$

$$V_m = \phi_i - \phi_e \tag{3.13}$$

where ϕ represents the electrical potential, referring the subindices i and e to the intra- and extracellular domain, respectively, σ is the conductivity tensor and β the surface to volume ratio of the cardiac tissue cells. I_{ion} accounts for the total transmembrane ionic current density from the cellular model, which is dependent on V_m and v of further state variables. I_{trans} represents a transmembrane current density stimulus, and $I_{e,s}$ describes external stimuli in the form of

an extracellular current density. As in the previous cellular model, I_m is the total current across the cell membrane and V_m the transmembrane voltage obtained from the difference between the intra- and extracellular space. In the case of modeling a bath surrounding the tissue, this is considered as an extension of the extracellular space. On the other hand, when no external stimulus is applied, the model can be reformulated as in the Equation (3.14) and Equation (3.15) by adding Equation (3.11) and Equation (3.12) and incorporating it into Equation (3.13):

$$\nabla \cdot ((\sigma_i + \sigma_e) \nabla \phi_e) = -\nabla \cdot (\sigma_i \nabla V_m) \tag{3.14}$$

$$\nabla \cdot (\sigma_i \nabla V_m) = \nabla \cdot (\sigma_i \nabla \phi_e) + \beta I_m \tag{3.15}$$

Making this distinction between intra- and extracellular domains is advantageous for computational simulation costs. This bidomain formulation can still be reduced to a monodomain model if anisotropy ratios in both intra- and extracellular domains are assumed to be equal. As the monodomain model was not employed in this work, the reader is referred to [59, 60] for further details.

3.3 Linear Regression

In order to analyze the results of experiments conducted in this thesis, linear regression methods were employed. Linear regression models the relationship between N observations $\boldsymbol{y} = [y_1, y_2, \ldots, y_N]^\top$ and a set of input variables $X = [x_1, x_2, \ldots, x_M]$. Each input feature $\boldsymbol{x}_i$, where $i \in \{1 \ldots M\}$ consists of N samples $\boldsymbol{x}_i = [x_{1i}, x_{2i}, \ldots x_{Ni}]^\top$. Assuming a linear relationship with a measurement error ε, the data set can be expressed as:

$$\boldsymbol{y} = \tilde{\boldsymbol{X}} \cdot \boldsymbol{\alpha} + \varepsilon \quad \text{, with}$$

$$\widetilde{\boldsymbol{X}} = \begin{bmatrix} x_{11} & x_{12} & \ldots & x_{1M} & 1 \\ x_{21} & x_{22} & \ldots & x_{2M} & 1 \\ \vdots & \vdots & \ddots & \vdots & 1 \\ x_{N1} & x_{N2} & \ldots & x_{NM} & 1 \end{bmatrix}, \quad \boldsymbol{\alpha} = \begin{bmatrix} \alpha_0 \\ \alpha_1 \\ \vdots \\ \alpha_M \end{bmatrix}. \tag{3.16}$$

By minimizing the squared deviation of the observed values from the prediction, a least square estimate of $M+1$ coefficients is achieved:

$$\hat{\boldsymbol{\alpha}} = \arg\min_{\boldsymbol{\alpha}} \|\tilde{\boldsymbol{X}}\boldsymbol{\alpha} - \boldsymbol{y}\|_2^2. \tag{3.17}$$

Left multiplying the Moore-Penrose pseudoinverse matrix described in Equation (3.16) yields the solution:

$$\hat{\boldsymbol{\alpha}} = \left(\tilde{\boldsymbol{X}}^\top \tilde{\boldsymbol{X}}\right)^{-1} \tilde{\boldsymbol{X}}^\top \boldsymbol{y}. \tag{3.18}$$

3.3.1 Regularization

Solving Equation (3.18), which represents the solution of a linear regression model, can be challenging due to the ill-conditioned character of $\tilde{\boldsymbol{X}}^\top \tilde{\boldsymbol{X}}$. Incorporating a regularization term that enforces prior knowledge into the solution helps resolving the system of equations. The introduction of a regularization term to Equation (3.17) yields the following for minimization:

$$\|\tilde{\boldsymbol{X}}\boldsymbol{\alpha} - \boldsymbol{y}\|_2^2 + \lambda \|\boldsymbol{\Gamma}\boldsymbol{\alpha}\|_2^2, \tag{3.19}$$

where λ and Γ are the regularization parameter and matrix, respectively. The regularization parameter λ helps balancing minimization of the regularization term and the squared residual norm. The regularization matrix Γ dictates the prior knowledge applied to the solution. Opting for Γ as the identity matrix corresponds to zero-order Tikhonov regularization [61], minimizing the norm of the solution itself. If Γ is chosen as a Laplacian, it is known as second-order Tikhonov or Laplace regularization, minimizing the second-order derivative of the solution. The least-square solution for the model coefficients α is expressed as:

$$\hat{\boldsymbol{\alpha}} = \left(\tilde{\boldsymbol{X}}^\top \tilde{\boldsymbol{X}} + \lambda \boldsymbol{\Gamma}^\top \boldsymbol{\Gamma}\right)^{-1} \tilde{\boldsymbol{X}}^\top \boldsymbol{y}. \tag{3.20}$$

3.4 Electrical Impedance Tomography

Electrical impedance tomography (EIT) is a medical imaging modality which calculates the spatial conductivity distribution of a medium using electrical

measurements on several electrodes placed at the medium boundary. An alternating current at a frequency below the order of MHz is injected through a pair of electrodes while using another pair to measure a potential difference of the potential field ϕ created by the injected current. In this case of having two separate pairs to inject and measure the current, the circuit is a four-terminal circuit. The biggest advantage of four-terminal circuits is the absence of influence on the measurement of the contact impedance between the electrode and the subject. Its main application relies on monitoring the ventilatory state of the lungs utilizing a chest belt in a non-invasive way. EIT represents a hard technique due to the ill-conditioned nonlinear inverse problem that needs to be solved to reconstruct the internal conductivity changes. Its poor spatial resolution is the main obstacle that impedes EIT being extensively adopted in medical clinical applications [42, 62].

Current research in the area aims to enhance EIT reconstruction performance and robustness by means of improving the regularization algorithms. A software package usually employed for this purpose is EIDORS, which has been recently tested also for local impedance (LI) myocardium simulated measurements [63]. The forward and inverse problem of EIT are used in this thesis in different chapters.

3.4.1 Forward Problem of Electrical Impedance Tomography

Computing the potential field Φ for a certain distribution of dielectric properties and known stimulation currents $\boldsymbol{I}$ constitutes the forward problem of EIT. The main equation of EIT's forward problem can be obtained by deriving the Maxwell's and Poisson's equation [44]. The injected current causes an electrical field $\boldsymbol{E}(\boldsymbol{p})$ at each position $\boldsymbol{p}$ and a current density $\boldsymbol{J}(\boldsymbol{p})$ affected by the electrical conductivity $\sigma(\boldsymbol{p})$ and the permittivity $\varepsilon(\boldsymbol{p})$:

$$\boldsymbol{J}(\boldsymbol{p}) = (\sigma(\boldsymbol{p}) + \mathrm{j}\omega\varepsilon(\boldsymbol{p})) \cdot \boldsymbol{E}(\boldsymbol{p}). \tag{3.21}$$

Due to the lack of internal current sources in the used frequency range, the divergence of the current density is zero [64]:

$$\nabla \cdot \boldsymbol{J}(\boldsymbol{p}) = 0. \tag{3.22}$$

Below 1 MHz, the magnetically induced currents are relatively small and the electrostatic case can allow to neglect the temporal derivative of the magnetic field and to express the electrical field as the spatial gradient of the scalar potentials $\boldsymbol{\Phi(p)}$ only:

$$\boldsymbol{E}(\boldsymbol{p}) = -\nabla\Phi(\boldsymbol{p}). \tag{3.23}$$

Combining the previous Equations (3.21), (3.22), and (3.23), the following Laplace equation is derived:

$$\nabla \cdot [(\boldsymbol{\sigma}(\boldsymbol{p}) + \mathrm{j}\omega\boldsymbol{\varepsilon}(\boldsymbol{p})) \cdot \nabla\Phi(\boldsymbol{p})] = 0. \tag{3.24}$$

The complex component of the admittance is relatively small in comparison to the real component in most medical field applications, yielding simplification of Equation (3.24):

$$\nabla \cdot [\sigma(p) \cdot \nabla\Phi(\boldsymbol{p})] = 0. \tag{3.25}$$

Current injection I gives the boundary conditions for the current density $\boldsymbol{J(p)}$ at the precise electrodes location. Solving Equation (3.25) using finite element method taking into account the mentioned boundary conditions yields the scalar potential field $\Phi(\boldsymbol{p})$ [44, 64].

To reduce the incorporation of errors in the model, which may impact significantly medical applications, EIT usually employs conductivity differences $\Delta\sigma(\boldsymbol{p})$ instead of absolute conductivities $\sigma(\boldsymbol{p})$. By taking two measurements at different frequencies or two separated points in time, two different conductivity distributions $\sigma(\boldsymbol{p})$ and $\sigma_B(\boldsymbol{p})$ can be created in practice. These techniques are known as frequency-difference EIT and time-difference EIT depending on the parameter to create the differential computation. Usually, one measurement is considered the background with the underlying background conductivities $\sigma_B(\boldsymbol{p})$ and its potential field $\Phi_B(\boldsymbol{p})$ [44].

Being $\boldsymbol{v} = [v_1, v_2, \ldots, v_M]$ the voltage measurements of M potential differences at M pairs of electrodes, a discrete forward operator $\mathbb{F}$ that maps the conductivity distribution $\sigma(\boldsymbol{p})$ and the current injection I can be defined.

Considering only the first order term of the Taylor expansion of $\mathbb{F}$ can substantially decrease sensitivity to modeling errors, thereby improving the quality of the forward calculation. This first-order linear Taylor approximation of $\mathbb{F}$ is referred to as the Jacobian matrix $\mathbb{J}$:

$$\Delta v = \mathbb{J}\Delta\sigma(\boldsymbol{p}), \tag{3.26}$$

with $\Delta\boldsymbol{v} = \boldsymbol{v} - \boldsymbol{v}_B$ being the voltage change with respect to the background measurement. $\mathbb{J}$ is of dimension $M \times K$ with M being the number of voltage measurements and K the number of discrete positions $\boldsymbol{p}$, i.e. the amount of elements in the defined geometrical model [44].

3.4.2 Inverse Problem of Electrical Impedance Tomography

In medical scenarios, the distribution of conductivities $\sigma(\boldsymbol{p})$ represents the variable to be determined. The given current injection I still serves as the boundary condition. The scalar potential field $\phi(\boldsymbol{p})$ can be evaluated by measuring the potential difference between electrode pairs, followed by solving the inverse problem to reconstruct $\Delta\sigma(\boldsymbol{p})$:

$$\Delta\sigma(\boldsymbol{p}) = \mathbb{J}^{-1} \cdot \Delta\boldsymbol{v}. \tag{3.27}$$

By least-square minimization, $\Delta\sigma(\boldsymbol{p})$ can also be estimated:

$$\Delta\hat{\sigma}(\boldsymbol{p}) = \underset{\Delta\sigma(\boldsymbol{p})}{\arg\min} \|\Delta\boldsymbol{v} - \mathbb{J} \cdot \Delta\sigma(\boldsymbol{p})\|_2^2. \tag{3.28}$$

With the help of the Moore-Penrose pseudoinverse described in Equation (3.18), Equation (3.27) can be resolved. A regularization term as described in Equation (3.19) is usually of need.

PART II

STATE OF THE ART

Chapter 4

A Review of an Emerging Atrial Tissue Characterization Method

Since the first release of DirectSense™ in 2018, a total of 159 results are found in PubMed, 133 in Scopus, and 68 in Web of Science when searching for local impedance (LI). After discarding abstracts or conference publications that were later extended to full journal papers, a final number of 71 studies were taken into account for this review. This chapter serves as an extension of the introduction given through previous chapters to this novel technique.

4.1 Introduction

Radio frequency (RF) catheter ablation is a widely adopted approach for treating cardiac arrhythmias. However, achieving deep, durable, and non-conductive ablation lesions, both in atrial [65] and ventricular [66] myocardium, poses a considerable challenge, often leading to a notable number of patients undergoing repeat procedures [67–69].

Moreover, identification of regions with pathologically altered substrate has emerged as a potential means to find good locations to apply these lesions [70, 71]. Currently, monitoring of intra-cardiac electrograms (EGMs) and derived mapping techniques, such as voltage maps, are employed to estimate the location of fibrotic areas [72, 73]. However, these techniques are subject

to variation between patients and over time due to their dependency on the electrical propagation wave [74, 75].

The use of electrical impedance measurements has a long history in the medical field, including the electrophysiology laboratory [76]. Past research has demonstrated that various biological tissues exhibit distinct impedance spectra [48], a characteristic attributed to their microscopic composition [42]. As an alternative approach, several technologies have attempted to measure the resistive load at the catheter-tissue interface using electrical impedance, providing real-time assessment of RF ablation delivery [77, 78].

Past attempts at measuring transthoracic impedance by connecting an ablation catheter tip electrode to a reference skin electrode had limited reliability [79–81], mainly due to significant impedance variation in the torso caused by current flowing through other organs, particularly the lungs. As a result, this method was not deemed a reliable measure.

In recent times, other parameters such as Force-Time Integral (FTI) or contact force (CF) have been employed to monitor catheter-tissue contact during ablation procedures [82]. While FTI serves as a marker of lesion success, its utility is constrained by the exclusion of power delivery. Similarly, CF measures the force between the catheter tip and myocardial tissue during mapping and ablation, with optimal CF being crucial for accurate data acquisition, lesion formation, and procedural safety [83]. Ongoing efforts, including the integration of CF, power, and time during RF delivery, aim to enhance the prediction of lesion creation [84].

More recently, impedance measurements have gained attention as another modality for substrate assessment in atrial conditions such as atrial fibrillation (AF) and atrial flutter (AFlut), as they do not rely on the dynamically changing electrical activity of the heart [85, 86]. The DirectSense™ technology [40] (Boston Scientific, Marlborough, MA, USA), integrated into the Rhythmia HDx electroanatomical mapping system (Boston Scientific), aims to provide an impedance measurement on an ablation catheter without the need for a reference skin electrode. This technology injects a non-stimulating alternating current of 5μA at 14.6 kHz between two intra-cardiac electrodes and measures the potential difference locally. The potential field is influenced by the conductive properties of the materials surrounding these electrodes. The resulting feature, known as LI, is calculated using Ohm's Law as the quotient

between the measured potential difference and the injected current amplitude, and it carries the unit ohm (Ω).

Currently, two tip ablation catheters (Boston Scientific), namely the IntellaNav MiFi™ OI (MiFi) and the IntellaNav Stablepoint™ (StPt) , incorporate this technology with slight differences in their circuits. The MiFi catheter [40], depicted in Figure 4.1 (a), uses a four-terminal circuit, where the current is injected from the distal tip electrode to the proximal ring electrode. The voltage is measured between the distal ring electrode and each of the three mini electrodes, resulting in three LI measurements simultaneously. In the clinical setup, only the maximum value among the three is displayed, as it is considered the most likely to be facing the tissue. In contrast, the StPt catheter [87], illustrated in Figure 4.1 (b), uses a three-terminal circuit where the current is injected between the distal tip electrode and the proximal ring electrode. In this case, the voltage is measured between the distal tip electrode, which is shared with the injection circuit, and the distal ring electrode.

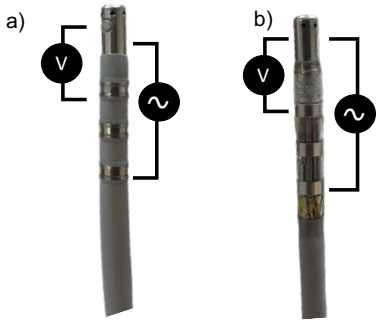

Figure 4.1: Picture of the clinically available ablation catheters including LI capability. The injection (V) and measurement (∼) electrode circuits are depicted in either catheter: (a) IntellaNav MiFi™ OI (Boston Scientific, Marlborough, MA, USA), and (b) IntellaNav Stablepoint™ (Boston Scientific, Marlborough, MA, USA).

Earlier review studies have explored LI to monitor radiofrequency ablation lesion formation [78, 88]. However, as of the submission of this manuscript and to the best of the authors' knowledge, the consideration of LI for mapping the arrhythmogenic substrate has not been addressed in any scientific review paper.

The objective of this work is to consolidate the existing knowledge from various studies in the field, providing insights into the potential future applications of this innovative technology in cardiac electrophysiology, with a specific focus on its utility for mapping arrhythmias.

4.2 Local Impedance in Ablation Performance

In contrast to transthoracic generator impedance (GI), LI highlights local changes in tissue impedance while demonstrating reduced susceptibility to far field artifacts [2, 3, 89, 90]. A drop in LI, resulting from resistive tissue heating, myocardial destruction, and subsequent lesion creation, serves as a robust indicator of effective lesion formation [40, 89]. While increased susceptibility to local surroundings compared to GI, LI remains responsive to the three-dimensional arrangement of materials and their properties around the catheter [91].

To ensure catheter-tissue contact in multielectrode devices without contact force, various impedance-based systems [92, 93] have been developed. In the MEIS system, acting as a middle step between GI and LI, an electrical field is locally created with minimal influence from the lungs, and voltage is measured through a skin patch. However, it remains a transthoracic measurement, limited by patient-specific factors such as body size, fluid status, or changes in lung volume [80, 89].

Martin et al. [90] reported in their first clinical use of the MiFi catheter a lower LI in dense scar than either healthy tissue or bloodpool. An exponential relationship between LI value and maximum EGM amplitude ($0.53 < r_m < 0.75$) was found, whereas the correlation between GI and EGM amplitude resulted very weak ($0.11 < r_m < 0.33$). Primarily explored during pulmonary vein isolation (PVI), LI served as a surrogate to improve lesion durability and predict successful lesions [94].

In clinical practice, LI is mainly represented by its drop, expressed as absolute difference (ΔLI) or percentage value (%ΔLI). Beyond PVI, superior vena cava isolation was also studied while guided by LI [95], where ΔLI was also reported greater than ΔGI. ΔLI and %ΔLI in the left chambers, i.e. left

ventricle (LV) and left atrium (LA), were higher in successful lesions. Median ΔLI was 16 Ω and 14.6 Ω in successful lesions on LV and LA, respectively, compared to 9.4 Ω and 6.8 Ω in non-successful lesions [90]. Accordingly, %ΔLI yielded 17.1% and 14.2% in effective lesions on LV and LA, respectively, against 10.6% and 7.5% in non-sufficient lesion areas. In a similar way, Pesch et al. [96] observed differences in median baseline LI among all four chambers: 107.5 Ω, 100.7 Ω, 100.5 Ω, and 104.6 Ω, in the LA, LV, right atrium (RA), and right ventricle (RV), respectively.

According to some studies, ΔLI was the most important predictor of acute lesion block [97, 98] and it correlated strongly with lesion size and depth but not width [99]. However, higher correlation with lesion size [100] and steam pop prediction has been reported when using %ΔLI instead of ΔLI [101].

Catheter contact angle (CA) considerably influences LI, dropping faster during RF ablation if the catheter is not in a perpendicular position with respect to the tissue [102]. Even in cases where a CF module is not included, LI can assist in ensuring suitable catheter-tissue contact. At different monitored CFs, LI demonstrated a positive correlation with CF and lesion depth, diameter, and volume [103]. Mean CF and baseline LI predicted ΔLI as a surrogate of lesion formation, with the highest ΔLI in high-voltage and high-baseline LI areas [104]. To avoid steam pops, the LI drop cutoff at several CF values was found to be 46 Ω [103].

The use of LI has been investigated in clinical trials, namely the LOCALIZE trial [89, 105], and the CHARISMA study [106–109]. In the LOCALIZE trial, focused on de novo PVI in paroxysmal AF patients using the Direct Sense™ technology, the MiFi catheter was exclusively used. The CHARISMA study, which included patients treated with various ablation catheters, encompassed the use of both the MiFi and the StPt.

Regional differences in optimal ΔLI were reported within the LOCALIZE trial in correlation with the thickness of the wall [89, 105, 110]. Thinner posterior and inferior walls showed optimal ΔLI cutoff values of 18.3 Ω and 14.2 Ω, whereas thicker anterior and roof regions required greater ΔLI of 21.8 Ω and 16.9 Ω, in [110] and [105], respectively. Depending on the ablation location, the best ΔLI and %ΔLI cutoffs were 20 Ω and 11.6%[111] for PVI, whereas 12 Ω and 21 Ω, and 11.6% and 10.8% during cavotriscupid isthmus ablation using MiFi [112] and StPt [113], respectively.

One published study within the CHARISMA trial combined LI and CF to evaluate acutely successful ablation applications. Researchers reported that aiming for higher CF increased the likelihood of achieving optimal LI, consequently reducing RF delivery time when combined with the target CF ($5 < \mathrm{CF} < 40\,g$) [108]. The same clinical trial reported a 12% recurrence rate in 153 AF and AFlut patients who underwent LI-guided catheter ablation with the MiFi catheter after a 1-year follow-up [109].

LI has demonstrated its utility in monitoring RF lesion gaps [106]. An ΔLI of 13.4 Ω, with a 4 mm inter-application distance and 20 s of RF ablation duration, may predict complete PVI using a MiFi catheter. The ΔLI was more prominent than a ΔGI at ablation points without a gap, and GI was not correlated with LI [114].

LI also emerges as a surrogate to guide cardiac ablation, optimizing RF delivery by offering real-time insights into lesion formation. RF duration required to achieve an effective lesion was inversely related to LI measured before RF delivery [115] and ΔLI [116]. Studies by Kawano [117] indicated that deep and wide lesions are predominantly created during the rapidly increasing phase of the ΔLI. To perform shorter ablations, authors suggested aiming for a duration shorter than the 90% decay time of ΔLI [117]. In the context of high-power and short-duration (HPSD) ablation delivery techniques, LI may facilitate achieving more transmural lesion formation than low-power settings [118]. However, in combination with CF, a power setting of 40 W may represent a better balance between safety and efficacy, as high-power delivery may lead to steam pops [119]. Combining LI with CF showed a significant reduction in RF delivery time at standard power, yielding an optimal ΔLI between 20 Ω and 65 Ω for creating sufficient lesions without excessive heating. Additionally, catheters combining CF and LI were associated with a higher recurrence-free survival rate than standard irrigated catheters [120], with the improvement more related to LI presence than the CF feature. Comparative analysis of ablation guidance features, including LI, CF, and fluoroscopy, indicated a substantial reduction in ablation time for the LI group. Furthermore, LI-guided ablation proved to be as successful and safe as other well-established ablation procedures [121, 122].

Beyond RF ablation, ΔLI before and after ablation performance was studied in cryoablation [123] and pulse field ablation (PFA) cases [124]. In cryoablation, successful PVI lesions showed a ΔLI greater than 17 Ω. Similarly, in a PFA case report, the mean ΔLI was 27.5 Ω, representing a 70% greater drop in PFA

compared to RF reported by Solimene et al. [109]. However, both cases were isolated case reports, necessitating further clinical trials to extrapolate their results.

Comparing ablation outcomes between the two LI-capable catheters, the MiFi and the StPt [101], both proved equally safe. However, the StPt catheter produced larger lesions, and in general, %ΔLI showed a higher correlation with lesion size and prediction of steam pops. Optimal cutoff values %ΔLI of 30.8% and 27.1% with the MiFi and the StPt, respectively, predicted steam pops with equal accuracy.

When combined with more conventional parameters such as ablation energy (AE), FTI [125], or electrode-tissue-coverage (ETC) [99], LI may offer a stronger correlation with lesion characteristics. Despite not being included in other lesion metrics, some studies found that catheter angle showed a higher correlation with LI drop than CF [126].

4.3 Local Impedance in Substrate Mapping

Beyond monitoring ablation lesion formation, LI exhibits potential in characterizing cardiac tissue and distinguishing between healthy myocardium and fibrotic or scar tissue [2, 3, 90]. Before LI was introduced, Pedrote et al. [127] explored already in 2008 the use of impedance to acquire full chamber maps through the use of a skin patch. A homogeneous and constant impedance gradient from the deep pulmonary veins (PVs) to the LAs was reported for all patients. While LI is not as widely used for mapping as it is for assessing effective lesion formation, researchers have explored its potential in characterizing cardiac substrate by means of LI distinguishing among cardiac chambers [96]. Unlike the use of techniques such as voltage maps or Late Gadolinium Enhancement Magnetic Resonance Imaging (LGE-MRI), LI mapping shows potential advantages, such as independence of the current rhythm (i.e. true substrate mapping), and independence of wavefront direction.

Two comprehensive studies acquired full-chamber maps, in the atria [128], as well as in the ventricles [129]. The atrial study recorded 14 point-by-point LI maps in de-novo and redo PVI patients, revealing LI variations across atrial regions correlated with low, intermediate and high voltage areas. In the ventricular study on pig models of ventricular tachycardia, low LI (defined as $\geq$

1 Ω lower than blood pool) was detected in 100% of low voltage areas, while intermediate LI (ranging between low LI and non greater than blood pool value +9 Ω) was found in core and border zone in 87% and 12.5%, respectively.

Several years earlier, Amorós et al. [130] tested a multifrequency approach (1-1000 kilohertz (kHz)) to study systolic-diastolic myocardial impedance in a healed myocardial infarction pig model. Lower LI measurements were observed in the healed myocardial infarcted tissue, representing the first use of a novel bioimpedance method potentially applicable in catheter-based devices for fibrotic tissue detection during arrhythmia mapping. A subsequent study by the same group [131], also using multifrequency impedance mapping, demonstrated the recognition of atrial infarct scar areas with less data variability than local bipolar voltage mapping.

Regarding voltage mapping, the debate persists on whether to map during sinus rhythm or during an arrhythmic episode [132]. Bates et al. [133] explored pacing thresholds based on LI and electrical activity, finding that scar was not electrically inert and should potentially be ablated. Low voltage areas were linked to LI values of 10.5 Ω, whereas 0.5 Ω corresponded to dense scar zones. Additionally, in [134], LI was correlated with CF depending on the rhythm. Recording LI at optimal catheter-tissue coupling controlled by CF in sinus rhythm and atrial fibrillation showed that LI was rhythm-dependent. The evaluation of fibrotic tissue using bipolar voltage did not affect the relationship between CF and LI, but it was impacted when assessed by bloodpool LI.

Using three-dimensional models of both ablation catheters, several confounding factors of LI were studied *in silico* [63]. The authors reported LI traces in clinically relevant scenarios, such as the variation of catheter-tissue distance and angle. The changes in LI from direct catheter-tissue contact to an insertion of the MiFi catheter 2 mm inside of the tissue ranged from 14 Ω to 33 Ω, which compared well to clinically observed mean ranges [128] of 16 Ω to 20 Ω. The combination of LI and CF has also been instrumental in studying the relationship with myocardial tissue thickness *in vitro* [135] and *in silico* [136], potentially aiding in creating transmural lesions for more successful arrhythmia treatment. *In silico* studies have also assessed the comparison between EGM-derived voltage maps and LI maps [137]. In a preliminary study, the LI inverse simulations yielded better reconstruction of the non-transmural fibrotic tissue than voltage maps.

Table 4.1: Summary of publications studying LI during catheter ablation.

	Cath	Study type	Findings	Ref
Lesion assessment	MiFi	Clinical (n=31)	Lower LI in dense scar	[90]
	Both	Clinical (n=1,15,102)	Conduction gap detection by LI and ΔLI	[106, 111, 114]
	Both	Clinical (n=60,48)	ΔLI correlated with conduction block	[89, 98]
	MiFi	Clinical (n=153)	After 1 year follow-up 12% recurrence rate	[109]
	StPt	*in vivo* canine	Chronic block with ΔLI ranging 23-34 Ω	[115]
	StPt	*ex vivo* porcine	Bloodpool LI> 160 Ω increased steam pops	[100]
	StPt	Clinical (n=30)	CA, CF, and baseline LI linked with ΔLI	[97]
	StPt	Clinical (n=15)	Perpendicular CA causes higher ΔLI	[126]
	Both	*ex vivo* porcine	Lesion width and ΔLI smaller at 90°	[102]
	StPt	Clinical (n=20)	Mean CF and baseline LI predicted ΔLI	[104]
	StPt	Clinical (n=40)	Combined CF-LI catheters improved recurrence-free rate	[120]
	MiFi	Clinical (n=1)	ΔLI> 17Ω after cryoablation	[123]
	MiFi	Clinical (n=1)	ΔLI was more pronounced with PFA than thermal ablation	[124]

Table 4.1 - continued form previous page. LAPWI: left atrial posterior wall isolation. RFDT: radio frequency delivery time. AW: anterior wall. SW: superior wall. IW: inferior wall. PW: posterior wall.

	Cath	Study type	Findings	Ref
RF optimization	MiFi	Clinical (n=10)	HPSD yields more transmural lesions	[118]
	StPt	*ex vivo* swine	Wattage crucially affects ΔLI	[119]
	StPt	*in vivo* canine	Inverse relation between initial LI and RFDT	[115]
	StPt	Clinical (n=45)	CF and ΔLI inversely correlated with RFDT	[116]
	StPt	CHARISMA trial	50W LAPWI guided by LI succeeded 93.3%	[97]
	StPt	*ex vivo* swine	RFDT<90% decay time of the ΔLI is preferable	[117]
	MiFi	Clinical (n=30)	LI-guided group showed reduced RFDT	[121]
	MiFi	*in vivo* canine	LI-guided ablation yielded minimal extra damage	[122]
	StPt	Clinical (n=212)	Good CF with an adequate LI reduced RFDT	[108]

Table 4.1 - continued form previous page. LAPWI: left atrial posterior wall isolation. RFDT: radio frequency delivery time. AW: anterior wall. SW: superior wall. IW: inferior wall. PW: posterior wall.

	Cath	Study type	Findings	Ref
LI optimization	StPt	Clinical (n=102)	Best LI and %ΔLI cutoffs 20 Ω and 11.6%	[111]
	MiFi	Clinical (n=50)	Best LI and %ΔLI cutoffs 12 Ω and 11.6%	[112]
	StPt	Clinical (n=50)	Best LI and %ΔLI cutoffs 21 Ω and 10.8%	[113]
	MiFi	Clinical (n=58)	ΔLI cutoff 16.9 Ω and 14.2 Ω on AW,SW and PW,IW	[105]
	StPt	Clinical (n=8,212)	Best ΔLI $>$ 21 Ω and $>$ 18 Ω on AW and PW	[108, 110]
	MiFi	Clinical (n=73)	LI at LV, LA, RA, and RV were 107.5 Ω, 100.7 Ω, 100.5 Ω and 104.6 Ω	[96]
	StPt	*in vivo* swine	20Ω $<$ ΔLI$<$ 65Ω resulted in effective yet safe lesions	[87]
	StPt	Clinical (n=45)	LI$<$ 25 g affects ΔLI	[116]
	MiFi	Clinical (n=15)	ΔLI 13.4 Ω, 4 mm lesion distance and 20 s duration closed PVI	[114]
	MiFi	*ex vivo* swine	Not exceeding ΔLI of 46 Ω avoided steam pops	[103]
	MiFi	*ex vivo* swine	Not exceeding %ΔLI of 30.8% avoided steam pops	[101]
	StPt	*ex vivo* swine	Not exceeding %ΔLI of 27.1% avoided steam pops	[101]

Table 4.2: Summary of publications studying LI as mapping feature. The use of "Both" as system refers to MiFi and StPt. VT: Ventricular Tachycardia.

	Cath	Study type	Findings	Ref
Point-by-point	Both	Clinical (n=40)	0.5 Ω and 10.5 Ω defined dense scar and low voltage area thresholds	[133]
	StPt	Clinical (n=20)	CF and rhythm affected bloodpool LI	[134]
	StPt	Clinical (n=20)	CF-LI relationship was affected by atrial fibrosis	[134]
	MiFi	Clinical (n=14)	ΔLI correlated with high, intermediate and low voltage areas	[128]
	StPt	Animal (swine)	Simultaneous LI-CF can estimate myocardial thickness	[135]
	StPt	*in silico*	Simultaneous LI-CF can estimate myocardial thickness	[136]
	Own	Animal (swine)	Fibrotic degree is correlated with local decrease in LI	[130]
	Own	Animal (swine)	Multifrequencial LI mapping outperformed voltage recognizing scar	[131]
	MiFi	Animal (swine)	LI mapping associated with VT inducibility	[129]
	Both	*in silico*	LI cofounding factors analyzed towards its mapping use	[63]
	Lasso	*in silico*	Sequential LI outperformed voltage detecting non-transmural fibrosis	[137]

4.4 Research Gaps and Potential Future Developments

Electrical impedance has long been considered in electrophysiology, but its widespread clinical implementation took place with the release of LI as a key feature for lesion assessment. In contemporary practice, LI primarily serves in assessing effective lesion formation, with a focus on durable lesions prediction. The scientific publictions related to LI in ablation performance and lesion characterization are summarized in Table 4.1, categorized by the study's objectives.

Nowadays, inconsistencies in atrial substrate detection among well establish mapping methods, i.e. voltage mapping, conduction velocity (CV), and LGE-MRI, still exist [138]. Statistically significant variations in LI recorded with ablation catheters, distinguishing healthy myocardium from scarred and fibrotic areas, prompted exploration of LI as another potential mapping feature. Table 4.2 consolidates published studies investigating LI's mapping capabilities and key findings.

Overall, the usage of LI feature may add valuable information while guiding ablation, which often translates in shorter and less powerful ablation deliveries. However, the potential drawbacks of its application remain underexplored. In Nakamura et al.'s study [139], the incidence and characteristics of postablation silent cerebral events (SCEs) were compared between ablation index-guided ablation with CARTO (Biosense Webster) and LI-guided ablation with Rhythmia. The latter group exhibited a significantly higher SCE incidence, but caution is warranted in generalizing these results due to differing materials used between the two groups, such as ablation and mapping catheter, electroanatomical mapping system, and sheath

Similarly, Lyan et al. [140] assessed the efficacy of lesion size index versus LI-guided ablation, revealing differences in ablation time and PV gaps. However, the use of distinct ablation catheters and systems with varying CF and RF delivery devices may contribute to these disparities.

Explorations into LI mapping in patients have showcased its potential to complement classical mapping based on EGMs [128]. Moreover, other technologies measuring local dielectric properties include wall thickness estima-

tion [141], which could add important value when using LI to assess ablation lesions.

Yet, challenges persist, with studies noting drawbacks like the frequency range used by the Direct Sense™ technology in point-by-point acquisitions for constructing full chamber maps [128]. Despite concerns, LI-based methods have been especially explored as innovative approaches, such as different frequency measurements [130, 131].

4.5 Conclusion

This study provides a comprehensive review of a novel method for characterizing myocardial tissue based on local electrical impedance measurements. The local electrical impedance and its drop have demonstrated their efficacy as good lesion formation predictor, in *ex vivo* and *in vivo* studies, as well as in various clinical trials. While the application of LI in mapping is not as widespread as its use in ablation assessment, several studies have explored its ability to distinguish between healthy and diseased myocardium. By consolidating the most relevant findings from *ex vivo*, clinical, and *in silico* studies in the field, this review highlights the potential complement that LI represents to voltage mappings for improved ablation outcomes in the future.

PART III

AN *IN SILICO* ELECTRICAL IMPEDANCE FRAMEWORK

Chapter 5

In Silico Study of Local Impedance Measurements in the Atria

In this chapter, an *in silico* environment for the two clinically available tip ablation catheters including local impedance (LI) measurements is presented. This serves the purpose to study several influencing factors that impact LI measurements in the clinics without a known ground truth.

The content of Chapter 5 was previously published under the CC-BY license in IEEE Transactions on Biomedical Engineering [63]. The study was firstly explored by Laura Unger, and the following concept was discussed and improved simultaneously by both authors. The first geometrical model setup was developed by Laura Unger, whereas the sheath and the second catheter were modeled by the author of this thesis. The conceptualization of the in vitro experiments were developed by Laura Unger and carried out by both authors. Diverse subsections of the results were presented by either author, as well as the development of figures. Overall, decisions in the implementation of the code and subsequent improvements were discussed by both. Its content has been rephrased with the consent of Laura Unger.

5.1 Introduction

The use of electrical impedance measurements has a long history in the medical and biomedical field. Past studies have demonstrated that several biological tissues exhibit distinct impedance spectra [48], a characteristic attributed to their microscopical composition [42]. Not only the material composition and the measurement frequency, but also the arrangement of electrodes and temperature significantly influence the recorded impedance value.

Various technologies have attempted to measure the resistive load at the catheter-tissue interface using generator impedance measurements, which have been an established method for evaluating real-time radio frequency ablation delivery for decades in the past [77, 142]. The transthoracic impedance encountered by the radio frequency energy between an intracardiac catheter electrode and a reference skin electrode helps identifying catheter-tissue contact during ablation. However, significant impedance variation in the torso through other organs, particularly the lungs, has limited its use as good measure [79, 80] and hinders thorough tissue characterization in the surroundings of the catheter tip.

Recently, two novel intra-cardiac catheters manufactured by Boston Scientific (Marlborough, MA, USA) were released to the market including a more locally focused impedance recording. These two catheters have all injecting and measuring electrodes built into the ablation catheter itself [142], although their circuits differ. The IntellaNav MiFi™ OI [40] employs a four-terminal circuit, where the current is injected from the distal tip electrode to the proximal ring electrode. The voltage is measured between the distal ring electrode and each of the three mini-electrodes, resulting in three LI measurements per recording. In the clinical setup, only the maximum value among the three is displayed, as it is considered to face towards the tissue directly. In contrast, the IntellaNav Stablepoint™ [87] uses a three-terminal circuit where the current is injected from the distal tip electrode and the proximal ring electrode. In this case, the voltage is measured between the distal tip electrode, which is shared with the injection circuit, and the distal ring electrode. The DirectSense™ technology [40], integrated into the Rhythmia HDx electroanatomical mapping system, provides an LI measurement. An LI drop, caused by a combination of resistive tissue heating and subsequent myocardial destruction and lesion formation, serves as an indicator of lesion quality and durability [40, 89].

In comparison to the transthoracic generator impedance, the LI highlights more local changes in tissue impedance and it is less sensitive to far field artifacts [2, 3, 89, 90]. Even though the local surroundings have a greater impact on the LI measurement in comparison to the generator impedance, the LI is still affected by materials' three-dimensional arrangement and their specific properties [91]. It is important to note that LI should not be confused with lumped impedance measurements, which condense all influencing properties to an infinitesimal element. Beyond monitoring ablation lesion formation, LI has demonstrated potential in characterizing cardiac tissue and distinguishing between healthy myocardium and fibrotic or scar tissue [2, 3, 90]. Given the significant impact of atrial fibrillation (AF) as the most common sustained cardiac arrhythmia on both patients and global health care systems, and considering the suboptimal success rates of current treatment approaches, innovative tissue characterization methods like LI are warranted further exploration.

Expanding the diagnostic utility of intracardiac LI measurements encounters significant challenges posed by several confounding factors. These factors include not only diverse tissue compositions but also variables such as the distance and angle between the catheter and the tissue, the geometric characteristics of surrounding tissues, potential overlap of the catheter with the transseptal sheath, or the influence of sodium chloride (NaCl) solution irrigation, among others. While some of these effects have been observed in *in human* studies, their quantification remains challenging due to the complex overlay of multiple factors and the absence of a clear ground truth. Although *in vitro* and *ex vivo* experiments can provide insights into different scenarios, they come with significant costs and, depending on the experimental setup, may leave the underlying ground truth still underdetermined.

In this study, we introduce a highly detailed *in silico* framework modeling the IntellaNav MiFi™ OI and the IntellaNav Stablepoint™ catheters combined in several clinically relevant scenarios. Several artifacts, such as the effect of the distance and angle in catheter-tissue contact, the presence of scar tissue, the insertion of the catheter into a pulmonary vein (PV), the overlap with a transseptal sheath, and the impact of NaCl solution irrigation, were studied and validated with *in vitro* and *in human* measurements.

Including a highly detailed comparison between two real ablation catheter geometries, as well as the investigation of confounding factors that affect clinically relevant scenarios, this work sets the ground for a less expensive im-

provement in the comprehension of intra-cardiac LI measurements and future development of cardiac catheters.

5.2 Methods

5.2.1 *In Silico* — Geometrical Setup

Clinically available radio frequency (RF) ablation catheters which include LI measurements, namely the IntellaNav MiFi™ OI and the IntellaNav Stablepoint™, were modeled as illustrated in Figure 5.1 (a-d). Highly detailed models with a resolution below 100 µm were achieved using measurements extracted from the specific product specification sheets [143, 144] and calibrated photographs.

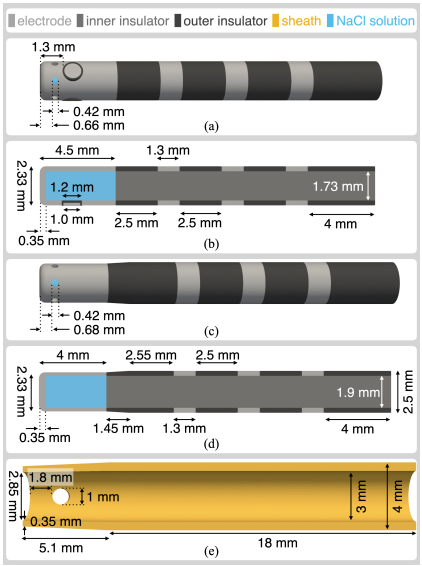

Figure 5.1: Geometrical models of both RF ablation catheters including an LI module and a transseptal sheath: (a) 3D model and (b) cross-section of the IntellaNav MiFi™ OI, (c) 3D model and (d) cross-section of the IntellaNav Stablepoint™, (e) cross-section of a transseptal sheath including one of the two irrigation holes. Image taken with permission from [63].

The IntellaNav MiFi™ OI, as shown in detail in Figure 5.1 (a-b), is composed of a 4.5 mm tip electrode, three ring electrodes of 1.3 mm width with 2.5 mm spacing between them, three equally distributed mini-electrodes of 0.8 mm diameter immersed in the tip electrode, a cooling chamber that stores the NaCl solution, and six irrigation holes. The inside of the catheter includes electrical and mechanical steering wires. However, as the inside is electrically isolated from the electrodes, the interior of the modeled catheter shaft was filled with insulating material.

Similarly, the IntellaNav Stablepoint™ comes with a 4 mm tip electrode, three ring electrodes of 1.3 mm width each and 4 mm, 2.5 mm, and 2.5 mm spacing between them, respectively. Additionally, six irrigation holes and a cooling chamber filled with NaCl solution are included. In this case, the tip does not incorporate any embedded mini-electrodes Proximal to the tip, the diameter increases in a conical way from a diameter of 2.33 mm until reaching a shaft diameter of 2.5 mm. The force sensing spring [87] existing in the interior of the tip of the catheter was neglected as it was assumed to be irrelevant for the spread of the electrical field into the tissue. Thus, the interior of the modeled catheter shaft was filled with insulating material as well. Detailed measures of its geometry are shown in Figure 5.1 (c-d).

A transseptal sheath was also modeled based on the 8.5 F Agilis™ NxT steerable introducer (Abbott, Chicago, IL, USA) as illustrated in Figure 5.1 (e).

Either catheter was embedded in a box spanning 140 mm $\times$ 140 mm $\times$ 140 mm as depicted in Figure 5.2 (a) filled with either blood or NaCl depending on the simulation setup. Geometry representation and tetrahedral meshing was performed in Gmsh (version 4.5.6) [145]. Mesh resolution was adapted to the size of local structures being the highest at the IntellaNav MiFi™ OI mini-electrodes, surrounding the tip and close to the tissue surface, while it decreased for larger distances to the catheter and reached the lowest at the outer boundary of the surrounding box. Depending on the simulation setup, 2.5 million to 5 million tetrahedral elements comprised the mesh.

Standardized NaCl Solutions

In this simulation setup, either catheter was introduced in the surrounding box filled with NaCl solution of eight different molar concentrations beginning with 0.02 $\frac{\text{mol}}{\text{l}}$ until reaching 0.09 $\frac{\text{mol}}{\text{l}}$ in steps of 0.01 $\frac{\text{mol}}{\text{l}}$.

Tissue

Within a surrounding box filled with blood, a squared patch of tissue measuring 110 mm × 110 mm × 2.5 mm resembling a piece of atrial myocardium of typical wall thickness [146] was placed below either catheter, as depicted in Figure 5.2 (a). As seen in Figure 5.2 (b), the distance between the catheter and the tissue d_T was varied from −2 to 10 mm in steps of 0.5 mm. In this case, negative distances describe an immersion of the catheter into the tissue represented as replacement of the tissue by the catheter without mechanical interaction modeled.

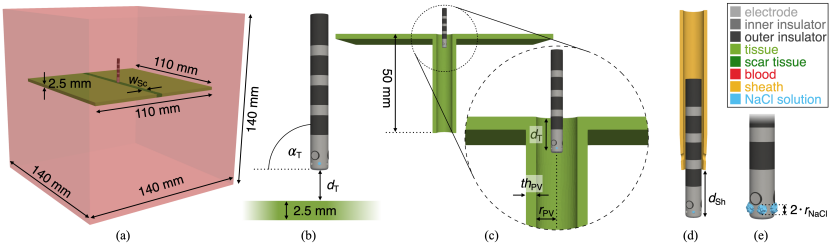

Figure 5.2: Simulation setups. All setups are depicted at the example of the IntellaNav MiFi™ OI and were equally conducted with the IntellaNav Stablepoint™: (a) tissue patch with line of scar within the surrounding blood box, (b) variation of distance and angle between catheter and tissue, (c) insertion of the catheter into the PV, (d) insertion of the catheter into the transseptal sheath, (e) irrigation with NaCl solution. Image taken with permission from [63].

In a second setup, the angle α_T between either catheter and the tissue was varied from 0° to 180° in steps of 15°. For those angles $90° < \alpha_T \leq 180°$, one of the mini-electrodes faced directly towards the tissue. Contrarily, for angles $0° \leq \alpha_T < 90°$, the two remaining mini-electrodes were pointed towards

but not directly at the tissue, as it can be observed in Figure 5.2 (b). The pivot point was located at the intersection of the catheter's distal plain and the outer wall of the catheter shaft at the left and right side, respectively. The simulations were conducted for five different distances between catheter and tissue $d_T \in \{0.0\,\text{mm}, 0.5\,\text{mm}, 1.0\,\text{mm}, 2.0\,\text{mm}, 4.0\,\text{mm}\}$.

Transmural Lesion

Complementing the general tissue setup described above, a central line of scar tissue of width $w_{Sc} \in \{3\,\text{mm}, 6\,\text{mm}\}$, as depicted in Figure 5.2 (a), was implemented representing damaged tissue from a previous ablation procedure or naturally developed myocardial scar. Either catheter was moved for two different catheter-tissue distances ($d_T = 0\,\text{mm}$ and $d_T = 1\,\text{mm}$) perpendicularly to the line of scar starting at a distance to the center of the scarred line of $d_{Sc} = -10\,\text{mm}$, crossing the line for $d_{Sc} = 0\,\text{mm}$ and up to a distance of $d_{Sc} = 10\,\text{mm}$ at a step size of 1 mm for $|d_{Sc}| > 2\,\text{mm}$ and 0.5 mm for for $|d_{Sc}| < 2\,\text{mm}$.

Pulmonary Vein

Either catheter was introduced into a PV simulated by extending the tissue setup with a perpendicular tube filled with blood. Using a PV wall thickness $th_{PV} = 2\,\text{mm}$, four different inner PV radii $r_{PV} \in \{2\,\text{mm}, 3\,\text{mm}, 4\,\text{mm}, 6\,\text{mm}\}$ were modeled. For $r_{PV} = 6\,\text{mm}$, extra PV wall thicknesses of $th_{PV} \in \{1\,\text{mm}, 3\,\text{mm}, 4\,\text{mm}\}$ were implemented in the simulations. Either catheter was inserted into the PV with the variable distance d_T to the surface of the tissue patch varied from −20 to 10 mm in steps of 1 mm. Negative distances represent the catheter being inside the PV while positive distances describe its elevation above the tissue.

Transseptal Steerable Sheath

Either catheter was placed in a surrounding box filled with blood and withdrawn into the transseptal sheath with the variable distance d_{Sh} representing the distance between the catheter tip and the distal edge of the sheath, as seen in Figure 5.2 (d). d_{Sh} was varied from −2 to 19.5 mm in steps of 0.5 mm, where negative distances describe the withdrawal of the catheter into the sheath.

Irrigation

Catheter irrigation was modeled by placing a sphere of physiological NaCl solution at the center of each irrigation hole, as seen in Figure 5.2 (e), and displacing encircled elements representing blood. The radius r_{NaCl} of each NaCl sphere was modified from 0 to 2 mm in steps of 0.05 mm.

5.2.2 *In Silico* — Material Properties

The tetrahedral elements of the mesh were assigned characteristic conductivity values for the respective material at 14.5 kilohertz (kHz) as described in Table 5.1 together with the employed temperature found in the corresponding study.

In vitro experimental setups with several concentrations NaCl solutions were performed at different temperatures and compared to *in silico* investigations based on the conductivity values described by Gabriel et al. [48], which did not specify the temperature at which the experiments were carried out. Comparing to the conductivity of 0.5% NaCl solution given for 20 °C [147] suggests that Gabriel et al. used a slightly higher temperature T_{Gab}, as included in Table 5.1. Taken into account the reference values [147] and the temperature coefficient of approximately 2.1 $\frac{\%}{^{\circ}\mathrm{C}}$ [148], Gabriel et al. most likely measured NaCl solutions significantly below body temperature (BT) contrary to their measurements of biological tissue. Since their dataset [48] was consistent in itself, the exact temperature employed was assumed to be negligible for the validation setups with NaCl solutions of different concentrations.

The remaining simulations setups were parameterized with given conductivities for blood, myocardium and scar tissue at BT, as well as physiological 0.9% NaCl solution for catheter irrigation at an approximate room temperature of 20 °C as explicitly described in Table 5.1. Due to the lack of an explicit reference for the conductivity of physiological 0.9% NaCl solution, it was interpolated from the values of 0.5% and 1% NaCl solution at 20 °C [147] as indexed in Table 5.1.

Table 5.1: Conductivities of relevant materials at 14.5 kHz used in this work. BT: body temperature; T_{Gab}: temperature used in Gabriel et al. [48].

Material	**Conductivity σ (S/m)**	**Temperature (°C)**	Reference
Metallic electrode	400,000		[149]
Insulator	10^{-7}		
Sheath	10^{-7}		
Blood	0.700	BT	[49, 50]
Myocardium	0.164	BT	[49, 50]
Connective tissue (scar)	0.387	BT	[49, 50]
NaCl 0.020 $\frac{\text{mol}}{\text{l}}$ (0.12%)	0.220	T_{Gab}	[48]
NaCl 0.030 $\frac{\text{mol}}{\text{l}}$ (0.18%)	0.330	T_{Gab}	[48]
NaCl 0.040 $\frac{\text{mol}}{\text{l}}$ (0.23%)	0.430	T_{Gab}	[48]
NaCl 0.050 $\frac{\text{mol}}{\text{l}}$ (0.29%)	0.530	T_{Gab}	[48]
NaCl 0.060 $\frac{\text{mol}}{\text{l}}$ (0.35%)	0.620	T_{Gab}	[48]
NaCl 0.070 $\frac{\text{mol}}{\text{l}}$ (0.41%)	0.720	T_{Gab}	[48]
NaCl 0.080 $\frac{\text{mol}}{\text{l}}$ (0.47%)	0.800	T_{Gab}	[48]
NaCl 0.086 $\frac{\text{mol}}{\text{l}}$ (0.50%)	0.820	20	[147]
NaCl 0.090 $\frac{\text{mol}}{\text{l}}$ (0.53%)	0.880	T_{Gab}	[48]
NaCl 0.154 $\frac{\text{mol}}{\text{l}}$ (0.90%)	1.444	20	
NaCl 0.171 $\frac{\text{mol}}{\text{l}}$ (1.00%)	1.600	20	[147]

5.2.3 *In Silico* — Impedance Forward Simulation

To simulate the spread of the electrical field created by the Rhythmia HDx electroanatomical mapping system (Boston Scientific, Marlborough, MA, USA) used in the clinics, an alternating current of 5 µA peak-to-peak amplitude at 14.5 kHz was modeled using the software EIDORS v3.10 [150] in MATLAB R2021a (The MathWorks, Inc., Natick, MA, USA). In short, this software solves the Poisson equation with a finite element model F. The injection currents are given as boundary conditions, whereas the current density and the potential field are the solution. The extracted voltage between two electrodes v is obtained as the potential difference and depends on the given conductivities $\boldsymbol{\sigma}$ at the elements of the model and the stimulation pattern $\boldsymbol{q}$ of the electrode model with $v = F(\boldsymbol{\sigma}, \boldsymbol{q})$ [150].

Both the stimulation and measurement circuits were modeled according to the clinical system of each catheter: a four-terminal circuit and three-terminal circuit for IntellaNav MiFi™ OI and IntellaNav Stablepoint™, respectively. For the IntellaNav MiFi™ OI, current injection was implemented between the distal

tip electrode and the proximal ring electrode, whereas the measurements were taken between the mini-electrodes and the distal ring electrode [40]. The three resulting voltage measurements were reduced to their maximum value as done in the clinical system. On the other hand, the IntellaNav Stablepoint™ followed a three-terminal circuit with current injection between the distal tip electrode and the proximal ring electrode and voltage measurements taken between the distal tip electrode and the distal ring electrode. The complete electrode model was used [151]. To obtain LI as the magnitude of impedance, the resulting voltage amplitude $|v|$ was then divided by the amplitude of the injected current.

5.2.4 *In Vitro* Setup

All experiments were conducted using the Rhythmia HDx system (Boston Scientific, Marlborough, MA, USA) and both catheters, namely the IntellaNav MiFi™ OI, and the IntellaNav Stablepoint™. NaCl solutions of several concentrations and known conductivity values σ were mixed to validate the simulation framework. The molar mass starting from 0.02 $\frac{\text{mol}}{\text{l}}$ up to 0.09 $\frac{\text{mol}}{\text{l}}$ in steps of 0.01 $\frac{\text{mol}}{\text{l}}$, as given in [48], was converted to weight percentages. The needed weight of NaCl was obtained using a scale of 10^{-3} g resolution and 10^{-3} g precision and dissolved in 250 ml of de-ionized water. For all concentrations prepared, an aqueous solution was obtained after the complete dissolution of NaCl. A thermometer of 0.1 °C resolution was used to keep track of the solution's temperature. The LI was measured with either catheter in each solution at least at 7 and maximum at 13 different temperatures between 18.2 °C and 38.8 °C. For better comparison, the simulated results for the respective NaCl solutions were validated against the LI at three different temperatures, namely 21 °C, 25 °C, and 36 °C.

In addition, the catheter-tissue contact effect on LI was measured *in vitro*. A cardiac tissue phantom made of 100 ml de-ionized water, 3 g agar-agar, and 0.0499 g NaCl [152] was prepared. At 25 °C and 14.5 kHz, the expected conductivity of 0.16 $\frac{\text{S}}{\text{m}}$ matched myocardial values well. However, as *in vitro* measurements in this work were taken at 20.5 °C, the actual conductivity might have varied slightly. Typical temperature coefficients reported for similar materials justified the neglect of deviations induced by the described temperature change [148, 153]. Additionally, a small porcine patch of left atrial tissue was

used. Both samples were set at a slightly elevated ring to not disturb measurements by the mount in 0.35% NaCl solution. Either catheter was positioned at either sample in both orthogonal and parallel orientations.

Finally, the effect of catheter irrigation with physiological NaCl solution on LI measurements was studied by incrementing the flow rate of the HAT 500® irrigation pump (Osypka AG, Rheinfelden, Germany) from 0 $\frac{\text{ml}}{\text{min}}$ to 2 $\frac{\text{ml}}{\text{min}}$ and 17 $\frac{\text{ml}}{\text{min}}$ in a 250 ml bath of 0.35% NaCl solution. The flow rate of 2 $\frac{\text{ml}}{\text{min}}$ is clinically applied in standby mode, while it is typically adjusted to 17 $\frac{\text{ml}}{\text{min}}$ during ablation application. The bath model used did not include circulation.

5.2.5 *In Human* Setup

Clinical measurements complement the *in silico* analysis of the effect on the LI when the catheter is withdrawn into the transseptal sheath. Either catheter was located in the left atrium after transseptal puncture using the transseptal sheath, namely the Agilis™ NxT steerable introducer. Verifying the location of the proximal ring electrode outside of the sheath using an X-ray scan, and a central position in bloodpool without endocardial contact, the catheter was gradually pulled back into the sheath at constant speed while the LI was being recorded. In the electroanatomical system, clinical LI was represented by its moving average calculated with a sliding window of 1.5 s width. All measurements were approved by the local ethics committee in accordance with the Declaration of Helsinki and all patients provided written informed consent.

5.3 Results

5.3.1 Aqueous NaCl Solutions

LI *in vitro* measurements in NaCl solutions prepared at 21 °C, 25 °C, and 36 °C following Table 5.1 are presented in Figure 5.3 together with simulated LI values for the corresponding *in silico* molar concentrations. For constant NaCl concentrations, higher temperatures resulted in lower LI values. Both *in vitro* and *in silico* observations followed a hyperbolic trend where LI decreased with increasing conductivity values.

In silico LI results laid between the corresponding *in vitro* experiment values at 21 °C and 25 °C for both catheters with a median deviation of −2.7 Ω and −2.8 Ω from the measurements at 21 °C for the case of IntellaNav MiFi™ OI and IntellaNav Stablepoint™, respectively. This negative deviation aligns with the previous assumption stated in Section 5.2.4 of 20 °C$< T_{\mathrm{Gab}} \ll$ 36 °C. Due to these results, where *in silico* and *in vitro* traces match in morphology and compare well in absolute value, the simulation environment was treated as valid for the relevant range of conductivities used in further settings.

Mass concentrations of 0.35% and 0.41%, meaning NaCl concentrations of $c_{\mathrm{NaCl}} = 0.06\,\frac{\mathrm{mol}}{\mathrm{l}}$ and $c_{\mathrm{NaCl}} = 0.07\,\frac{\mathrm{mol}}{\mathrm{l}}$, yielded similar LI measurements to human blood. At a concentration of $c_{\mathrm{NaCl}} = 0.06\,\frac{\mathrm{mol}}{\mathrm{l}}$, simulated LI resulted in 98.3 Ω and 154.5 Ω compared to *in vitro* measurements at 21 °C of 101.9 Ω and 156.2 Ω for the IntellaNav MiFi™ OI and the IntellaNav Stablepoint™, respectively. These values were in line with the ranges of bloodpool LI observed in the clinical environment.

As given in Table 5.1, the simulated bloodpool LI at conductivity $\sigma = 0.7\,\frac{\mathrm{S}}{\mathrm{m}}$ [50] was at the lower bound of values observed in the clinical environment with 87.1 Ω for the IntellaNav MiFi™ OI and 138.9 Ω for the IntellaNav Stablepoint™.

Using a linear regression, LI measurements between both catheters (LI_{MiFi} and LI_{StPt}) led to a perfect linear relationship ($R^2 < 10^{-4}$) for *in silico* and *in vitro* experiments. An extended set of measurements in 25 NaCl solutions of concentrations between 0.15% and 2.00% yielded the following linear relationship:

$$LI_{\mathrm{StPt}} = 1.42 \cdot LI_{\mathrm{MiFi}} + 8.7\,\Omega \tag{5.1}$$

5.3.2 Transseptal Steerable Sheath

Simulated LI results of the IntellaNav MiFi™ OI and the IntellaNav Stablepoint™ together with an exemplary clinical trace for the withdrawal of each catheter into a transseptal sheath are illustrated in Figure 5.4 (a) and (b), respectively.

Simulated bloodpool LI values of 87 Ω and 139 Ω using the IntellaNav MiFi™ OI and the IntellaNav Stablepoint™, respectively, were the starting

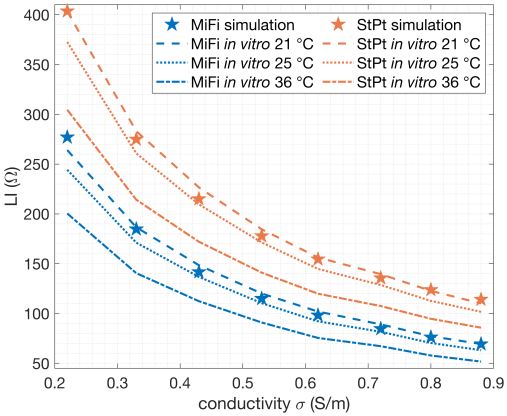

Figure 5.3: *In vitro* LI measurements in NaCl solutions of different molarity compared with corresponding simulated LI values. Dashed lines of increasing distance correspond to measurements at 21 °C, 25 °C, and 36 °C, respectively, whereas star marks refer to simulation results. IntellaNav MiFi™ OI and IntellaNav Stablepoint™ values are shown in blue, and orange, respectively. Image taken with permission from [63].

point for an increase of more than 2 Ω for the distal edge of the sheath located between the proximal and 2nd to proximal ring electrode. With the sheath covering the distal ring electrode, the steep increase of LI values commenced. For the distal edge of the sheath located between the distal ring electrode and the tip electrode, the steepness decreased until forming a small plateau, especially pronounced for the IntellaNav Stablepoint™. The LI increased up to 1353 Ω and 2200 Ω for the sheath fully covering the IntellaNav MiFi™ OI and the IntellaNav Stablepoint™, respectively. At the final stage, the simulated LI decreased as the sheath progressed, covering the tip electrode and revealing the proximal insulator. In contrast, the clinical trace remained closer to the maximum value, forming a plateau until the end of the experiment.

Both *in silico* traces were in line with the clinically measured LI.

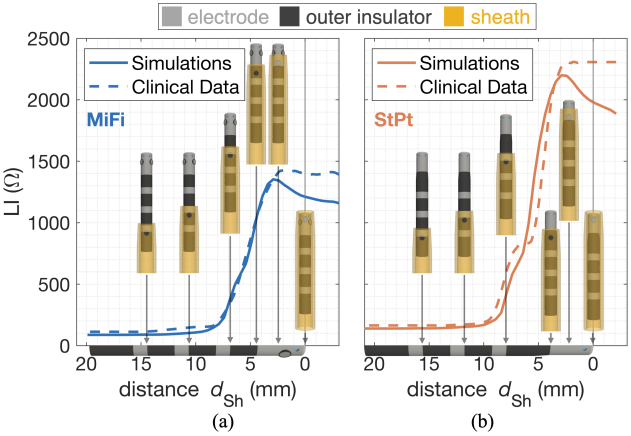

Figure 5.4: Withdrawal of (a) IntellaNav MiFi™ OI and (b) IntellaNav Stablepoint™ into a transseptal sheath. Simulated LI is represented by solid lines while clinical LI is represented by dashed lines. Sheath positions are depicted on the horizontal axes. Image taken with permission from [63].

5.3.3 Catheter-Tissue Interaction

Catheter Distance and Orientation

Again with simulated bloodpool LI values of 87 Ω and 139 Ω for the IntellaNav MiFi™ OI and the IntellaNav Stablepoint™, respectively, a decrease of the distance to the tissue surface with the catheter in perpendicular position ($\alpha_T = 90°$) yielded increasing LI values as shown in Figure 5.5. Respectively for the IntellaNav MiFi™ OI and IntellaNav Stablepoint™, the LI was exceeding the bloodpool value by more than 2% at a distance $d_T = 3.5\,\text{mm}$ and $d_T = 2.5\,\text{mm}$. For $d_T = 0\,\text{mm}$, the LI exceeded the bloodpool LI by 16.0% and 14.9% for either catheter, respectively. The LI trace became steeper the closer the catheter advanced towards the tissue. For negative distances $d_T < 0\,\text{mm}$, i.e. the catheter being introduced into the tissue, the LI increased constantly. For the IntellaNav MiFi™ OI, a small LI plateau was formed between $d_T = -1.0\,\text{mm}$ and $d_T = -1.5\,\text{mm}$.

Simulated LI values are shown in Figure 5.6 for modified angles α_T between either catheter and the tissue for selected distances. All traces, i.e. both catheters and all distances, resulted in a w-shape. From a perpendicular position and tilting towards a parallel position, LI dropped first and increased again later. For a parallel orientation at a distance $d_T = 0\,\text{mm}$, the simulated LI value exceeded the result for a perpendicular position by $14.0\,\Omega$ ($\alpha_T = 0°$) and $12.9\,\Omega$ ($\alpha_T = 180°$) for the IntellaNav MiFi™ OI and by $9.4\,\Omega$ for the IntellaNav Stablepoint™. While the traces were symmetric to $\alpha_T = 90°$ for the IntellaNav Stablepoint™, the LI was dependent on the mini-electrodes orientation for the IntellaNav MiFi™ OI, as represented in Figure 5.6 with the mirrored traces. If one of the measuring mini-electrodes faced the tissue directly ($90° < \alpha_T \leq 180°$), the LI values exceeded those of the same distance and angle without any of the mini-electrodes pointing directly towards the tissue ($0° \leq \alpha_T < 90°$).

In vitro experiments with either catheter in contact with a tissue phantom and a myocardial tissue sample in perpendicular and parallel position resulted in comparable differences between both orientations. The LI for the parallel position exceeded the LI measured perpendicularly by approximately $11\,\Omega$ and $10\,\Omega$ for the IntellaNav MiFi™ OI and IntellaNav Stablepoint™, respectively.

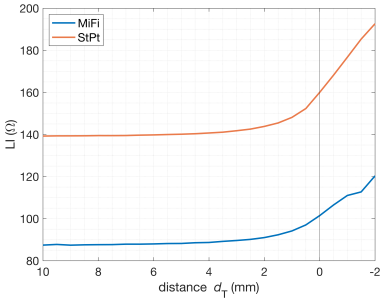

Figure 5.5: Dependency of LI on the distance d_T to myocardial tissue for IntellaNav MiFi™ OI in blue and IntellaNav Stablepoint™ in orange. Image taken with permission from [63].

Transmural Lesion

LI theoretically drops in the surroundings of myocardial scarred tissue caused by the lower conductivity of healthy myocardium in comparison to connective tissue. Figure 5.7 shows LI traces for the virtual catheter passing linear lesions of width $w_{Sc} = 3\,\text{mm}$ and $w_{Sc} = 6\,\text{mm}$. At a catheter-tissue distances $d_T = 0\,\text{mm}$, the absolute LI drop was bigger for the IntellaNav Stablepoint™ due to its higher baseline LI value for either lesion width. However, the percentage drop taking the LI at the furthest point to the lesion and the measurement at direct tissue contact was similar with 3.8% and 6.0%, and 3.9% and 5.7%, for lesion widths of $w_{Sc} = 3\,\text{mm}$ and $w_{Sc} = 6\,\text{mm}$ for the IntellaNav MiFi™ OI and the IntellaNav Stablepoint™, respectively. Raising the catheter 1 mm above the myocardial tissue led to a larger LI drop in the baseline values with comparison to the scar scenario for both catheters.

In Figure 5.8, the potential field (a) and the current density (b) are depicted for the setup with direct catheter-tissue contact including a scar width $w_{Sc} = 3\,\text{mm}$. The current spreads between the injecting electrodes with similarity to an electrical dipole field. The current density reveals the edges of the tissue directly underneath the distal tip electrode, where higher current densities are shown in the central scar line compared to the surrounding tissue of higher conductivity.

5.3.4 Insertion into a Pulmonary Vein

Characteristic LI traces for the progressive introduction of a tip catheter into a PV are depicted in Figure 5.9 (a) for the IntellaNav MiFi™ OI, and Figure 5.9 (b) for the IntellaNav Stablepoint™. For the IntellaNav MiFi™ OI, the simulated LI value increased from 87 Ω in bloodpool up to peak values between 93 Ω and 176 Ω depending on the radius r_{PV} and the thickness th_{PV} of the modeled PV. Similarly, simulated LI values for the IntellaNav Stablepoint™ started from 139 Ω in bloodpool, increasing up to 145 Ω and 240 Ω depending on r_{PV} and th_{PV}.

The radius r_{PV} was found to strongly influence the maximum LI with smaller radii yielding higher LI values. The narrowest simulated PV, with a radius $r_{PV} = 2\,\text{mm}$, yielded a maximum LI of 176 Ω with the IntellaNav MiFi™ OI and 240 Ω with the IntellaNav Stablepoint™, whereas an increase

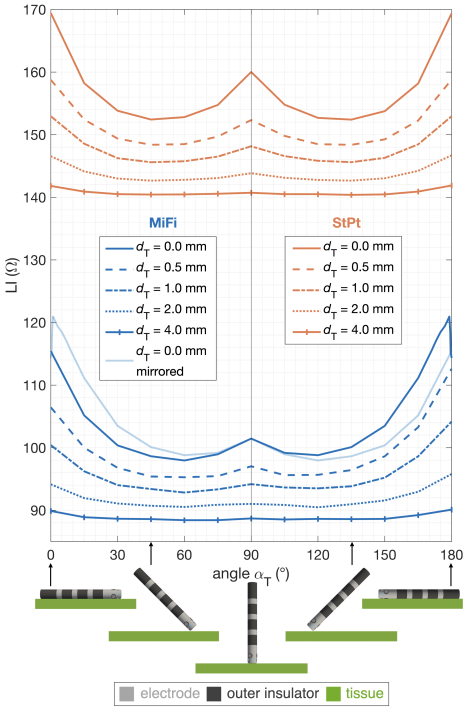

Figure 5.6: Dependency of LI on the angle α_T between catheter and myocardial tissue for the IntellaNav MiFi™ OI in blue and the IntellaNav Stablepoint™ in orange. Different distances d_T between catheter and tissue, as well as the mirrored traces for the IntellaNav MiFi™ OI are depicted with several line styles. Image taken with permission from [63].

of the radius to $r_{PV} = 3$ mm resulted in a maximum LI of 127 Ω and 186 Ω, respectively.

Maximum values for all *in silico* setups corresponded with the insertion of the ablation catheter tip into the PV. The marginal following decrease for further insertions was linked to the passage of the surrounding tissue plate, which contributed to an additional rise of LI values.

The thickness th_{PV} was found to be an additional determinant of the absolute LI value, as shown for a radius $r_{PV} = 6$ mm with several thickness $th_{PV} \in \{1\,\text{mm}, 2\,\text{mm}, 3\,\text{mm}, 4\,\text{mm}\}$. Within the same radius, thicker PVs yielded higher simulated LI values.

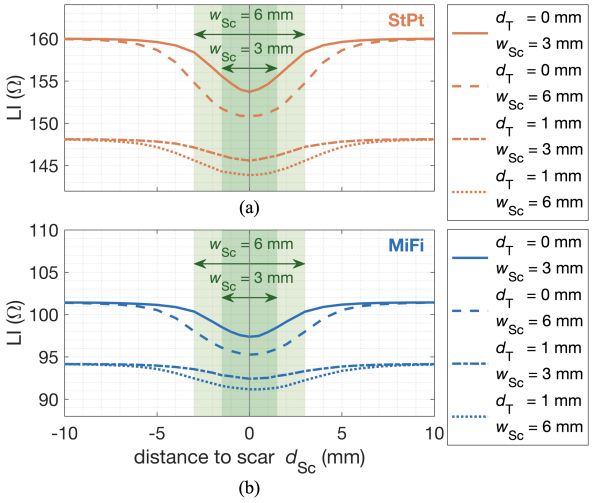

Figure 5.7: Dependency of the LI on the horizontal distance d_{Sc} to a linear scar centered in a patch of tissue for (a) the IntellaNav MiFi™ OI, and (b) the IntellaNav Stablepoint™. Either catheter hung above the tissue at two vertical distances $d_T = 0\,\text{mm}$ and $d_T = 1\,\text{mm}$ for two different scar widths $w_{Sc} = 3\,\text{mm}$ and $w_{Sc} = 6\,\text{mm}$. Image taken with permission from [63].

5.3.5 NaCl Solution Irrigation

Simulated LI values for flushing of either catheter with NaCl solution of physiological concentration from the cooling lumen at the irrigation holes is shown in Figure 5.10. By changing the radius of the bubble r_{NaCl} from 0 to 2 mm, the variation of irrigation flow rate was modeled. The simulated LI values remained almost invariant for NaCl bubbles up to a radius $r_{NaCl} = 0.7\,\text{mm}$ and $r_{NaCl} = 0.55\,\text{mm}$, with less than 1% change compared to the bloodpool measurements of $87\,\Omega$ and $139\,\Omega$ for the IntellaNav MiFi™ OI and the IntellaNav Stablepoint™, respectively. For the IntellaNav MiFi™ OI, the *in silico* LI slightly increased then reaching a maximum value of $1.4\,\Omega$ above the bloodpool for $r_{NaCl} = 0.85\,\text{mm}$ because of the slight overlap of the bubbles with the mini electrodes' distal edges. Right after, the LI values decreased with increasing r_{NaCl} until $76.4\,\Omega$, reached for $r_{NaCl} = 2\,\text{mm}$. According LI traces

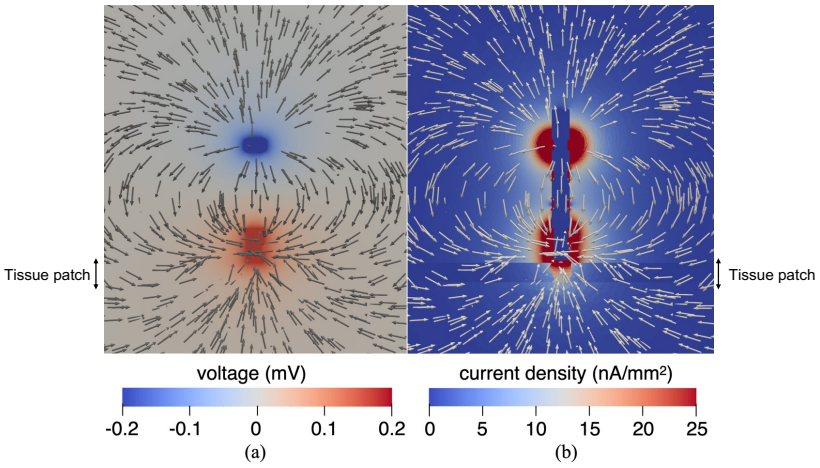

Figure 5.8: Cross section of a transmural lesion setup with a scar of width $w_{Sc} = 3\,\text{mm}$ centered in a patch of myocardial tissue and surrounded by blood. The (a) potential field and (b) current density characterize the electrical field. Arrows represent the current flow direction. Image modified with permission from [63].

decreased monotonously for the IntellaNav Stablepoint™ down to $116.6\,\Omega$ at NaCl bubbles of $r_{\text{NaCl}} = 2\,\text{mm}$.

Mini panels in Figure 5.10 (a-b) illustrate the *in vitro* LI experiments for onset and offset of irrigation at two different flow rates, i.e. $2\,\frac{\text{ml}}{\text{min}}$ and $17\,\frac{\text{ml}}{\text{min}}$. *In vitro* traces at a flow rate of $2\,\frac{\text{ml}}{\text{min}}$ showed an instantaneous drop of $0.6\,\Omega$ and $1\,\Omega$, as well as oscillations of $0.6\,\Omega$ and $1\,\Omega$ peak-to-peak amplitude for the IntellaNav MiFi™ OI and the IntellaNav Stablepoint™, respectively. For the IntellaNav Stablepoint™, LI dropped abruptly by $2.5\,\Omega$ at the onset of irrigation at $17\,\frac{\text{ml}}{\text{min}}$. LI progressively decreased as a result of a modest bath volume merging with the irrigation solution of higher conductivity.

5.4 Discussion

In summary, we introduced a computational environment that closely simulated *in human* and *in vitro* LI measurements. This *in silico* setup enabled the

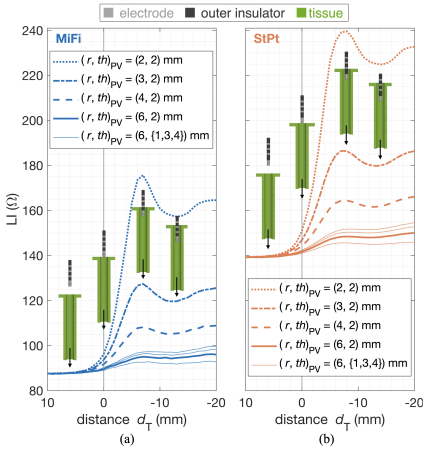

Figure 5.9: LI traces during the gradual insertion of ablation catheter into a PV: (a) IntellaNav MiFi™ OI in blue and (b) IntellaNav Stablepoint™ in orange. The horizontal axis indicates the distance d_T between the tip of the catheter and the edge of the tissue. Negative distances correspond to positions inside the PV. Image taken with permission from [63].

quantification of several factors affecting the measurements with an established ground truth.

5.4.1 Aqueous NaCl Solutions

Validation of the model using standard aqueous NaCl solutions with known conductivity confirmed the simulation environment to be appropriate. NaCl solutions can be assumed to behave as resistors at the employed measurement frequency of 14.5 kHz. Therefore, the hyperbolic relationship between conductivity and LI can be attributed in this setup to the reduction of impedance, which is reciprocally related to conductivity.

In the *in vitro* experiments, it was demonstrated that NaCl solutions at mass concentrations ranging from 0.35% to 0.4% at 21 °C are suitable as equivalent of human blood at body temperature for a measurement frequency of 14.5 kHz.

The fact that LI measurements with the IntellaNav MiFi™ OI and the IntellaNav Stablepoint™ resulted in a perfectly linear relationship is of significant clinical value. Clinical trials carried out with one catheter can be translated and

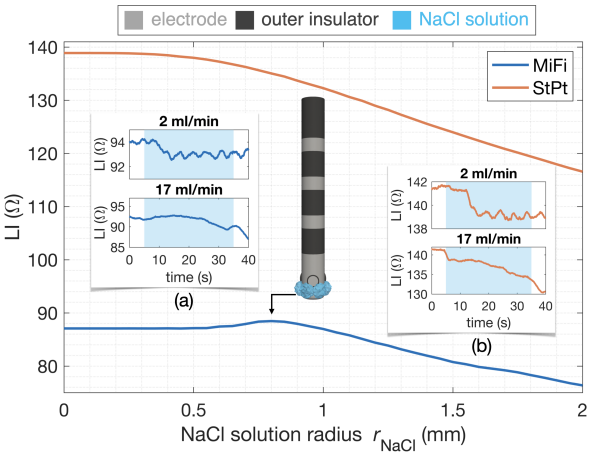

Figure 5.10: *In silico* LI for different irrigation radii of NaCl solution for the IntellaNav MiFi™ OI in blue and the IntellaNav Stablepoint™ in orange. Subpanels (a) and (b) report *in vitro* measurements for the onset of irrigation flow rates of 2 $\frac{ml}{min}$ and 17 $\frac{ml}{min}$. Irrigation times are shaded in blue. Image taken with permission from [63].

extrapolated to the respective other device, ending up in a reduction of efforts and financial costs. Taking measurements with several catheter items yielded to slight deviations of the linear coefficients. This may be caused by minor – but still acceptable within a tolerance – differences in manufacturing or due to its previous use for radio frequency ablation prior to the *in vitro* experiments.

5.4.2 Transseptal Steerable Sheath

Simulated results showed that LI began to rise remarkably once the steerable sheath exceeded the proximal ring electrode. LI measurements used in clinical practice to characterize both the substrate and the ablation lesion should therefore always ensure full catheter withdrawal out of the sheath, as of helping in the prevention of confounding influences on the measured LI.

5.4.3 Catheter-Tissue Interaction

For 0 mm distance to the tissue, i.e. 0 g so-called "contact force", to −2 mm distance to the tissue, the increase of LI above the bloodpool value ranged from 14 Ω to 33 Ω, respectively, comparing well with the mean ranges between 16 Ω and 20 Ω [128] observed in the clinical practice for the IntellaNav MiFi™ OI. The simulated upper bound of an immersion depth of 2 mm most likely overestimates the LI for mean contact force in the clinical application due to neglecting a realistic tissue deformation effect.

Detailed *in vitro* experiments on catheter-tissue interaction using the IntellaNav MiFi™ OI catheter had been performed in previously published work by Sulkin et al. [40], where the authors found a non-linear and monotonic increase of LI with the approximation of the catheter towards a perpendicular position. The *in silico* results presented in this work mimicked the morphology of the curve well but led to scaled absolute values and slopes presumably caused by discrepancies in the underlying tissue and blood conductivities. In the case of Sulkin et al., the right ventricular tissue employed was probably thicker than the 2.5 mm thickness of the modeled atrial tissue used in this work, which may explain both the higher absolute values and slopes in the previous study. Furthermore, the existing variability of conductivity in real tissue samples can cause a spread of measured LI values in Sulkin's work that are not present in our work due to the choice of one specific conductivity phantom within the human myocardial range.

Varying the catheter-tissue angle yielded higher LI values in parallel than in perpendicular catheter orientations for distances $d_T > -2$ mm both in the work by Sulkin et al. and the *in silico* experiments presented here. Garrott et al. [87] measured a mean LI difference of 13 Ω between parallel and perpendicular catheter orientation using the IntellaNav StPt™, which aligns well with the simulated results computed in this work.

In silico experiments computed with the IntellaNav MiFi™ OI showed a slight plateau for the immersion into a myocardial tissue patch by 1.0 mm to 1.5 mm, as well as a sudden decrease in LI measurements for an angle $\alpha_T = 180\,°C$ that did not match well with the respective trend of adjacent distances and angles. It can be assumed that the close interaction between the mini-electrodes and the tissue induced both findings.

Clinical studies for the use of IntellaNav MiFi™ OI reported different ranges of LI measured on healthy and scar tissue, e.g. $109\,\Omega \pm 15\,\Omega$ and $104\,\Omega \pm 12\,\Omega$ [154], $111\,\Omega \pm 14\,\Omega$ and $92\,\Omega \pm 16\,\Omega$ [155], and $132\,\Omega \pm 12\,\Omega$ and $85\,\Omega \pm 11\,\Omega$[90], respectively. Different operators and force applied at the contact may explain the variability in range. Scar tissue presented lower LI simulated values in comparison with healthy myocardium following previous clinical findings. In both *in silico* and clinical observations it can be explained as an increasing in conductivity due to the increase in extracellular space for the scar tissue. However, simulated values displayed in Figure 5.7 were slightly lower in comparison with the clinical studies [90, 154, 155], most likely caused by the selected conductivities or due to an insufficient catheter-tissue contact modeled in this *in silico* study. Our model represents the equivalent of 0 g so-called "contact force", whereas in the experimental and clinical environment the typical value oscillates from 5 to 20 g. The larger the lesion area within the footprint of the catheter, the lower the LI dropped. For quantitative applications of LI measurements, the results shown in Figure 5.7 pointed out the importance of adequate catheter-tissue contact and regulated contact force. Only by 1 mm distance to the endocardial surface the LI drop from baseline values was larger than the difference between LI measured at healthy myocardium and scar tissue. As LI values depend highly on the selected conductivity for the *in silico* model, an accurate and precise validation of the atrial scar tissue conductivity would reinforce the results presented in this work.

In this preliminary study, myocardial tissue was only modeled as a homogeneous and transmural block. The potential effect that fiber anisotropy and three-dimensional atrial tissue structures may have on *in silico* LI results was out of the scope of this work. Future studies will have to consider the mechanical response of the myocardium to catheter-tissue contact using more realistic myocardial models.

5.4.4 Insertion into a Pulmonary Vein

The results presented in Figure 5.9 highlighted the strong effect that the PV radius has on the LI measured inside of the vein. Although the PVs and the atrial myocardium differ histologically, no differences were considered between

them in terms of modeling in this *in silico* study, which may affect the difference with LI measured *in human* PVs.

5.4.5 NaCl Solution Irrigation

Both catheters employed in this simulation study, namely the IntellaNav MiFi™ OI and the IntellaNav Stablepoint™, include an open irrigated tip for cooling purposes using 0.9% NaCl solution during radio frequency delivery. However, as seen in Table 5.1, human blood is having a different conductivity than the so-called physiological NaCl solution at lab temperature by a factor of approximately 2. According to previous studies, this solution irrigation does have an effect on lesion formation during ablation delivery. As current flow is attracted to the highly conductive saline solution, the current flowing through the ablation target tissue is reduced and smaller lesions in comparison with the ones created with a less concentrated irrigation fluid, i.e. 0.45% NaCl solution or dextrose water, are obtained [156–159]. While measuring LI, special attention needs to be drawn to irrigation fluid flow in two specific situations: when there is a constant flow of liquid, and when the flow rate changes. Constant irrigation flow may be related to the use of LI as substrate mapping feature, while situations with a change of flow rate can be related to radio frequency ablation delivery. In either case, clinical LI is mainly interpreted as a comparison between the bloodpool reference or the LI value at the beginning of the ablation delivery, rather than looking at absolute values.

During radio frequency ablation delivery, the typical irrigation flow rate increases from the default value of 2 $\frac{\text{ml}}{\text{min}}$ to 17 $\frac{\text{ml}}{\text{min}}$ or even 30 $\frac{\text{ml}}{\text{min}}$, which increases the volume of NaCl solution enclosing the tip and may have an effect in the LI drop that is not related with tissue heating. However, in Figure 5.10 the LI drop caused by changes in the irrigation flow rate seems to be unimportant considering typically desired minimum LI drops between 12 Ω and 16 Ω during radio frequency power delivery using the IntellaNav MiFi™ OI [89], which confirms the assumption that the NaCl solution irrigation is merged fast with the circulatory blood.

On the other hand, when it comes to LI used in substrate mapping, slight differences become of importance. Keeping the flow rate consistently low at 2 $\frac{\text{ml}}{\text{min}}$ restricts the chances of affecting the measurement. Looking at the LI only

in differential manner can make the results be influenced when the distribution of NaCl near the catheter tip changes, for example due to blood flow. Moreover, due to the high electrical conductivity of NaCl in comparison to tissue and blood, less current flows through the measurement area.

The lack of a precise correlation between spherical NaCl radius in this work and irrigation flow rates used in the clinical setups limit the results together with the oversimplified spheres of irrigation fluid at the catheter tip. The *in vitro* setup used for comparison with the simulations did not include a circulatory blood flow, whose inclusion may have added more detailed information about the influence of irrigation changes on the LI measurements.

5.4.6 Sensitivity

The geometrical model of the catheter was of high importance for the obtained LI value. Small deviations in the dimensions, especially in the electrodes, caused notable changes in the results. For quantitative analysis, a detailed and accurate model of the investigated catheter is crucial. This was guaranteed in this study.

In silico experiments in this study proved that a subset of clinically relevant settings, such as the presence of scar tissue, resulted in small variations of the measured LI. However, the loss of appropriate catheter-tissue contact has a bigger impact on LI, sometimes even more significant. LI measurements in a non-controlled clinical environment with artifacts and background noise in the measurements may make the changes in LI hard to notice. This highlights the need of assuring a suitable contact with the heart wall and controlling other recording conditions when using LI technology in practice.

In addition to the clinical measurement noise, the presence of air in the lungs, as well as their inflation and deflation process, is of evident impact on the LI measurement [128] due to the close proximity of the lungs to certain chambers of the heart. The conductivity of inflated lungs is reported to be $0.0954\,\frac{\mathrm{S}}{\mathrm{m}}$ at 14.5 kHz, increasing up to $0.247\,\frac{\mathrm{S}}{\mathrm{m}}$ in deflated state [49]. As the respiratory state of the patient is known, this respiratory oscillations could be compensated in LI measurement traces.

To account for the suitability of catheters and electrode arrangements for impedance measurements, different catheter settings and how their electrode

distribution affects the measured LI need to be estimated. The close distance of the catheter will take more influence on the measured LI value in comparison to the generator impedance measurements. Clinically relevant examples such as varying the catheter-tissue distance, the catheter-tissue angle, or introducing an insulating sheath were tested in this study. However, not only the variation in the position of the setting around the catheter, but also size and conductivity variations on the setting itself should be included. Future studies should account for catheter and electrode arrangement affecting LI measurements to further optimize their settings.

5.5 Conclusion

In this preliminary work, an *in silico* model with highly detailed catheter and sheath geometries included in a simple myocardial tissue patch was used to study local electrical impedance measurements using point ablation catheters. Clinically relevant scenarios, such as catheter-tissue interaction varying distance, angle, and tissue substrate, the insertion of a catheter into a PV, its withdrawal into the transseptal steerable sheath, and saline solution irrigation were reproduced *in silico*. Forward simulations of the electrical field provided a better understanding of the quantitative effects of single and combined modifications in several parameters on the LI measurements. The resulting environment proved to be a valuable tool that offers deeper insight into the clinical interpretation of LI and has the potential to support future catheter development.

Chapter 6

In Silico Evaluation of the Effect of Contact Force on Local Impedance

This chapter aims to give some insights about how local electrical impedance measurements are affected by catheter-tissue pressure contact and deformation of the underlying myocardium.

The content of Chapter 6 is taken from conference proceedings published in Europace 2022 [160] and Computing in Cardiology 2022 [161]. Most passages in this chapter have been quoted verbatim from the publications and are adapted with permission from the authors and Oxford Academic Press. Work presented in Section 6.2.1 and subsequent results were carried out during the master thesis of M.Sc. Andreas Heinkele [162].

6.1 Introduction

Atrial fibrillation (AF) is the most common cardiac arrhythmia and it is characterized by a remodeling of the cardiac substrate. A standard treatment for patients with AF is ablation. Applying controlled force to the tissue with the catheter can assure good electrode-tissue contact, which is important to perform effective lesions during ablation procedures.

In persistent AF patients, ablation lesions can be placed in areas of scar tissue in addition to usual pulmonary vein isolation (PVI). Currently, the characterization of the substrate is supported by voltage mapping to locate these scar tissue areas. Recently, local impedance (LI) has been gaining attention due to its independence on the electrical activity to better differentiate healthy tissue from scar [90]. Therefore, it may improve the current understanding of underlying substrate. In this chapter, the term "scar tissue" is employed for both scar and fibrotic tissue.

The new generation of ablation catheters, as the IntellaNav Stablepoint™ (Boston Scientific, Marlborough, MA, USA), can help achieving good electrode-tissue contact by measuring the contact force (CF) at the tip, and also recording LI. The combination of both techniques results in a novel method to characterize the process of lesion formation.

Some studies have recently investigated the effect of CF in ablation assessment [163]. However, the effect of CF on the LI measurements to characterize the substrate needs to be further explored. *In silico* experiments are helpful to better understand tissue behavior in a controlled environment without noise sources and measurements uncertainties. To show its clinical utility, validation of the model is performed by comparing the simulated data with LI clinical data acquired at manually controlled CF values,

In this work, we study the effect of mechanical deformation of the atrial tissue on LI measurements for several thicknesses and CFs using the *in silico* framework from Chapter 5. Our objective is to study the possibility to characterize healthy tissue and scar tissue by means of LI taking into account the effect of tissue thickness and CF.

Including an extension of the previously described model by introducing mechanical deformation, as well as the validation with clinical data taken at different CFs, this work continues studying the comprehension of LI measurements and the potential development of mapping catheters including this feature.

6.2 Methods

In Figure 6.1, the *in silico* framework used to conduct the simulations in this work is depicted. The IntellaNav Stablepoint™ was model in a similar way as in Pollnow et al. [164] – just as described in Chapter 5 – and was placed

within a 140 mm × 140 mm × 140 mm box representing the surrounding blood. Centered below the tip of the catheter and in direct contact with it, a squared patch of tissue measuring 110 mm × 110 mm × t_{th} was positioned, where t_{th} defines the tissue thickness within the anatomical range of 2.5 to 7.5 mm [146] in steps of 1 mm.

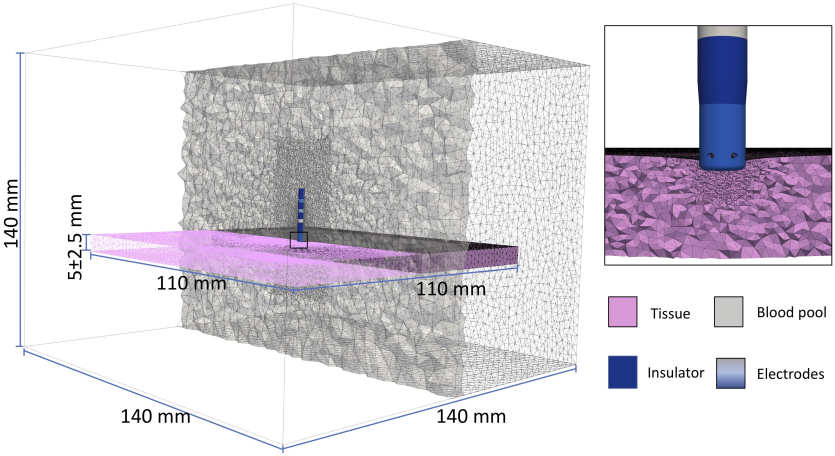

Figure 6.1: *In silico* experiment setup that contains the IntellaNav Stablepoint™ catheter with its different conductive (light blue) and isolator (dark blue) parts, tissue patch (pink) with different thicknesses, and bloodpool (grey).

Geometry representation and tetrahedral meshing was performed in Gmsh (version 4.5.6) [145]. A total of 1,577,670 million tetrahedral elements comprised the mesh. Mesh resolution of blood and tissue elements was adapted to be the highest surrounding the tip and close to the tissue surface, while it decreased for larger distances to the catheter. The minimum, average, and maximum length of the elements were 0.0008 mm, 1.9668 mm, and 11.1377 mm, respectively.

6.2.1 Atrial tissue deformation model

To identify the impact of CF on LI measurements, mechanical deformation was simulated by finite element analysis with Ansys (Ansys® Academic Research Mechanical, Release 18.1). An elastic model with Young's modulus reported by Bellini et al. [165] for human cardiac tissue was adopted for the tissue's mechanical behavior. In the case of scar tissue, the healthy Young's modulus was increased five-fold as described in the work of Villemain et al. [166]. Consequently, the Young's modulus for healthy and scar atrial tissue was set to 19.19 kPa and 88.73 kPa, respectively.

A perpendicular CF between 1 and 6 g in steps of 1 g for both healthy and scar tissue was applied in the model. Furthermore, the range between 10 and 25 g in steps of 5 g was also simulated for the scar tissue case. In Figure 6.2, a healthy deformed mesh after applying a CF of 5 g with the corresponding displacement of each cell element is depicted.

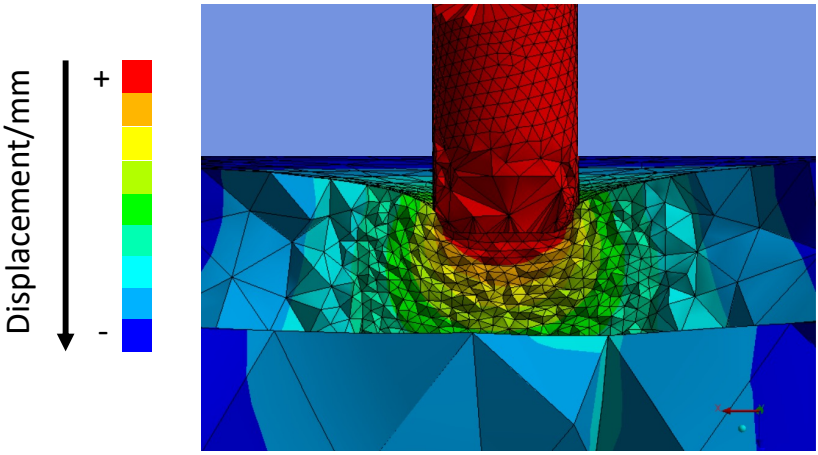

Figure 6.2: Exemplary image of an atrial mesh deformed after applying 5 g of CF. The absolute displacement value of each cell element is color-coded ranging from 1.16 mm in the red zone, to 0 mm in the dark blue.

6.2.2 Local electrical impedance simulation

After the mechanical simulations, the electrical properties were assigned to each tetrahedral element of the setup mesh. Conductivity values at 14.5 kilohertz (kHz), as detailed in Table 6.1, were chosen for the metallic electrodes, insulator, blood, healthy tissue, and scar tissue as 400,000 S/m, 10^{-7} S/m, 0.7 S/m, 0.164 S/m, and 0.387 S/m, [50] respectively. To simulate the electrical field created by the Rhythmia HDx electroanatomical mapping system (Boston Scientific, Marlborough, MA, USA) used in the clinics, an alternating current of 5 µA peak-to-peak amplitude at 14.5 kHz was modeled using the software EIDORS [150] in MATLAB (The MathWorks, Inc., Natick, MA, USA, version 2021a). Stimulation and measurement circuits were defined according to the catheter system and the resulting voltage amplitude was divided by the amplitude of the injected current to obtain the LI.

Table 6.1: Conductivities of relevant materials employed in the simulations at 14.5 kHz for body temperature in this work.

Material	Conductivity σ (S/m)	Reference
Platinum electrode	400,000	[149]
PEBA insulator	10^{-7}	
Blood	0.700	[49, 50]
Myocardium	0.164	[49, 50]
Connective tissue (scar)	0.387	[49, 50]

6.2.3 Clinical cohort

Patients diagnosed with either AF or atrial flutter (AFlut) undergoing left atrium (LA) ablation therapy with the IntellaNav Stablepoint™ catheter and the Rhythmia HDx electroanatomical mapping system (Boston Scientific, Marlborough, MA, USA) at the Städtisches Klinikum Karlsruhe (Karlsruhe, Germany) were included in this analysis. The clinical cohort comprised 10 patients (2 female) with a mean age of 63.9±10.2 years, including both de novo ablations and

redo procedures. The study was approved by the local ethics committee and all patients provided written informed consent.

CF and LI data were acquired after bipolar voltage electroanatomical mapping in healthy tissue areas on the anterior wall. In 8 of the patients, at least one point in low voltage regions of the LA was recorded as scar tissue. After evaluating the viability of the recording points, the available dataset, described in Table 6.2, was compound of 20 anterior points and 9 scar points. Each LI measurement was correlated with its corresponding CF value, which was increased from 0 g to the saturation point ($\sim$70 g).

Table 6.2: Detailed description of the clinical dataset used in this work. Disaggregated number of points recorded per patient, recorded per anatomical region, total number of points per patient and per anatomical region, and total amount of viable points are specified.

	Patient n°										Total points (#)
	1	**2**	**3**	**4**	**5**	**6**	**7**	**8**	**9**	**10**	
Anterior points (#)	2	2	2	3	2	2	1	2	2	2	20
Scar points (#)	-	-	1	1	-	1	2	2	1	1	9
Total points (#)	2	2	3	4	2	3	3	4	3	3	29

Due to the susceptibility to oscillations of raw LI recordings, a moving average approach was chosen instead. All LI measurements from each patient recorded at every applied CF were collected. Due to slightly different sampling frequencies between the two parameters that causes a non-simultaneous recording, namely 20.0115 Hz and 19.8908 Hz for LI and CF respectively, the closest corresponding timestamp to the annotated start and end times were found in either signal recording. Afterwards, outliers determined as values not included in $median \pm 1.5 \times IQR$ were removed. At each selected CF, all LI measurements from each patient were represented as median and interquartile range after removing the outliers, resulting in one *in human* value for each CF.

6.3 Results

In silico LI results, as depicted in Figure 6.3, from simulations with mechanical deformation showed lower values in scar than in healthy tissue at identical

applied CF. Moreover, LI values were higher for larger CFs and thicker tissues indistinctly from the tissue type.

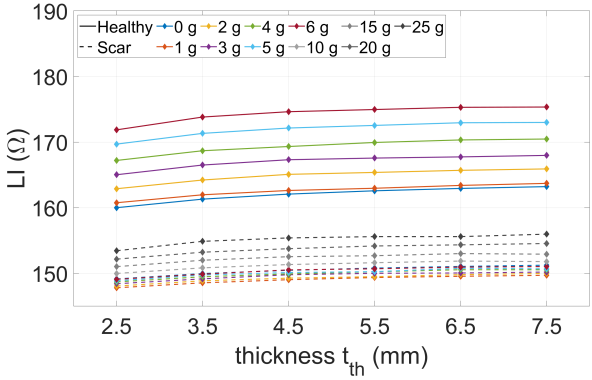

Figure 6.3: *In silico* LI values at CFs between 0 and 6 g in healthy myocardium (solid lines) and scar tissue (dashed lines) for t_{th} between 2.5 and 7.5 mm. In scar tissue LI values for *in silico* experiments at 10, 15, 20, and 25 g are also shown.

In healthy myocardium, *in silico* LI values ranged from 160 Ω to 175 Ω for CF between 0 and 6 g, whereas values between 148 Ω and 151 Ω were obtained for scar tissue. When applying higher CFs to the scar, i.e. between 10 and 25 g, LI values increased up to 156 Ω. There was no overlap between values obtained for healthy tissue and scar tissue for any of the given tissue thicknesses and applied CFs.

Figure 6.4 shows trends for both healthy and scar tissue when increasing CF. Simulated values laid in the range of clinical data for scar and healthy tissue. Healthy and scar clinical data did not follow the trend of *in silico* values from 0 to 6 g as well as scar tissue did from 6 to 25 g, as depicted in Figure 6.5.

Differences between simulated and clinical data acquired in healthy tissue were not statistically significant (Wilcoxon rank sum test for unpaired samples), whereas they were for the case of scar tissue. In parallel, clinical data acquired in scar and healthy tissue did not yield statistically significant differences while simulated measurements demonstrated statistical significance.

Table 6.3: LI_{SIM} results in Ω for healthy myocardium with t_{th} between 2.5 and 7.5 mm at applied CF between 0 and 6 g.

CF (g)	Tissue thickness t_{th} (mm)					
	2.5	3.5	4.5	5.5	6.5	7.5
0	160.005	161.308	162.075	162.578	162.940	163.214
1	160.759	161.970	162.627	162.965	163.398	163.709
2	162.893	164.220	165.085	165.375	165.697	165.912
3	165.026	166.502	167.312	167.564	167.745	167.972
4	167.202	168.681	169.325	169.941	170.327	170.466
5	169.691	171.816	172.143	172.540	172.946	172.995
6	171.864	173.816	174.629	174.960	175.297	175.341

Table 6.4: LI_{SIM} results in Ω for scar with t_{th} between 2.5 and 7.5 mm at applied CF between 0 and 6 g in steps of 1 mm, and 10 to 25 g in steps of 5 mm.

CF (g)	Tissue thickness t_{th} (mm)					
	2.5	3.5	4.5	5.5	6.5	7.5
0	149.148	149.965	150.463	150.801	151.051	151.244
1	147.799	148.556	149.032	149.364	149.555	149.707
2	148.065	148.864	149.270	149.492	149.798	149.990
3	148.417	149.160	149.788	150.008	150.053	150.197
4	148.693	149.482	149.918	150.242	150.553	150.545
5	148.870	149.759	150.124	150.259	150.775	150.689
6	149.089	149.883	150.527	150.698	150.954	151.053
10	149.982	150.836	151.341	151.620	151.871	151.788
15	151.021	151.998	152.540	152.687	153.011	152.920
20	152.166	153.223	153.757	154.171	154.344	154.549
25	153.443	154.879	155.399	155.597	155.597	155.972

6.4 Discussion

In silico experiments were performed to evaluate the effect of CF on LI measurements in deformed atrial tissue. For CF values between 1 and 6 g, first mechanical deformation and subsequently electrical impedance measurement were simulated. For the case of 0 g, no mechanical interaction was performed. These CF were applied in both healthy and scar myocardial tissue with thicknesses between 2.5 and 7.5 mm.

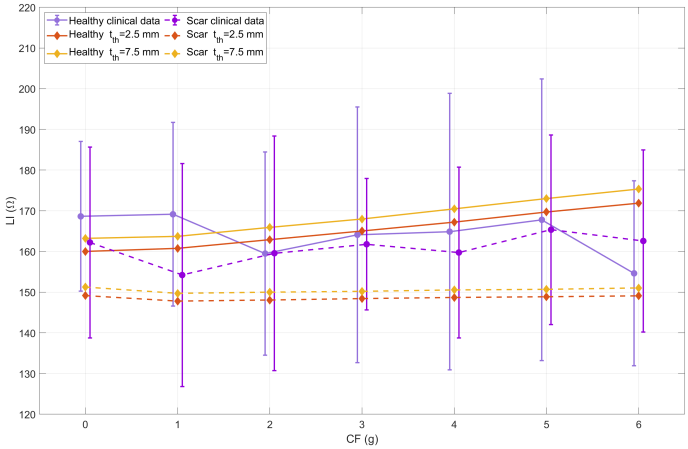

Figure 6.4: LI values for *in silico* (diamond) at CFs between 0 and 6 g in tissues of 2.5 mm (red) and 7.5 mm (yellow) and clinical data (circles). Healthy tissue is represented by solid lines while scar tissue is represented by dashed lines.

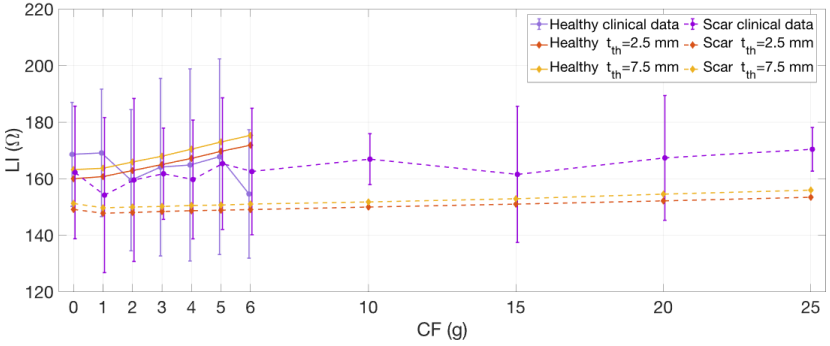

Figure 6.5: LI values for *in silico* (diamond) and *in human* (circles). LI_{SIM} results at CFs between 0 and 6 g in tissues of 2.5 (red) and 7.5 mm (yellow) are plotted for healthy (solid lines) and scar tissue (dashed lines). Median clinical value (circles) among 10 patients and its interquartile range are shown for healthy (light purple) and scar (dark purple) at each CF value. For scar tissue, CF values between 10 and 25 g are also plotted.

In silico results showed in Figure 6.3 that healthy and scar tissue can be distinguished even when increasing the contact force and tissue thickness. Moreover, *in silico* results laid in the range of clinical data, as depicted in Figure 6.4, for healthy and scar tissue. However, healthy clinical data shows a drop at 3 g and 5 g, which was not observed *in silico* but could be explained due to the extreme difficulty getting exact CF values below 10 g measured by human. However, trends of clinical data followed the expected behavior as scar tissue usually presents lower LI values than healthy tissue [128]. *In silico* healthy values showed more similar results when comparing with healthy clinical data than scar tissue.

Even when increasing the contact force to up to 25 g and varying tissue thickness, *in silico* results showed that healthy and scar tissue can be clearly distinguished. However, LI from *in silico* experiments tended to overlap between healthy and scar clinical data acquired on 10 patients, even though the simulations remain within an acceptable range of values. Statistical studies showed that clinical and *in silico* data cannot be considered different for the case of healthy tissue. However, that is not the case for scar scenarios. Besides, clinical data do not differ statistically between healthy and scar, which could have been caused by difficulties during the acquisition or simply due to the low number of patients recruited.

In this study, the whole tissue patch was simply changed to scar properties when simulating scar. In a more realistic way, diffuse patches of fibrosis and healthy tissue should be interspersed to better model the mechanical and electrical interaction. Moreover, left atrial tissue was model as an elastic tissue with ventricular parameters due to the lack of more specific literature. The introduction of an hyperelastic model in future studies will allow to model broader ranges of CF as used in the clinics.

Nonetheless, our *in silico* setup helped to better understand the link between CF and LI in both healthy and scar tissues, showing similar results as those obtained in both *in vitro* and *in human* environment [87, 163, 167]. LI values are expected to distinguish between healthy and scar tissue independent from the atrial rhythm, which can improve the understanding of underlying substrate, even more, when corrected for an eventual lack of contact by combining it with CF. Understanding how this CF affects the LI will allow to move slowly towards an intracavitary impedance electroanatomical mapping system.

6.5 Conclusions

We evaluated the effect of the CF and tissue thickness on LI measurements for healthy and scar tissue. Simulated LI values increased with CF, as well as with t_{th}. Simulations performed in tissues applying identical CF yielded to lower LI values in scar than in healthy myocardium. Healthy and scar tissue can still be distinguished by means of LI. Comparing to clinical data, our simulations laid within the range of clinical measurements for both healthy and scar tissue. To conclude, mechanical deformation does have an effect on LI simulations in atrial tissue, especially in healthy tissue, and still can help characterizing fibrotic substrate by means of LI. A larger dataset of clinical data with higher variability should be acquired for more detailed analyses in future work.

Chapter 7

In Silico Study of Local Impedance in Multielectrode Catheters

In previous chapters, an *in silico* framework with ablation catheters to evaluate local impedance (LI) confounding factors has been developed and explored. By extending this setup with multielectrode mapping catheters, this chapter aims to give some more insights about how local electrical impedance measurements can be used to characterize atrial substrate.

7.1 Introduction

In Chapter 5 and Chapter 6, an *in silico* framework with ablation catheters to evaluate LI measurements in the cardiac tissue has been presented. However, these *in silico* measurements were limited to those catheters including the DirectSense™ technology, which nowadays only consists of ablation catheters.

The DirectSense™ technology [40] (Boston Scientific, Marlborough, MA, USA), integrated into the Rhythmia HDx electroanatomical mapping system (Boston Scientific), provides impedance measurements on an ablation catheter without the need of a reference skin electrode. This technology determines only point-by-point values obtained at the tip of the catheter, but can serve as

a starting point to extend the concept towards a mapping system. The main advantage lies in having two distinct pairs of electrodes as part of the injection and measurement circuit, which minimizes the impact of contact impedance between the electrode and the tissue.

Beyond monitoring ablation lesion formation, LI has demonstrated potential in characterizing cardiac tissue and distinguishing between healthy myocardium and fibrotic or scar tissue [2, 3, 90]. Unger et al. [128] also demonstrated the potential use of LI by acquiring full atrial impedance maps. Thus, the implementation of LI measurements onto multielectrode catheters may show potential benefit in better tissue characterization when combined with widely extended methods such as voltage maps obtained from electrogram (EGM) recordings.

This work introduces a preliminary study of *in silico* LI measurements using the layout of a multielectrode mapping catheter. Located in a simple myocardial tissue patch, different electrodes from the catheter will serve as part of the injection and measurement bipolar pairs to account for substrate characterization sequentially.

7.2 Methods

7.2.1 Geometrical setup

An *in silico* environment was developed for simulating the forward propagation of the electrical field. As illustrated in Figure 7.1 (a), a tissue patch measuring 70 mm $\times$ 70 mm $\times$ 2.5 mm was embedded into a box of blood of measures 100 mm $\times$ 100 mm $\times$ 100 mm.

A multielectrode grid setup was implemented in 4×4 configuration mimicking the Advisor™ HD Grid (Abbott, Chicago, IL, USA). The spacing between the electrodes was defined as $d_E = 4$ mm as shown in Figure 7.1 (b). Denoted as d_T and schematically presented in Figure 7.1 (c), the catheter-tissue distance ranged from 0 to 2 mm in steps of 0.5 mm. The electrodes were configured as spheres parameterized by the radius $r_S = 0.5$ mm.

For the geometrical setup previously described, three different tissue configurations depicted in Figure 7.2 were employed, encompassing homogeneous

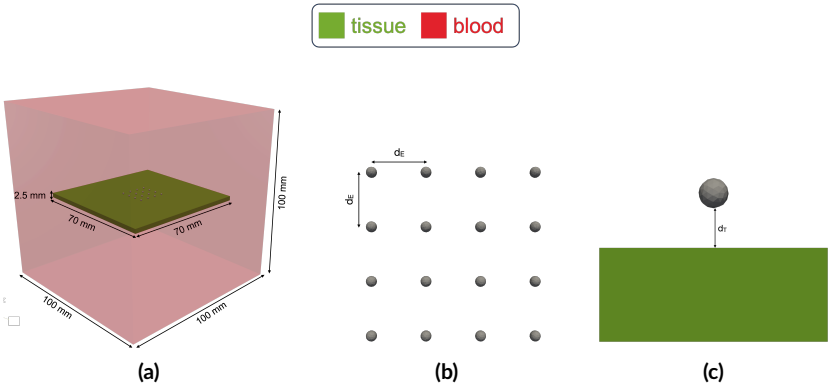

Figure 7.1: Geometrical setup to simulate forward electrical propagation. (a) A tissue patch is embedded inside a blood box, and a 4×4 grid catheter with spherical electrodes is placed on the center at direct catheter-tissue contact. (b) Top view of the circular catheter geometry with inter-electrode distance parameter, and (c) front view of an electrode elevation showing its position above the tissue surface in cross-section.

physiological tissue, homogeneous scar tissue, and a central transmural scar line with a width of 8 mm flanked by healthy myocardium.

7.2.2 Material Properties

The tetrahedral elements of the mesh were assigned characteristic conductivity values for the respective material at 14.5 kilohertz (kHz) as described in Table 7.1 for body temperature. The employed frequency was chosen to match the frequency implemented in the DirectSense™ [40] by the Rhythmia HDx electroanatomical mapping system (Boston Scientific, Marlborough, MA, USA) used in the clinics.

7.2.3 Stimulation Patterns

For the squared catheter, a total of eight different bipolar pairs were simulated, as depicted in Figure 7.3. A four electrode circuit was always used, meaning that two electrodes were part of the injecting pattern and a potential difference was measured between another two. The horizontal patterns where the electrodes are

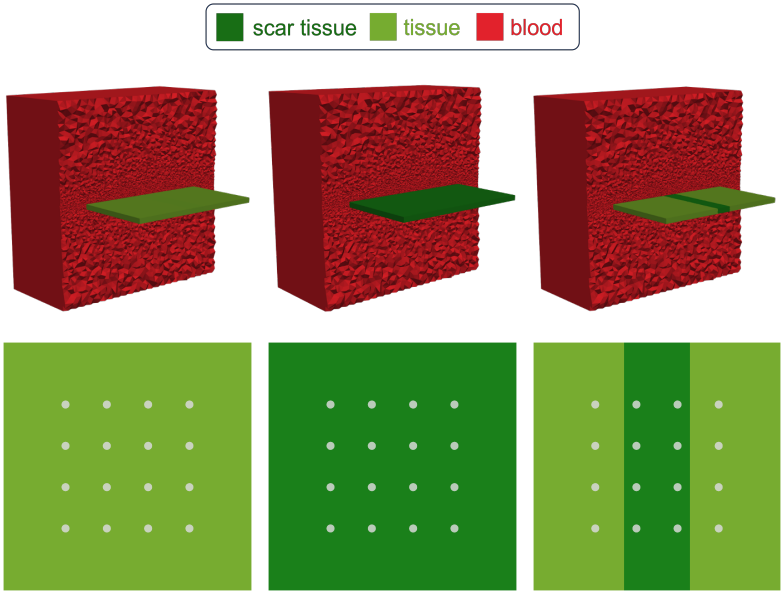

(a) Healthy tissue. **(b)** Scar tissue. **(c)** Line of scar 8 mm width.

Figure 7.2: Tissue configurations surrounded by a box of blood represented by a cross section (upper row), and their corresponding top view with the electrodes placed as in the simulation setup (bottom row): (a) homogeneous healthy tissue, (b) homogeneous scar tissue, and (c) healthy tissue with a line of scar tissue.

Table 7.1: Conductivities of relevant materials used in the simulations at 14.5 kHz at body temperature in this work.

Material	Conductivity σ (S/m)	Reference
Platinum electrode	400,000	[149]
PEBA insulator	10^{-7}	
Blood	0.700	[49, 50]
Myocardium	0.164	[49, 50]
Connective tissue (scar)	0.387	[49, 50]

aligned in the same row are depicted in panels (a-d). Here the outer electrodes are the stimulating pair and the inner electrodes the measuring pair. Similarly, for the vertical patterns the electrodes are aligned in the same column. The

stimulating electrodes are placed at the top and bottom and the measurement electrodes in the center, as depicted in panels (e-h).

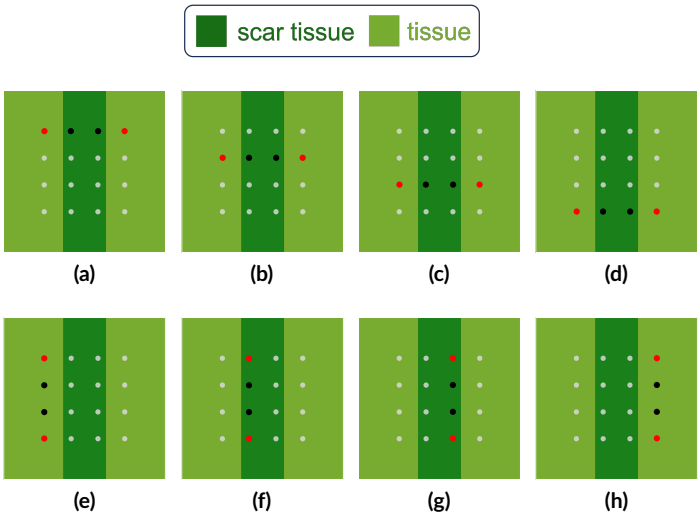

Figure 7.3: Bipolar electrode pairs in horizontal (a-d) and vertical (e-h) patterns for a 4×4 squared catheter mimicking the Advisor™ HD Grid on a slice of tissue with a central line of scar. Grey dots represent electrodes, marked in red if part of the stimulating bipole, or in black if belonging to the measuring bipole.

7.2.4 Forward Simulation

As in Section 5.2.3 and Section 6.2.2, to simulate the spread of the electrical field created by the Rhythmia HDx electroanatomical mapping system (Boston Scientific, Marlborough, MA, USA), an alternating current of 5 µA peak-to-peak amplitude at 14.5 kHz was modeled using the software EIDORS v3.10 [150] in MATLAB R2023b (The MathWorks, Inc., Natick, MA, USA). Combining eight stimulation patterns, four catheter-tissue distances, and three geometrical setups, the analysis comprised 96 simulated LI measurements.

7.3 Results

7.3.1 Catheter-Tissue Interaction

Increasing the catheter-tissue distance yielded monotonously decreasing LI values. As shown in Table 7.2, starting at a median LI value of 63.91 Ω across the eight measurements in healthy tissue at direct contact, the median LI decreased to 62.80 Ω, 60.80 Ω, 58.46 Ω, and 56.02 Ω, each time the catheter moved 0.5 mm away from the tissue, respectively. This represents a 2% decrease after the first loss of contact at 0.5 mm distance, scaling to 3%, 4%, and 4% decrease of the LI with increasing catheter-tissue distance.

Similarly, in Table 7.3 the decreasing effect can be seen in scar tissue. At direct catheter-tissue contact, the median LI value was 52.77 Ω, decreasing between 0.5 and 2% each step, meaning 52.50 Ω, 51.76 Ω, 50.76 Ω, and 49.80 Ω, respectively. Not only the median value at direct contact, but also the drop percentage as the catheter moved away from the tissue were lower in scar tissue than in the healthy patch.

7.3.2 Tissue Characterization

Theoretically, LI drops in the surroundings of myocardial scarred tissue due to the lower conductivity of healthy myocardium in comparison to connective tissue. It can be observed in Table 7.2 and Table 7.3 that scar tissue always yielded lower LI values than healthy scenarios. When comparing median measurements at direct catheter-tissue contact, LI on healthy tissue exceeded the value on connective tissue by 17%.

Table 7.4 shows the LI data corresponding to healthy tissue with a transmural scar line of 8 mm width in the center. Overall, the median LI value across all adjacent bipoles at direct catheter-tissue contact was 58.51 Ω, which was 9% lower than for myocardial tissue and 10% higher than for connective tissue. This median value therefore lays in between the measured values on homogeneous tissue patches.

Accounting for the location of bipolar pairs, horizontal bipoles recorded their respective LI measurements across the scar line, whereas vertical pairs

were located completely on either healthy or scar tissue. Horizontal pairs measured 57.65 Ω, 57.55 Ω, 57.59 Ω, and 57.63 Ω at direct contact. These measurements were in line with LI values being in between healthy and scarred tissue. On the contrary, vertical pairs showed clear differences between the outer adjacent pairs measuring 63.07 Ω and 63.05 Ω, and the internal adjacent pairs obtaining 55.80 Ω and 55.77 Ω, matching the expected values according to the tissue beneath the electrodes involved.

7.4 Discussion

In Chapter 5, an *in silico* framework to measure local electrical impedance in atrial tissue was presented. In that previous work, only tip ablation catheters were employed, leaving room for the extension of its implementation to multi-electrode mapping catheters.

Increasing the distance between the catheter and the tissue yielded monotonously decreasing *in silico* LI results. The simulated LI values never overlapped between measurements on homogeneous healthy and scar tissues. LI measured at the furthest tested distance on healthy tissue never reached the LI measured at direct contact in homogeneous scar tissue, being approximately 3 Ω higher. Nevertheless, that was not the case for the tissue with a scar line. *In silico* LI 2 mm apart from the tissue ranged from 51.71 Ω to 55.51 Ω depending on the bipoles in use, laying within the margin of LI measured in homogeneous scar tissue between direct contact and a catheter-tissue distance of 1 mm. However, these results were never in the range of healthy tissue LI. When considering the clinical application of LI as mapping feature, it is crucial to strike a balance between misidentifying healthy tissue as scar and vice versa.

The presence of a scar line altered the LI measurements compared to the healthy homogeneous tissue patch. Depending on the location and direction of the measuring and stimulating patterns, the results were closer to those obtained on healthy myocardium than on scar tissue. As it can be seen in Figure 7.3 (a-d), injected current through horizontal bipoles crossed the scar line, yielding to LI values corresponding to the range in between healthy and scar tissue. However, vertical bipoles were located completely either on healthy or scar tissue. Outer vertical bipoles, as in Figure 7.3 (e) and (h), were located fully in healthy tissue and thus, showed similar LI values than in a homogeneous healthy patch. On the

contrary, LI measured at inner vertical pairs located on scar tissue, as depicted in Figure 7.3 (f) and (g), decreased in comparison to measurements taken by outer vertical pairs and horizontal pairs, however their values were still far from measurements recorded on homogeneous scar tissue. The results from this work may indicate that not only the properties of the tissue directly underneath the electrodes but also the nearby area is relevant when characterizing atrial substrate by means of LI.

7.5 Conclusion

In this work, an *in silico* model with a 4×4 grid catheter located over a simplified cardiac tissue patch was employed to study the potential use of local electrical impedance measurements in multielectrode mapping catheters. Several stimulating and measuring bipolar pairs were tested to account for the characterization of a vast majority of the tissue surface. Forward simulations of the electrical field provided a better understanding of the effects of scar tissue presence and catheter-tissue distance on the overall measured LI. The resulting environment and simulations represent a valuable starting point to deeper study the incorporation of LI into the clinical mapping field and optimize future catheter development.

Table 7.2: LI simulated values measured at each adjacent bipole (columns) with increasing catheter-tissue distance (rows) in a homogeneous healthy tissue patch.

Distance (mm)	LI in healthy tissue (Ω)							
0.0	63.97	63.85	63.89	63.94	63.96	63.85	63.84	63.95
0.5	62.80	62.78	62.79	62.82	62.93	62.70	62.70	62.86
1.0	60.87	60.71	60.75	60.81	60.87	60.80	60.75	60.84
1.5	58.45	58.33	58.28	58.38	58.44	58.27	58.32	58.38
2.0	56.06	55.98	55.98	56.11	56.05	55.96	55.93	56.11
								

Table 7.3: LI simulated values measured at each adjacent bipole (columns) with increasing catheter-tissue distance (rows) in a homogeneous scar tissue patch.

Distance (mm)	LI in scar tissue (Ω)							
0.0	52.81	52.73	52.77	52.79	52.81	52.73	52.72	52.81
0.5	52.57	52.48	52.49	52.50	52.59	52.45	52.41	52.53
1.0	51.81	51.69	51.72	51.76	51.81	51.76	51.72	51.78
1.5	50.84	50.74	50.69	50.77	50.83	50.68	50.73	50.77
2.0	49.83	49.76	49.76	49.87	49.82	49.74	49.72	49.87
								

Table 7.4: LI simulated values measured at each adjacent bipole (columns) with increasing catheter-tissue distance (rows) in a healthy tissue patch with a centered 8 mm line of scar.

Distance (mm)	LI in tissue with line of scar (Ω)							
0.0	57.65	57.55	57.59	57.63	63.07	55.80	55.77	63.05
0.5	57.84	57.75	57.77	57.80	62.06	55.36	55.33	61.99
1.0	56.93	56.81	56.85	56.88	60.05	54.42	54.36	60.00
1.5	55.43	55.30	55.24	55.34	57.67	53.00	53.00	57.58
2.0	53.78	53.71	53.71	53.82	55.35	51.75	51.71	55.41
								

PART IV

INVERSE RECONSTRUCTION OF ATRIAL TISSUE CONDUCTIVITY

Chapter 8

Inverse Reconstruction with a Circular Multielectrode Catheter

In this chapter, an intracardiac electrical impedance tomography (EIT) environment for multielectrode mapping catheters is presented. This aims to study the local impedance (LI) reconstruction of tissue as surrogate for atrial substrate. Several *in silico* distributions of scar tissue exploring the potential distribution of an LI mapping catheter are conducted to this purpose.

The content of Chapter 8 was developed in strong collaboration with Laura Unger, a previous researcher from the Institute of Biomedical Engineering at Karlsruher Institut für Technologie (KIT). The study was firstly explored by Laura Unger, and the following concept was discussed and improved simultaneously by both. The geometrical simulation setting was developed in parallel by both. The analysis of first results and figures were performed by Laura Unger for her PhD Thesis. Overall, decisions in the implementation of the code and subsequent improvements were discussed by both. As a result, it was previously published under the CC-BY license in Chapter 8 of her PhD Thesis [46] in 2022. Its content has been rephrased with the consent of the author.

8.1 Introduction

As described in Chapter 5, the usage of electrical impedance has a long story in the medical and biomedical field. Previous studies like the ones carried out by Gabriel et al. [48] demonstrated the different dielectric properties of several biological tissues. These characteristics have been used by EIT techniques in the medical field and especially in the lungs, as explained in Section 3.4. By injecting an alternating current between a pair of electrodes lower than the MHz range, the spatial conductivity distributions are reconstructed measuring the potential difference created using another pair of electrodes. In the specific case of the lungs, this method is employed to monitor the ventilatory state of the lungs in a non-invasive way thanks to the contrast between the conductivity of the air and the tissue. Currently, impedance measurements, and more specifically LI measurements, have also gained attention as a novel real time indicator for durable lesion formation and proper catheter-tissue contact during radio frequency delivery. The benefits from LI over classical impedance measurements rely mainly on the lack of other body structures as the lungs and torso in general, which used to limit the value of the previously used generator impedance. However, the classical problem shown by EIT techniques remains, and the resolution keeps being a limiting factor. Lately, researchers have attempted to monitor the temperature changes caused by radio frequency ablation delivery using EIT principles. This approach employs a skin grid of chest electrodes in combination with an intracardiac catheter, aiming to reconstruct the tissue heating using a tomographic multielectrode system [168]. However, some impedance related artifacts, such as respiratory ventilation and muscular interferences, have been identified. Other experimental studies [169, 170] found a successful composite of intracardiac and external electrodes that reconstructed the demarcation and depth of ablation lesions.

The novel DirectSense™ technology [40], integrated into the Rhythmia HDx electroanatomical mapping system, acquires point-by-point impedance measurements without the need of a reference skin electrode. This feature does not provide tomographic results, but on the contrary it includes a four-terminal circuit in the same catheter. The biggest advantage of these circuits, with two separate pairs of electrodes to inject and measure the current, is the absence of influence on the measurement of the contact impedance between the electrode

and the subject. The so-called LI has clinically gained attention as another modality for atrial substrate assessment as it does not rely on the dynamically changing electrical activity of the heart. An LI drop, caused by a combination of resistive tissue heating and subsequent myocardial destruction and lesion formation, serves as an indicator of good lesion performance [40, 89]. Beyond monitoring ablation lesion formation, LI has demonstrated potential in characterizing cardiac tissue and distinguishing between healthy myocardium and fibrotic or scar tissue [2, 3, 90]. Moreover, *in human* studies carried out by Unger et al. [128] have also proved the capabilities of LI to complement low voltage mapping by acquiring full intraatrial maps. However, as mentioned above, there are some confounding factors that represent significant inconveniences when it comes to achieve quantitative LI mapping the way we can think on electrogram (EGM)-based substrate characterization nowadays.

This work introduces an intracardiac EIT environment that could be implemented for any multielectrode mapping catheter. It aims to study the LI reconstruction of tissue as surrogate for atrial substrate. Several *in silico* distributions of scar tissue are used to test the potential arrangement of an ideal LI mapping catheter. By exploring the clinically available multielectrode recording systems in the market, we aim to discover future clinical potential of LI mapping and real applicability of this new technique.

8.2 Methods

8.2.1 Geometrical Setup

An *in silico* environment was developed for simulating the forward propagation of the electrical field, as illustrated in Figure 8.1 (a). A tissue patch measuring $36\,\text{mm} \times 36\,\text{mm} \times 2.5\,\text{mm}$ was embedded into a box of blood of measures $40\,\text{mm} \times 40\,\text{mm} \times 25\,\text{mm}$. A flat circular catheter with a variable number of electrodes was centrally placed above the tissue mimicking clinically available Achieve Advance™ (Medtronic, Dublin, Ireland), Advisor™ FL circular mapping catheter (Abbott, Chicago, IL, USA), or LASSO™ catheter (Biosense Webster, Irvine, CA, USA). Its circular configuration including 10 electrodes is depicted in Figure 8.1 (b). The radius r_L was varied $\in \{7.5\,\text{mm}; 12.5\,\text{mm}\}$ to

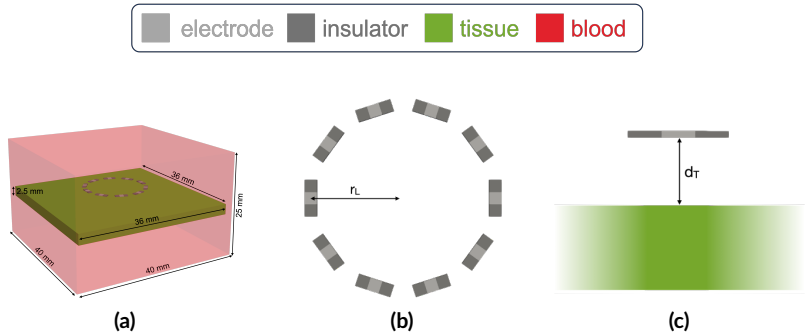

Figure 8.1: Geometrical setup to simulate forward electrical propagation. (a) A tissue patch is located inside a blood box, and a series of electrodes is hanging above the tissue. The catheter is represented with cuboid electrodes, but the setup is equal for the rest of catheter and electrode arrangements. (b) Top view of the circular catheter geometry with radius parameter, and (c) front view of an elevation showing its position above the tissue surface in cross-section. Image modified with permission from [46].

incorporate typical clinically available samples. The catheter-tissue distance d_T, as schematically displayed in Figure 8.1 (c), was varied from 0 to 2 mm in steps of 0.5 mm.

Five different electrode configurations were implemented, including a zero-dimensional point electrode and four three-dimensional geometrical electrodes, as illustrated in Figure 8.2. The spherical electrode was characterized by a radius $r_S \in \{0.25\,\text{mm}; 0.50\,\text{mm}; 0.75\,\text{mm}\}$. The cylindrical electrodes consisted of a central conducting part flanked by insulating cylinders on both lateral sides. The cylinder's radius $r_C \in \{0.25\,\text{mm}; 0.50\,\text{mm}; 0.75\,\text{mm}\}$, the length of the conductor $l_C \in \{0.5\,\text{mm}; 1.0\,\text{mm}; 1.5\,\text{mm}; 2.0\,\text{mm}\}$, and the length of each insulator segment $l_I = 1\,\text{mm}$ parameterized the cylindrical electrode. Similarly, the cuboid electrode was modeled with a central conducting part surrounded by insulating segments on both laterals. The fixed height $z_C = 0.2\,\text{mm}$ was combined with varying width and length of the conductor segment $x_C = y_C \in \{0.5\,\text{mm}; 1.0\,\text{mm}; 1.5\,\text{mm}\}$. The adjacent insulating segments measured $l_I = 1\,\text{mm}$ in length. Finally, the cuboid electrode with a rear insulator was defined according to the previous cuboid electrode, adding an insulating plate surface of height $h_I = 0.1\text{mm}$ covering the surface in opposite direction to the tissue. In total 22 distinct electrodes resulted from the described combinations of

parameters. All variations reported summed up to 22 electrodes × 2 catheter arrangements × 5 distances = 220 geometrical setups.

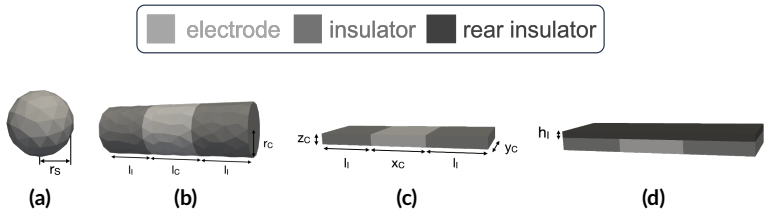

Figure 8.2: Four three-dimensional electrode geometries and their defined variable parameters: (a) spherical, (b) cylindrical, (c) cuboid, and (d) cuboid with rear insulator. Image modified with permission from [46].

For each geometrical setup previously described, six different tissue configurations depicted in Figure 8.3 were employed, encompassing homogeneous physiological tissue, an equal division of physiological tissue and scar, a central scar line with a width of 1 mm, a central scar line with a width of 3 mm, a central cylinder of scar tissue with a radius of 2 mm, and a central cylinder of scar tissue with a radius of 5 mm. All scars were fully transmural, meaning that they occupy the totality of the tissue patch thickness. Consequently, 1320 different scenarios, as a result from 220 geometrical setups × 6, were simulated and subsequently reconstructed as described in following sections.

8.2.2 Material Properties

Similarly to previously presented in Chapter 5, Chapter 6, and Chapter 7, the tetrahedral elements of the mesh were assigned characteristic conductivity values for the respective material at $f_1 = 14.5\,\text{kHz}$ and $f_2 = 2.5\,\text{MHz}$, as described in Table 8.1 for body temperature, i.e. σ_1 and σ_2. f_1 was chosen to match the frequency implemented in the DirectSense™ [40] by the Rhythmia HDx electroanatomical mapping system (Boston Scientific, Marlborough, MA, USA) used in the clinics. f_2 was chosen as a secondary frequency needed when employing a frequency-difference imaging technique.

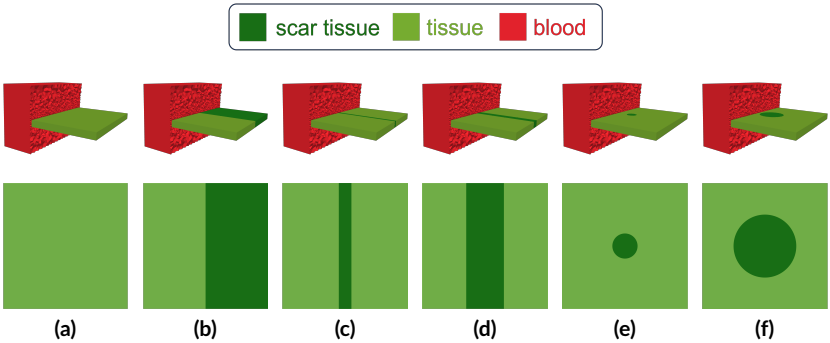

Figure 8.3: Different pathological configurations of scar tissue and homogeneous control tissue surrounded by a box of blood represented by a cross-section (top row) and their corresponding top view (bottom row): (a) healthy homogeneous tissue, (b) half scar, (c) line of 1 mm width scar, (d) line of 3 mm width scar, (e) cylinder of 2 mm radius scar, and (f) cylinder of 5 mm radius scar. Image modified with permission from [46].

In Figure 8.4, the conductivity spectra of human blood, myocardial tissue and connective tissue is displayed. The latter was chosen as the most similar to represent scar tissue due to its composition primarily of extracellular fluid, which causes minimal variations in terms of conductivity along different frequencies. In opposition to that behavior, the conductivities of blood and myocardial tissue rise with increasing frequency, mainly attributed to the enhanced accessibility of intracellular space as the capacitive impedance of cell membranes decreases along higher frequencies.

In time-difference imaging techniques, two measurements at different points in time are usually employed, being able to capture variations in the spatial distribution of the conductivities under study. One of the images is designated as the reference background for difference imaging. Instead of acquiring a second measurement at a different point in time, the background image can be synthetically computed assuming a uniform background, so the reconstruction process adjusts for deviations with respect to the homogeneity. Two different homogeneous background conductivities were then employed, as specified in Table 8.1, where σ_{BI} refers to the conductivity of myocardial tissue. On the contrary, as the specific conductivity of healthy myocardium is usually not known in practice, σ_{BII} was chosen to be a slightly lower value than both myocardium and connective tissue conductivities.

Table 8.1: Conductivities of employed materials for body temperature at frequencies used in the simulations, $f_1 = 14.5\,\text{kHz}$ and $f_2 = 2.5\,\text{MHz}$.

Material	Conductivity σ_1 (S/m)	Conductivity σ_2 (S/m)	Reference
Platinum electrode	$400,000$	$400,000$	[149]
PEBA insulator	10^{-7}	10^{-7}	
Blood	0.700	0.958	[49, 50]
Myocardial tissue	0.164	0.398	[49, 50]
Connective tissue / scar	0.387	0.395	[49, 50]
Homogeneous background I (σ_{BI})	0.164	(-)	
Homogeneous background II (σ_{BII})	0.150	(-)	

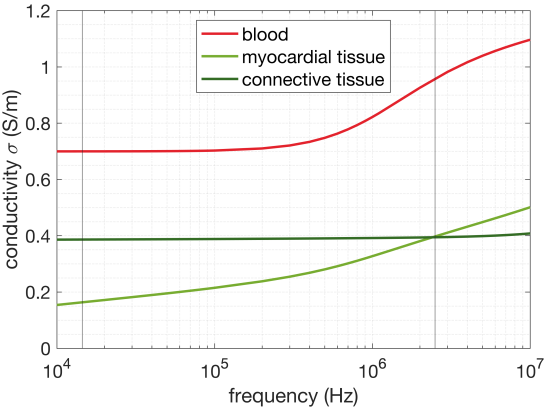

Figure 8.4: Conductivity of blood and specific tissue types (myocardial and connective) used in the conducted simulations at frequencies between 10 kHz and 10 MHz. Vertical lines point out the frequencies employed in this study $f_1 = 14.5$ kHz and $f_2 = 2.5$ MHz. Data taken from [49, 50]. Image reproduced with permission from [46].

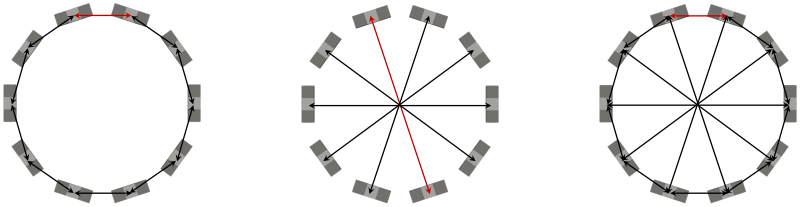

(a) Adjacent bipoles. **(b)** Opposite bipoles. **(c)** All bipoles.

Figure 8.5: Patterns of bipolar (a) adjacent, (b) opposite, and (c) combination of both pairs for the circular catheter. Cuboid electrodes are represented from a top view, with black arrows denoting measuring bipolar pairs and red arrows depict one exemplary injecting bipolar pair of each pattern. Image modified with permission from [46].

8.2.3 Stimulation Pattern

For the current stimulation, two distinct patterns of bipolar pairs of electrodes were defined. Adjacent pairs accounted for directly neighboring electrodes, whereas opposite pairs linked two electrodes in opposition to each other, which in this 10-electrode catheter referred to those with exactly five electrodes distance between them. In Figure 8.5, adjacent and opposite pairs are depicted in panel (a) and (b), respectively. With these distinct patterns, three sets of stimulation were employed: only using adjacent bipolar pairs, only using opposite bipolar pairs, and a third one combining both adjacent and opposite approaches. For each set of stimulations, each bipolar pair belonging to the pattern was employed as stimulating pair once. The remaining pairs which were not part of the stimulating electrodes were used as measuring pairs to always account for the employment of a four-terminal circuit. At each simulated scenario, the three sets were individually computed.

8.2.4 Forward Simulation

The method employed in this work, as described in Section 3.4.1, simulates the spread of the electrical field. Using the software EIDORS v3.10 [150] in MATLAB (The MathWorks, Inc., Natick, MA, USA), an alternating current of 5 µA peak-to-peak amplitude at 14.5 kHz was modeled. This software primarily solves the Laplace equation that describes the distribution of electrical potentials, which depends on the given conductivities $\boldsymbol{\sigma}$ at the different elements of the model and the injected currents I of the electrode model with $v = \mathscr{F}(\boldsymbol{\sigma}, I)$. The complete electrode model was used for all the conducted simulations. A set of M bipolar measurements was gathered to conform the measurement vector $\boldsymbol{v} = [v_1, v_2, \ldots, v_M]$, which was provided as input together with the geometrical mesh to the inverse reconstruction pipeline.

8.2.5 Inverse Reconstruction

After the forward calculation, an inverse reconstruction following the method described in Section 3.4.2 was performed. This process involves the calculation of

the Jacobian matrix $\mathscr{J}$ and the subsequent least square residuals minimization. Both zero-order Tikhonov and the Laplace regularization methods were applied varying the regularization parameter $\lambda = 10^x$ with x ranging from -7.5 to -4.5 in steps of 0.5. Three distinct difference imaging approaches were employed: 1) frequency-difference imaging with two different frequencies $f_1 = 14.5\,\mathrm{kHz}$ and $f_2 = 2.5\,\mathrm{MHz}$, 2) time-difference imaging with a homogeneous tissue background conductivity $\sigma_{\mathrm{BI}} = 0.164\frac{\mathrm{S}}{\mathrm{m}}$ matching myocardial conductivity, and 3) time-difference imaging with a homogeneous tissue background conductivity $\sigma_{\mathrm{BII}} = 0.150\frac{\mathrm{S}}{\mathrm{m}}$ slightly lower than both myocardium and connective tissue conductivities.

For the time-difference imaging approach, all tissue elements were assigned either σ_{BI} or σ_{BII} as conductivity, whereas the blood elements remained unchanged.

The inverse reconstruction was conducted on a two-dimensional mesh with three-dimensional electrode positions projected onto the tissue surface. The surface enclosed by the catheter outline was expanded radially by 1.5 mm and re-meshed with triangles of an average length of 0.2 mm.

Combining two regularization matrices, seven parameterizations of λ, three different stimulation patterns, and three background images, the analysis resulted in 126 reconstruction parameterizations. Taking into account the previously mentioned 1,320 geometrical scenarios, a total of 166,320 reconstructions were examined.

8.2.6 Reconstruction Quality

The reconstruction quality was evaluated mainly by two metrics: the correlation coefficient and the mutual information. Both metrics compared the ground truth of the spatial distribution of conductivities with the corresponding reconstructed image information.

8.3 Results

The shape of the totality of the pathological geometries was successfully reconstructed. Based on the chosen parameters and setup geometries, their reconstruc-

tion quality varied as will be discussed in the following. Absolute conductivity values were not given importance, as the study aimed on reconstructing differences in conductivity with comparison to the respective background image.

In Figure 8.6, the ground truth conductivity distributions and their corresponding reconstructed images are represented. The shapes of all distributions were correctly reproduced, although detailed size distinctions were more challenging due resolution restrictions in the chosen colorbar limits, which were set to the minimum and maximum individual values of each reconstruction. This range was narrower for smaller scar structures, namely the 1 mm line and 2 mm cylinder, in comparison to larger scar structures, such as the 3 mm line and 5 mm cylinder.

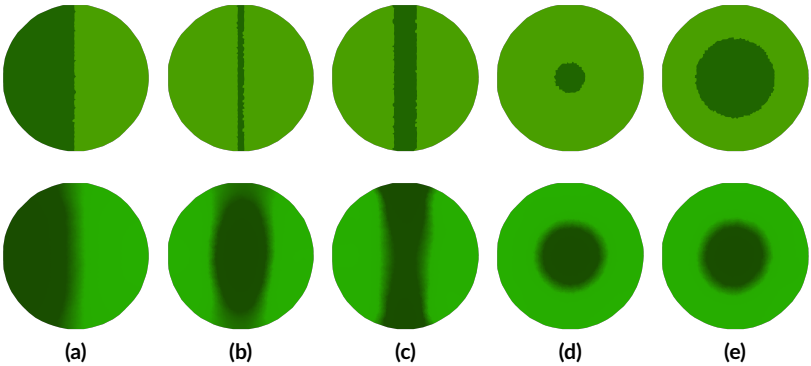

Figure 8.6: Pathological configurations of scar tissue defined as ground truth (top row) and one of their corresponding relative conductivity reconstruction examples (bottom row) for a circular catheter radius of 7.5 mm. The colorbar of the reconstructed images was individually scaled for each example from the maximum to the minimum relative conductivity value. Healthy myocardium is depicted in light green, whereas scar tissue is represented in dark green. The reconstruction was conducted using adjacent stimulation patterns, a frequency-difference reconstruction method, and a Laplace regularization parameter $\lambda = 10^{-6.5}$: : (a) half scar, (b) line of 1 mm width scar, (c) line of 3 mm width scar, (d) cylinder of 2 mm radius scar, and (e) cylinder of 5 mm radius scar. Image reproduced with permission from [46].

8.3.1 Reconstruction Parameters

At the beginning, the performance of different reconstruction parameters was evaluated using non-dimensional point electrodes with direct catheter-tissue contact as exemplary setup configuration. The reconstruction method was influenced by the choice of several factors, such as the regularization matrix, the regularization parameter, the background image, and the stimulation pattern. For the analysis of other parameters, such as the catheter radius, the pathological configuration, the electrode geometry, and the catheter-tissue distance, all simulations contributed to the overall statistics. As depicted in Figure 8.7, the Laplace regularization outperformed the zero-order Tikhonov regularization across all regularization parameter λ choices. Additionally, the use of adjacent current injection showed a slight advantage over opposite current injection. The selection of the regularization parameter had minimal impact on the reconstruction outcome within the analyzed range. In summary, the combination of adjacent current injection with the Laplace regularization and $\lambda = 10^{-7}$ yielded the best performance.

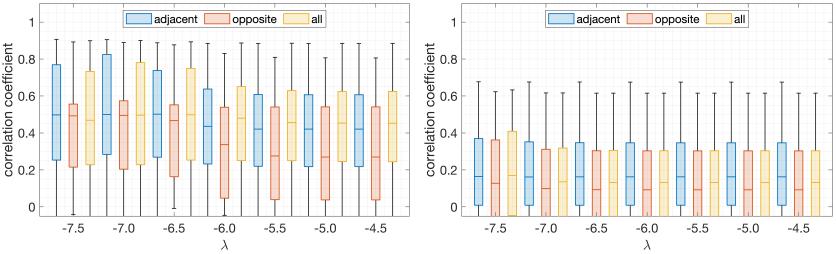

(a) Laplace regularization. **(b)** Zero-order Tikhonov regularization.

Figure 8.7: Correlation coefficients for diverse stimulation patterns using point electrodes and direct catheter-tissue contact. Regularization parameters were chosen to be (a) Laplace and (b) zero-order Tikhonov. Each image depicts the results of using different stimulation pattern: adjacent in blue, opposite in red, and the combination of both in yellow. The horizontal axes represents the variation of x as part of the regularization parameter $\lambda = 10^x$. Image reproduced with permission from [46].

Figure 8.8 illustrates the comparison of different reconstruction methods depending on their impact on the reconstruction parameter. The Laplace regularization consistently outperformed the zero-order Tikhonov regularization. The frequency-difference imaging approach yielded the best results for the Laplace regularization, closely followed by the homogeneous background image with σ_{BI} matching the conductivity of healthy myocardium. An homogeneous background image with σ_{BII} represented by a biased conductivity value resulted in the poorest performance for the Laplace regularization. The influence of the parameter λ on the reconstruction quality was minimal, particularly in the context of frequency-difference imaging.

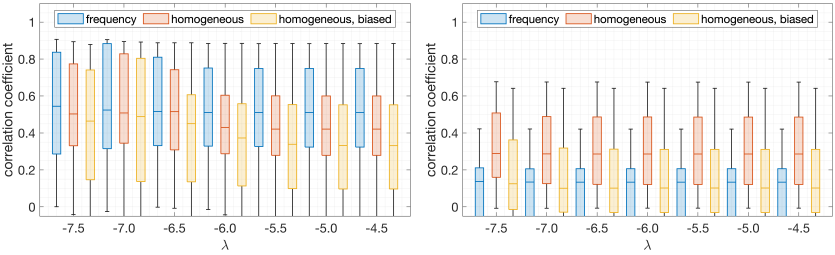

(a) Laplace regularization. **(b)** Zero-order Tikhonov regularization.

Figure 8.8: Correlation coefficients for diverse reconstruction parameters using point electrodes and direct catheter-tissue contact. Regularization parameters were chosen to be (a) Laplace and (b) zero-order Tikhonov. Each image depicts the results of using different reconstruction method: frequency-difference in blue, homogeneous background with σ_{BI} in red, and homogeneous biased background with σ_{BII} in yellow. The horizontal axes represents the variation of x as part of the regularization parameter $\lambda = 10^x$. Image reproduced with permission from [46].

8.3.2 Geometrical Setup

The actual geometric arrangement significantly impacted the quality of the reconstruction. For all the comparisons, only the optimal set of reconstruction parameters was selected for each specific arrangement. The most commonly used method for the reconstruction – but not the exclusive one – was frequency-

difference with a regularization parameter $\lambda = 10^{-7}$ using a Laplace constraint and adjacent bipolar pairs for both current injection and measurement.

In Figure 8.9 (a), the pronounced influence of pathological geometry on the reconstruction quality is depicted. Coarser pathological setups, such as the even split of the tissue in healthy myocardium and scar, yielded correlation coefficients highly clustered around 0.9. The poorest reconstruction quality was observed in setups with finer structures, such as the 1 mm-wide line of block. In parallel, the catheter-tissue distance did show minimal impact on the reconstruction quality, as shown in Figure 8.9 (b).

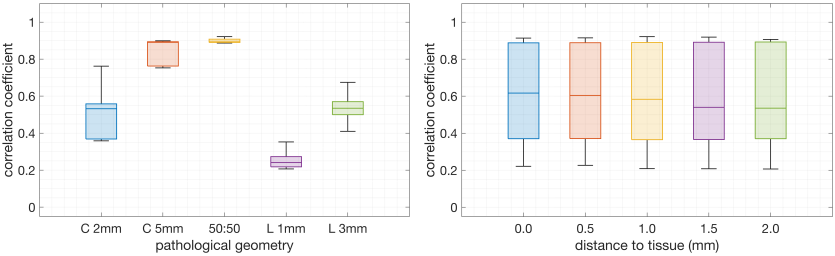

(a) Pathological geometries **(b)** Catheter-tissue distances

Figure 8.9: Correlation coefficients for: (a) different pathological geometries, and (b) catheter-tissue distances. In panel (a), pathological geometries are coded as: C being cylinder, L being line, 50:50 for the even split in healthy myocardium and scar tissue, and y mm meaning the width or radius of the respective setup. Only the best choice of the rest of reconstruction parameters is displayed for each individual setup. Image reproduced with permission from [46].

Figure 8.10 (a) depicts the impact of electrode geometry on the reconstruction quality. Point electrodes exhibited a slightly superior correlation coefficient compared to the three-dimensional electrodes. Among them, neither the size nor the geometry had a strong influence on the reconstruction quality. On the contrary, varying the radius of the catheter produced notable changes in the results, leading to better reconstruction quality when using a smaller radius of 7.5 mm.

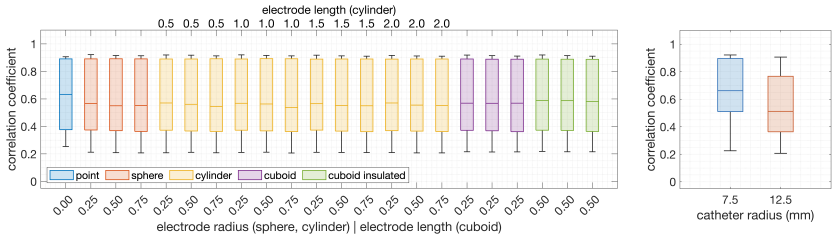

(a) Electrode types **(b)** Catheter radii

Figure 8.10: Correlation coefficients for: (a) different electrode types and (b) catheter radii. In panel (a), point electrodes are depicted in blue, spherical electrodes in red, cylindrical electrodes in yellow, cuboid electrodes in purple, and cuboid electrodes with roar insulator in green. The corresponding geometrical dimensions are annotated on the top and bottom of the horizontal axis. Only the best choice of the rest of reconstruction parameters is displayed for each individual setup. Image reproduced with permission from [46].

8.4 Discussion

This study is the first to evaluate the potential of EIT in reconstructing the relative conductivity of atrial tissue using *in silico* measurements recorded with a multielectrode mapping catheter.

8.4.1 Reconstruction Parameters

All implemented pathological geometries were successfully reconstructed from measurements obtained at a centered catheter position. However, the accurate determination of the pathological structure to their actual extent posed a challenge due to the absence of an absolute reference. Comparisons of reconstructed images using a common reference suggested that the extent of structures could be compared more reliably. In general, coarser structures exhibited higher reconstruction quality than fine structures, which was attributed to the limited resolution of the tomographic approach and led to blurring and lower contrast in the reconstruction of finer structures.

The choice of the reconstruction quality measure is crucial. Both the correlation coefficient and mutual information were used in this study, yielding similar

results. Nevertheless, the consideration of other additional parameters such as the contrast between regions or relative standard deviation could enhance the quality measure.

When it comes to stimulation patterns, adjacent bipolar pairs for current injection and voltage measurement demonstrated slightly better results than opposite ones. The inferiority of opposite bipolar pairs was attributed to their fewer numbers and longer current paths, reconstructing tissue conductivity over a greater distance. Despite central structures being directly crossed by opposite bipolar pathways, the observed effects still favored adjacent bipolar pairs.

To determine the optimal set of reconstruction parameters, including the regularization parameter and the regularization matrix, a brute force approach was used. Using well-known methods like the L-curve for selecting the regularization parameter could further improve reconstruction quality. In addition, two standard regularization constraints were employed with the Tikhonov and Laplace operator. The exploration of different or even combined regularization constraints for intracardiac applications is recommended. In a clinical setting implementation, a fixed set of parameters or dynamic adaptation based on current measurements would be necessary due to the unavailability of ground truth.

The selection of the background image is critical for difference-based EIT methods. This approach may face challenges in clinical practice implementation due to the unknown conductivity of healthy myocardium, with a random bias negatively influencing the reconstruction. The bloodpool conductivity was assumed as known because it can be easily measured in clinical practice. However, the influence of inaccuracies should be taken into account when using time-difference approaches. Alternatively, frequency-difference imaging represents a more robust choice that avoids the need for a background conductivity assumption by using two different frequencies. Implementing this in clinical hardware, particularly in the MHz range, presents big challenges but promises better outcome.

8.4.2 Geometrical Setup

Despite the apparent lack of influence of the catheter-tissue distance on the reconstruction quality, it is fundamental to acknowledge that the imposition

of constant distances between electrodes and tissue represents a significant limitation. This constraint restricts the applicability of the findings, as slightly elevation of the catheter from the tissue by a few millimeters can result in drops in measured voltage amplitude similar to the presence of pathological structures – as it was previously discussed in Chapter 5. Ensuring consistent catheter-tissue contact is crucial for meaningful measurements. To address this limitation, an extension of this *in silico* study should delve into the effects of varying and uneven distances between electrodes and tissue within a single measurement. Employing ultrasound-based distance measures or contact force (CF) sensors could be instrumental in mitigating any disadvantageous effects stemming from variations in electrode-tissue distances. This additional investigations would provide a more comprehensive understanding of the reconstruction process under realistic conditions where electrode-tissue distances are not fixed.

While there is considerable room for improvement and further investigations, this preliminary study has illuminated the substantial potential of EIT for reconstructing atrial tissue conductivity based on mapping catheter measurements. To validate and expand upon these findings, the next logical steps involve conducting *ex vivo* and *in vivo* studies. Given the existing clinical use of linear catheters including DirectSense™ technology, the transition to human measurements using mapping catheters presents a challenge but is definitively feasible. This advancement could significantly contribute to the clinical application of EIT in understanding and characterizing atrial tissue conductivity in real-world scenarios.

8.4.3 Future Perspectives

The current analysis of the circular catheter only explored one possible electrode arrangement. Advanced high-density mapping two-dimensional catheters, such as the PentaRay™ NAV Eco (Biosense Webster, Irvine, CA, USA) or the Advisor™ HD Grid (Abbott, Chicago, IL, USA), or even three-dimensional ones such as the IntellaMap Orion™ (Boston Scientific, Marlborough, MA, USA), or the Sphere-9™ (Medtronic, Dublin, Ireland), could offer a denser configuration of electrodes. Unlike the circular catheter, these newer proposals cover the central part of the area of interest in a more comprehensive way, eliminating the need for extrapolation of information from the center.

In the previous Chapter 7, an *in silico* model of a grid-shaped catheter, resembling the Advisor™ HD Grid mapping catheter, was geometrically implemented in an effort to address this. By the use of cylindrical and cuboid electrodes with a rear insulator, this model could represent the Advisor™ HD Grid or the IntellaMap Orion™, respectively. The stimulation patterns available in a grid catheter surpass those of a circular catheter, enabling the definition of horizontal, vertical, and diagonal bipoles in addition to the already defined adjacent and opposite pairs. Preliminary thoughts suggested that the reconstruction quality could be further improved by leveraging the advantages of the grid arrangement. The close proximity of neighboring electrodes and the even coverage of the area of interest may be advantageous for reconstruction. Specifically, fine structures, such as a centered cylinder with a 2 mm radius, could potentially be reconstructed in higher detail with a 4×4 grid compared to the circular reconstruction described earlier. Nevertheless, in an effort to implement this geometry in the presented inverse reconstruction pipeline, it yielded no conclusive results presumably due to a non-sparse matrix when including many injection patterns and leading to non convergence of the computational system. However, the improvement of the already implemented method in EIDORS was out of scope and the efforts should be redirected towards the finding of a better solution. Still, a comprehensive study is needed to thoroughly explore and validate the potential enhancements offered by grid-shaped catheters.

Moreover, in this work all pathological configurations were represented as fully transmural and compact scar patterns. The introduction of more realistic fibrosis patches at several depth positions representing endocardial, midmyocardial, and epicardial pathological structures may be of help when accounting for realistic representation of fibrotic structures in the heart. On top of that, not only purely geometrical structures but also diffuse and less compact fibrosis patterns should be taken into account when evaluating the feasibility of incorporating LI mapping in the clinical environment.

As a follow-up of this work, using point electrodes, direct catheter-tissue contact, Laplace regularization and frequency-difference reconstruction, different pathological geometries will be tested towards the implementation of a multielectrode catheter device. In the same way, more diffuse and realistic fibrotic patterns will be included in the next chapter of this thesis to test the feasibility of impedance measurement in the clinics.

8.5 Conclusion

In this work, an *in silico* EIT model to reconstruct relative myocardial tissue conductivity from multielectrode measurements was presented. The model incorporated various relevant scenarios, encompassing factors such as catheter-tissue distance, electrode types, catheter radii, and diverse pathological geometries. By conducting forward simulation and inverse reconstruction of an electrical field on a two-dimensional mesh, an extensive set of parameters were studied. The developed model and simulations lay the groundwork for the optimization of catheter and electrode arrangements specifically tailored for LI measurements. This optimization represents a crucial step towards the potential clinical integration of LI mapping in the EP study and improved characterization of atrial tissue conductivity.

Chapter 9

Local Electrical Impedance in Non Fully Transmural Fibrosis

In this chapter, the performance assessing non fully transmural fibrotic substrate of the previously presented *in silico* electrical impedance tomography (EIT) environment is compared with the widely extended voltage map method based on electrogram (EGM) computation. This work aims to shed some light on local impedance (LI) ability to detect and characterize atrial substrate when it is not extended through a substantial myocardial thickness.

The content of Chapter 9 was previously published as part of the Computing in Cardiology 2023 Proceedings [137]. Most passages in this chapter have been quoted verbatim from the publications and are adapted with permission from the authors. Work presented in Section 9.2.1 and subsequent results were carried out during the master thesis of B.Sc. Nansi Caslli [171].

9.1 Introduction

A standard treatment for atrial fibrillation (AF) involves creating lesions in the pulmonary veins (PVs) to isolate them. In patients with persistent AF, additional ablation lesions can be placed in areas of fibrotic tissue, which can include complex fibrotic patterns that fractionate the wavefront and could potentially promote reentries [172]. During an ablation procedure, mapping techniques

are currently used to estimate the location of these abnormal substrate areas. EGM can be recorded in a unipolar or bipolar technique [39] and can be used to produce local activation time (LAT) and voltage maps to represent the electrical activity of the heart.

While EGM-based substrate mapping has shown inconclusive success, recently, LI has been gaining attention as a surrogate to differentiate pathologically altered substrate due to its independence on the electrical activity [90]. LI may improve the current understanding of underlying substrate, including the possibility of computing full-chamber maps [128].

In this work, we study the ability of EGMs and LI to identify non-transmural fibrosis areas in different locations of the endo-, midmyo-, and epicardium using in silico experiments. By using an EIT system applied to a multi-electrode mapping catheter [46], we aim to explore the possibility to differentiate fibrotic tissue located on the midmyo- and epicardial surface by means of LI mapping where EGMs lose track of the atrial substrate.

9.2 Methods

An *in silico* squared patch of tissue measuring 36 mm $\times$ 36 mm $\times$ 2.5 mm was embedded in a 40 mm $\times$ 40 mm $\times$ 25 mm box that represents the surrounding blood, as depicted in Figure 9.1. A circular catheter with 10 zero-dimensional point electrodes in a circular arrangement of 7.5 mm radius mimicking the Lasso™ catheter (Biosense Webster, Irvine, CA, USA) was placed centrally above the tissue.

Centered below the catheter, 4 fibrosis patterns with different levels of entropy [173], as shown in Figure 9.2, were placed. Each pattern was realized with 4 distinct configurations: endo-, midmyo-, epicardial, and transmural. For the endo-, midmyo-, and epicardial cases, the thickness of the fibrotic area was set to 1.25 mm, i.e. half of the total tissue thickness, varying only its location along the z-axis. The transmural configuration occupied the totality of the tissue thickness. In total, 16 different configurations were studied. Meshes comprising 1,020,544 tetrahedral elements were generated using Gmsh [145].

Mesh resolution of blood and tissue elements was adapted to be the highest surrounding the electrodes and close to the tissue surface, while it decreased for larger distances to the catheter.

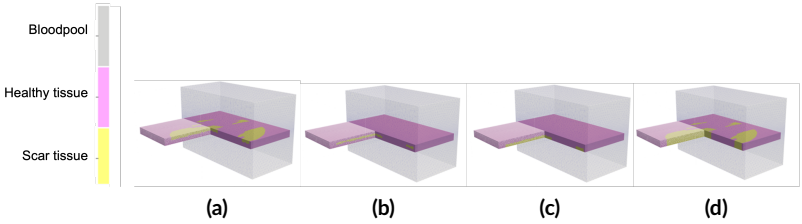

Figure 9.1: Geometrical model setup of one exemplary fibrosis patch in its distinct configurations with cuts along two planes for visualization purposes. Each tissue is surrounded by a blood bath (grey) and its cells are assigned as healthy (pink) or fibrotic (yellow). (a) Endocardial: fibrosis area on the surface of the tissue patch. (b) Midmyocardial: fibrosis area in the middle of the tissue patch. (c) Epicardial: fibrosis area at the bottom of the tissue patch. (d) Transmural: fibrosis area throughout the total thickness of the tissue patch.

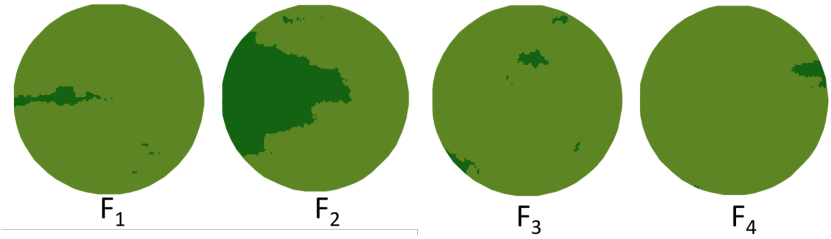

Figure 9.2: Ground truth of each fibrosis pattern F_{1-4}. Light green represents healthy tissue, whereas dark green areas are assigned to fibrosis. F_2 and F_4 show the lowest and highest entropy, respectively.

9.2.1 Electrogram Computation

Electrical propagation in the tissue and its surroundings was simulated by solving the pseudo-bidomain model in openCARP [174]. Cellular electrophysiology was modeled using the ionic model proposed by Courtemanche et al. [52]. A stimulus of 50 μA/cm^2 lasting 2.5 s was placed at one lateral face of the tissue to simulate a planar wavefront.

For healthy tissue, intracellular and extracellular conductivity were set to 0.36 S/m and 1.29 S/m [175], respectively. Similarly, the fibrotic region and the blood were modeled with a conductivity of 10^{-5} S/m, and 0.7 S/m [176].

The extracellular potentials of each point within 9 mm radius measured from the center of the catheter at the surface of the tissue were extracted to compute voltage maps. At each point, the peak-to-peak (p2p) voltage was computed as the difference between the maximum and the minimum value over time. As suggested by Nairn et al. [75], a bipolar voltage threshold of 1 mV was translated to a unipolar threshold of 1.32 mV.

9.2.2 Local Electrical Impedance Simulation

The local electrical impedance simulation was performed as described in the previous chapter. The spread of the electrical field was modeled using the software EIDORS [150] in MATLAB (The MathWorks, Inc., Natick, MA, USA, version 2023b). An alternating current of 5 mA peak-to-peak amplitude at 14.5 kilohertz (kHz) was simulated. Conductivity values at body temperature for blood, healthy tissue, and connective tissue at f = 14.5 kHz were modeled as 0.7 S/m, 0.164 S/m, and 0.387 S/m, respectively [50].

Stimulation, i.e. current injection, was performed using adjacent bipolar electrode pairs. For each set of simulations, each bipolar pair was chosen to be the stimulating pair once and measuring pair the rest of the times, sticking to four-terminal circuits during all sets. Zero-order Laplace discrete regularization with $\lambda = 10^{-7}$ was applied. A time-difference imaging approach with an homogeneous tissue background conductivity σ_{BI} = 0.164 S/m was employed.

On a two-dimensional mesh, three dimensional electrode positions were projected to the surface to perform an inverse reconstruction. The enclosed surface was extended radially by 1.5 mm and meshed with triangles of an average edge length of 0.2 mm.

9.2.3 Comparison Between the Modalities

To compare both mapping techniques, the Pearson correlation coefficient between the two binarized images and the ground truth of each fibrosis configuration was computed.

9.3 Results

9.3.1 Voltage Maps

No fibrosis was recognized for any midmyo- or epicardial structure, as shown in Figure 9.3 (a). Fibrotic structures not located on the surface yielded high voltage values, whereas endocardial and transmural configurations were better identified. However, after applying the voltage threshold, only F_2 in the transmural configuration led to some low voltage extent with a correlation of 0.7.

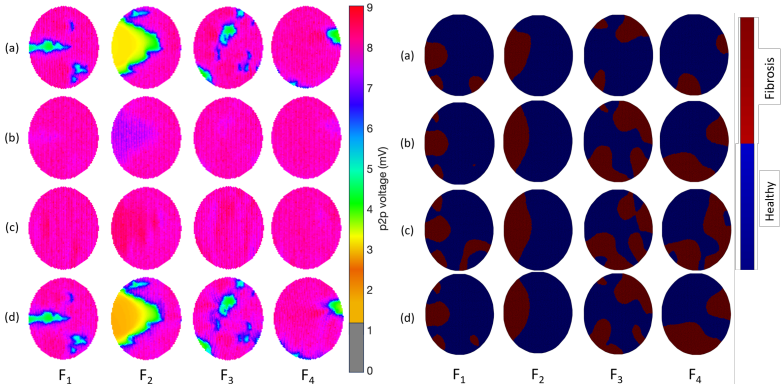

(a) Voltage maps. **(b)** LI maps.

Figure 9.3: Continuous voltage maps (left panel) and binary reconstructed structures (right panel) of four different fibrosis configurations F_{1-4}: (a) endocardial, (b) midmyocardial, (c) epicardial, and (d) transmural. Low voltage values below 1.32 mV are color coded in grey.

9.3.2 LI Maps

Differences in conductivity compared to the respective background image were reconstructed. For all the configurations and patterns, fibrotic structures were identified at some extent, as shown in Figure 9.3 (b). Reconstruction quality varied by pattern, increasing as the entropy of the pattern decreased. Correlation coefficients are detailed in Table 9.1.

In the transmural case, the correlation values ranged between 0.16 and 0.72, whereas values between 0.25 and 0.74 were obtained for the endocardial configuration. For midmyo- and epicardial configurations, lower absolute value correlations between 0.03 and 0.68 were observed.

Among the different patterns, correlation values of 0.68, 0.68, 0.72, and 0.74 were obtained for F_2 in midmyocardial, epicardial, transmural, and endocardial configurations, respectively. For the smaller patterns $F_{1,3,4}$, mean correlation values decreased respectively to 0.29, 0.18, and 0.17. A negative correlation of -0.02 was found for F_3 in midmyocardial configuration.

Table 9.1: Correlation values between ground truth structures and relative conductivity reconstruction (LI maps) for each pattern F_{1-4} (columns) and configuration (rows).

	F_1	F_2	F_3	F_4	Mean
Endocardial	0.29	0.74	0.25	0.32	0.40
Midmyocardial	0.24	0.68	0.10	-0.02	0.27
Epicardial	0.33	0.68	0.15	0.18	0.34
Transmural	0.32	0.72	0.19	0.16	0.35
Mean	0.29	0.70	0.17	0.17	

9.4 Discussion

In a previous *in silico* study [46], simple fibrosis patterns were used to explore the capabilities of this new method to account for conductivity changes. Up to the authors' knowledge, no previous works evaluated the ability of voltage and

LI maps to account for realistic fibrosis patterns while examining non-transmural fibrosis configurations in tissue.

Voltage maps were not able to detect any epi- nor midmyocardial fibrosis pattern The threshold used to identify low voltage regions might be too low for this *in silico* setting and could be optimized in future work. LI maps yielded slightly better fibrosis detection. Endocardial configurations showed the best results on average, whereas midmyocardial ones performed worst. Among the fibrotic patterns, F_2 led to an average correlation value of 0.70 due to its compactness. For the voltage maps, both configuration and thickness of the fibrotic area were proven to be of importance. On the other hand, LI can detect fibrosis at different locations in a similar extent but the size of the structure is clearly of importance. However, reconstructed conductivity values were thresholded according to the distance to each relative maximum value. The threshold is a balance between over- and undersensing of potential arrhythmogenic substrate.

In this study, a patch of flat tissue without any anatomical structure or reentry was used. A realistic geometry with a more complex simulation approach, which includes sophisticated fibrosis modeling instead of taking it as a block element, may lead to better outcomes in both methods. Moreover, only a circular catheter setting was employed. The lack of electrodes outside of the circumferential shape causes a loss of information when the structures are located at the innermost parts of this area. Using other two-dimensional catheter setups, such as the Advisor™ HD Grid (Abbott, Chicago, IL, USA), the PentaRay™ NAV Eco (Biosense Webster, Irvine, CA, USA), or even tridimensional ones as the IntellaMap Orion™ (Boston Scientific, Marlborough, MA, USA) or the recently approved Sphere-9™ (Medtronic, Dublin, Ireland) could improve the reconstruction quality when accounting for smaller fibrotic patches located centrally.

In summary, this *in silico* comparison helped to better understand the limits of using voltage for fibrosis detection, as it may lead to underestimation of non-transmural areas. LI is expected to help distinguishing between a healthy atrium and fibrotic areas which are big enough, improving the understanding of underlying substrate and paving the way towards the use of impedance as a readout for non-transmural atrial fibrosis substrate.

9.5 Conclusions

An *in silico* evaluation of voltage and LI-based mapping techniques as a surrogate for atrial substrate was conducted. Locations whose voltage maps were not able to detect any fibrosis extent, the LI reconstruction led to higher correlation values in critical fibrotic areas. Comparing to the ground truth, our simulations achieved good results for endocardial configuration. More catheter and fibrosis configurations with more complex electrical propagation simulations should be implemented for further analysis in the future.

PART V

MULTIELECTRODE LOCAL ELECTRICAL IMPEDANCE MAPPING

Chapter 10

In vitro Local Impedance in a Multielectrode Catheter System

This Chapter explores the potential of using multielectrode catheters as local impedance mapping systems. Changing the focus compared to previous parts of this thesis, this work makes use of *in vitro* experiments to measure impedance on tissue phantoms.

The experiments included in the work presented in Chapter 10 were conducted in the facilities of Boston Scientific in Cambridge, MA, USA. This Chapter is the result of a collaboration over 2 years between the Concepts Team from the R&D Rhythmia Department of Boston Scientific Cardiology in Cambridge and the Biosignals Group at IBT at Karlsruher Institut für Technologie (KIT).

10.1 Introduction

For several decades, attempts have been made to exploit impedance information in medicine, particularly focusing on the varied conductivity of different tissues [48, 50]. Impedance tomography, leveraging tissue conductivity differences, has been recently explored as a valuable tool in medicine and, particularly during this thesis, in cardiac electrophysiology. Local impedance (LI) has emerged as a key player in recent times, providing real-time insights into lesion formation during catheter ablation. The applications of LI extend to

the assessment of effective lesion performance, with a focus on gap detection and conduction block identification. This approach holds promise for mapping and guiding medical interventions, exemplified by the potential role of LI in complementing classical mapping methods [128, 137].

The review of studies presented in Chapter 4 underscores the ability of LI to discern disparities between healthy and scarred myocardium, paving the way for enhanced ablation outcomes and indicating a broader potential for impedance-based mapping techniques in cardiac arrhythmias. An observed drop in LI, resulting from a combination of resistive tissue heating, myocardial destruction, and lesion formation during ablation, serves as a reliable indicator of effective lesion performance, as highlighted in previous studies [40, 89].

Beyond its primary function of monitoring ablation lesions, LI demonstrates promising capabilities in differentiating between healthy myocardium's higher impedance regions and lower values associated with scar tissue [2, 3, 90]. Part of this thesis, previously presented in Chapter 7 and Chapter 9, has demonstrated LI's ability to complement, and at times surpass, the efficacy of low voltage mapping, even providing comprehensive full chamber maps [128, 137].

The main drawback presented by Unger et al. [128] regarding substrate mapping using LI was the lack of contact force sensor within the IntellaNav MiFi™ OI (Boston Scientific, Marlborough, MA, USA). Although the release of IntellaNav Stablepoint™ (Boston Scientific, Marlborough, MA, USA) represents a step forward in this direction, multielectrode catheters rarely include such technology. In such cases, impedance could act as surrogate to assess the difference between catheter-tissue contact and non-contact by position the catheter in the bloodpool.

Leveraging the distinct conductivity characteristics exhibited by various biological tissues within a specific frequency range, LI holds potential for integration into multielectrode catheters. This integration would enable the assessment of myocardial structures through intracavitary recordings, complementing sometimes insufficient electrograms (EGMs). However, as mentioned previously, there are some confounding factors that represent significant inconveniences when it comes to achieve quantitative LI mapping the way we can think on EGM-based substrate characterization.

Building upon the *in silico* work presented in Chapter 8, this study introduces a preliminary set of *in vitro* experiments utilizing a clinically available multielectrode mapping catheter. The primary objective is to investigate the ca-

pability of LI in distinguishing between electrode-tissue contact and no contact by examining phantom tissue contact. To determine how impedance behavior changed among contact settings, stimulating pairs, or along time, comparisons among different measurements were carried out. By delving into the distinctions among different catheter-tissue contact settings, the aim is to uncover and demonstrate the future clinical potential of LI mapping, establishing its real-time sequential applicability as a technique.

10.2 Methods

10.2.1 LI Recording

The Rhythmia HDx electroanatomical mapping system (Boston Scientific, Marlborough, MA, USA) allowed for LI recordings with the Orbiter™ PV (Boston Scientific, Marlborough, MA, USA) catheter.The Orbiter™ PV is a flat circular catheter, similar to the ones studied *in silico* in Chapter 8 and Chapter 9, of variable radius ranging from 14.5 to 25 mm. It includes 14 cylindrical electrodes with an interelectrode distance of 5 mm, as schematically depicted in Figure 10.1 (a). [177].

An alternating current of 5 µA peak-to-peak amplitude was injected at 18.335 kHz between two adjacent electrodes chosen between all available pairs in the catheter during the experiment. This frequency, as previously shown in Figure 3.4, lies in the frequency range that highlights the differentiation in blood and tissue conductivity. The electric field created is influenced by the surrounding elements' electrical properties. To measure this electric field, the potential difference ($\Delta\phi$) is recorded between any remaining catheter electrode and a system reference located in the signal station and isolated from its ground, yielding a unipolar measurement. This measurement will serve to infer the electrical properties of the materials directly around the catheter.

For the current stimulation, adjacent bipolar pairs of electrodes were defined. Each recording made use of a unique pair of neighboring electrodes, (E_i,E_j, with j=i+1) which was varied among several experimental measurements. At each measurement, the remaining electrodes that were not belonging to the injection pattern were available as measuring pairs. Only the electrodes placed at one and

two electrodes of distance from either electrode involved in the stimulating pair were employed as measuring electrodes. An example of one injection pair, the corresponding measuring electrodes, and the rest of the catheter electrodes can be seen in Figure 10.1 (b).

Using Ohm's law, $\Delta\phi$ is divided by the injected current to obtain LI expressed in ohms (Ω). At each measurement, data was recorded for 30 s at a sampling frequency of 20 Hz, generating sets of 590 samples per measurement.

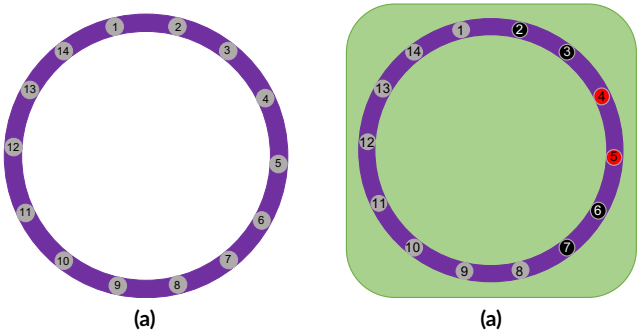

Figure 10.1: Schematic top view representation of the Orbiter™ PV (Boston Scientific, Marlborough, MA, USA) mapping catheter. (a) The 14 equidistant electrodes, in grey, are fitted into an insulating circular tube, in purple. (b) An exemplary case of the catheter located in direct tissue contact (green area) with the electrodes from the injection pattern in red (E_4 and E_5) and measuring ones in black (E_2,E_3, E_6 and E_7).

10.2.2 Experimental Setups

The experimental setup used in this Chapter can be seen in Figure 10.2. In short, it was composed by a tank filled with saline solution in which an adipose tissue phantom sample lies and the catheter was introduced to measure distinct contact settings.

The catheter was introduced in a tank filled with a homogeneous saline bath medium of 3.5 $\frac{g}{L}$ that mimics human blood conductivity [49, 50]. The tank, which had a capacity of 11 L, included a structure to support and elevate

the tissue phantom. Attached to the back part of the tissue support, a fixation allowed to rotate the catheter in an X direction and translating it along the YZ axes. To provide a stable reference required for the signal station, the coronary sinus (CS) catheter was parked at the back wall of the tank. The CS catheter, the DYNAMIC XT™ (Boston Scientific, Marlborough, MA, USA), is a linear catheter with 10 electrodes.

On the bottom part of the back side of the tank, two holes connected through two pipes to a heater machine. One of the pipes took the saline solution from the tank, made it circulate through the heating, and turned it back to the tank. With this constant flow and making use of a thermocouple wire connected to a thermometer, the temperature of the bath was controlled to lie within usual blood ranges (36.6-37.2 °C).

Moreover, two descendant tubes located at the upper back corners of the tank were attached to an irrigation machine. This device was included to maintain a constant circulation of 17 $\frac{\text{ml}}{\text{min}}$. To be sure that the impedance recordings were not affected by the flow, the inflow pipe was not directly pointing to the mapping catheter but parallel to it.

In vitro phantoms with similar conductivity behavior as adipose tissue were employed. To fix the phantoms to the tissue support table, non-conductive metallic needles, i.e. that do not interfere with the electric field, were used. The catheter was placed above the tissue sample or floating in the saline bath to measure their conductivity differences at various contacts, as exemplary depicted with the Orbiter catheter in Figure 10.3 (a) and (b), respectively. Due to the surface irregularities of the tissue samples, aiming for a full contact of all electrodes sometimes was not possible, as we can see in Figure 10.3 (c). Thus, a third contact setting with all electrodes in close proximity to the tissue defined as 1-2 mm catheter-tissue distance was defined, where most of the electrodes were in touch and some others slightly floated in saline.

10.2.3 Data Collection

Due to the change of stimulating pattern among recordings, firstly an automatic detection of the signals from either source and sink electrodes was carried out. By using this method, it was assured that the impedance measured at a certain electrode pair (E) did not depend on the manufacturing setting of the catheter,

i.e. its shape and interelectrode distances, but the actual position with respect to the created electric field. For all recordings, the two closest electrodes to either the source and the sink electrodes were selected: E_{i-2}, E_{i-1}, E_{j+1}, and E_{j+2}, being the electrodes located two and one positions to the left of the source, and one and two positions to the right of the sink, respectively. As the employed catheter was composed of 14 electrodes, in those cases in which the stimulating pair was set to be E_1 and E_2, the two closest electrodes to the source, E_{i-2}, E_{i-1}, were E_{13} and E_{14}, respectively.

Selecting these four electrodes of interest yielded four separated data distributions, which were represented by each one of the 15 measurements recorded, M_x, with x ranging from 1 to 15 and measured in ohms (Ω). In Table 10.1, a more detailed description of each measurement recorded, as well as the stimulating pair, the contact setting, and the time at which the measurement was recorded, can be found.

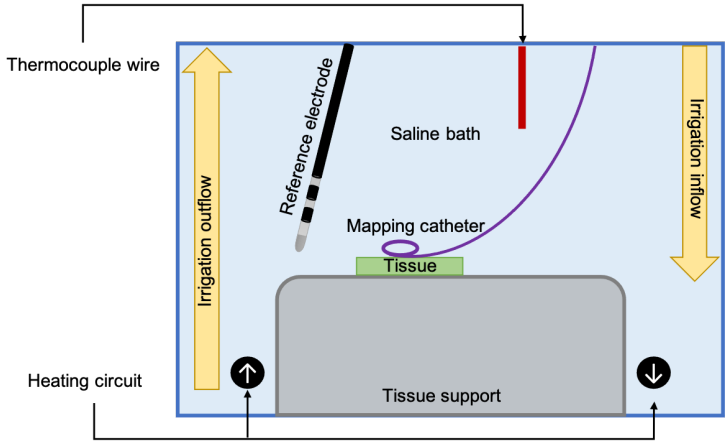

Figure 10.2: Graphical representation of the experimental setup setting used in this *in vitro* work including the mapping catheter in contact with the catheter, as well as other employed materials: heating circuit pipes, thermocouple wire, irrigation flow pipes, tissue support, reference catheter, and tissue phantom.

(a) Floating in saline.

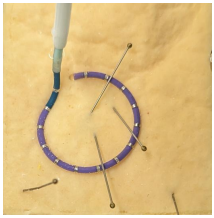

(b) Full contact.

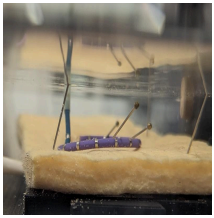

(c) Close proximity.

Figure 10.3: Orbiter catheter in various contact settings: (a) catheter completely floating in the saline bath, (b) catheter with all the electrodes in contact with tissue, and (c) catheter with all electrodes in close proximity to tissue.

Table 10.1: Description of all 15 measurements M_{1-15} recorded including their corresponding stimulating electrodes (E_i and E_j), catheter contact setting (saline, full contact, or close proximity), and recording time (hh:mm:ss.msec).

Measurement n°	Stimulating pair E_i	E_j	Contact Setting	Measurement time hh:mm:ss.msec
M_1	E_1	E_2	Saline	00:00:28.149
M_2	E_1	E_2	Saline	00:00:59.405
M_3	E_3	E_4	Saline	00:02:48.159
M_4	E_5	E_5	Saline	00:05:00.853
M_5	E_5	E_6	Saline	00:05:41.666
M_6	E_5	E_6	Close proximity	00:18:47.741
M_7	E_5	E_6	Close proximity	00:19:28.245
M_8	E_1	E_2	Close proximity	00:20:58.000
M_9	E_1	E_2	Close proximity	00:21:48.482
M_{10}	E_3	E_4	Full contact	00:29:56.160
M_{11}	E_1	E_2	Full contact	00:31:56.767
M_{12}	E_1	E_2	Full contact	00:33:03.249
M_{13}	E_5	E_6	Full contact	00:35:31.048
M_{14}	E_5	E_6	Full contact	00:36:36.272
M_{15}	E_1	E_2	Saline	00:46:46.023

10.2.4 Description of Measurements Comparisons

The previously explained measurements were then compared to account for differences in the contact settings among them. The measured signal was always a voltage between one electrode and a reference point. To get a voltage between

two electrodes, the measured voltage had to be subtracted. Thus, a ratio formula was taken to minimize the influence of the electrode-surface contact impedance at each measurement.

In this ratio, always a reference measurement floating in saline, M_{ref}, and a second measurement in any of the three contact settings, M_x, were used. The reference measurement floating in saline varied depending on the comparison we wanted to address $M_{ref} \in \{M_1, M_2, M_3, M_4, M_5\}$. Similarly, M_{x1} and M_{x2} were selected to be the two measurements to be compared. As some measurements were recorded twice to assess the time evolution, the closest in time to M_{x1} and M_{x2} was chosen. Two populations of impedance measurements to be compared, P_1 and P_2, were obtained:

$$P_1 = \frac{M_{ref} - M_{x1}}{M_{ref}}, P_2 = \frac{M_{ref} - M_{x2}}{M_{ref}}, \tag{10.1}$$

where each one, unitless, is composed by four data distributions reflecting the recording of either electrode of interest. Thus, at each comparison scenario, C_x, a reference measurement M_{ref} and two measurements to be compared, M_{x1} and M_{x2}, were used.

The comparisons were labeled as identical, similar, or different depending on the combination of contact setting and stimulating pair used. Identical comparisons refer to comparisons between two measurements that shared both contact setting and stimulating pair, whereas similar comparisons only shared the contact setting, and different comparisons shared none of them. It is also noted if, independently of their contact setting and stimulating pair, the measurements part of a comparison were recorded consecutively.

To determine how impedance behavior changed among contact settings, stimulating pairs, or along time, 12 comparisons in total, C_{1-12}, were carried out. Table 10.2 condenses the information detailed in the following, describing their comparison label, as well as the measurements involved in either comparison:

1. **C_1:** comparison between two identical consecutive measurements, M_{11} and M_{12}, representing the same full contact position with E_1 and E_2 as stimulating pair and only 1 min of difference between recordings. The reference measurement, M_2, also used E_1 and E_2 as stimulating pair.
2. **C_2:** comparison between two similar measurements, M_{11} and M_{13}, representing the same full contact position using different stimulating pairs (E_1 and E_2 vs. E_5 and E_6) and about 3 min of difference between recordings.

The reference measurement, M_2, used E_1 and E_2 as stimulating pair, matching M_{11}.

3. **C_3:** comparison between two different measurements, M_{11} and M_9, which represent full contact and close proximity settings, respectively. In both cases, as well as in the reference measurement, M_2, E_1 and E_2 are used as stimulating pair.
4. **C_4:** comparison between two identical measurements at the same full contact position, M_{13} and M_{14}, using E_5 and E_6 as stimulating pair and with only 1 min of difference between recordings. The reference measurement, M_5, also used E_5 and E_6 as stimulating pair.
5. **C_5:** comparison between two similar measurements recorded about 3 min apart, M_{11} and M_{13}, using M_3 as reference measurement. Both measurements represent the same full contact position, but the stimulating pairs differ among either the two compared measurements and the reference (E_1 and E_2 vs. E_5 and E_6, vs. E_3 and E_4).
6. **C_6:** comparison between two different measurements, M_{11} and M_8, which represent full contact and close proximity settings, respectively. Both cases employed E_1 and E_2 as stimulating pair, whereas the reference measurement, M_3, used E_3 and E_4.
7. **C_7:** comparison between two different measurements, M_{11} and M_7, representing full contact and close proximity settings, respectively, and using different stimulating pairs (E_1 and E_2 vs. E_5 and E_6). The reference measurement, M_4, shared E_5 and E_6 as stimulating pair with one of the compared measurements, M_7.
8. **C_8:** comparison between two different measurements, M_3 and M_{10}, which refer to the catheter floating in saline and positioned in full contact, respectively, and used E_3 and E_4 as stimulating pairs. The reference measurement, M_1, used E_1 and E_2 as stimulating pair, differing from the compared measurements.
9. **C_9:** comparison between two different measurements, M_{11} and M_3, referring to full contact and floating in saline catheter settings, respectively. M_{11} used E_1 and E_2 as stimulating pair, whereas M_3 employed E_3 and E_4. The reference measurement, M_2, shared the stimulating pair with M_{11}, i.e. electrodes 1 and 2.
10. **C_{10}:** comparison between two similar consecutive measurements, M_3 and M_5, recorded about 2 min apart with the catheter floating in saline

and using different stimulating pairs (E_3 and E_4 vs. E_5 and E_6). The reference measurement, M_1 used E_1 and E_2 as stimulating pair, differing from both compared measurements.

11. **C_{11}:** comparison between two similar measurements, M_2 and M_{15}, sharing E_1 and E_2 as stimulating pair, but representing two different catheter locations floating in saline recorded with 41 min of difference. The reference measurement, M_1, is closer in time to M_2, and shared E_1 and E_2 as stimulating pair with both compared measurements.
12. **C_{12}:** comparison between two different measurements, M_3 and M_{15}, which represented a full contact setting and a catheter floating in saline, respectively. Each compared measurement used a different stimulating pair (E_5 and E_6 vs. E_3 and E_4), which also differed from the electrodes used at the reference measurement, M_1, namely E_1 and E_2.

10.2.5 Statistical Analysis

Statistical analysis was performed with MATLAB R2023a (The MathWorks, Inc., Natick, MA, USA) to establish the comparisons. Initially, a Kolmogorov-Smirnov test was conducted to assess the normal distribution of the populations. If at least one of them rejected the null hypothesis at the 5% significance level, a non parametric tests, such as the Wilcoxon rank sum test for comparing medians, was employed. Alternatively, if the populations showed no deviation from normality, the equivalent parametric test, the two-sample t-test for comparing means, was carried out.

Following the comparison of means or medians, the assumption that the two populations originated from the same distribution was made if the null hypothesis was accepted at the 5% significance level. Conversely, the populations were determined to come from distinct catheter contacts if the p-value was less than 0.05.

10.3 Results and Discussion

The comparison between a certain electrode in contact with an adipose tissue phantom with respect to the catheter completely floating in the bath theoretically yields a higher impedance value. In Table 10.2, it can be observed the contact scenarios that were compared and the obtained results.

Figure 10.4 shows the boxplots corresponding to the results of those comparisons labeled as different, in which two different contacts or a full contact and a measurement in saline, were compared. Due to the conditions of each measurement, these comparisons were expected to express differences, as they represent two distinct positions with a slightly different number of electrodes in contact. Indeed, all five comparisons were proven to be different, with a p-value $p< 0.01$ for all of them. When two different positions were compared, the stimulating pair used in either scenario was not relevant, as C_6, C_7, C_8, C_9, and C_{12} demonstrated, Not only the difference between floating completely in saline and being in full contact showed significance, but also the difference between two contact with not all the electrodes on full contact did. These results are promising for the implementation of this technology as complementary mapping feature.

Similarly, in Figure 10.5, the results from similar or identical comparisons are represented. It was previously hypothesized that, due to their recording settings, the difference between these comparisons were not statistically significant, which was correct for C_1, C_2, C_4, and C_{11}. However, C_5 and C_{10}, which compared similar measurements, yielded statistical significance. Both comparisons analyzed alike positions within few minutes with the stimulating pair differing among the three scenarios. C_2 also compared invariant contact settings, but the stimulating pair from M_{ref}, i.e. electrodes 1 and 2, was also used in one of the compared measurements M_{11}.

In Table 10.3, four exemplary comparisons of median values from each distribution of P_1 and P_2 at C_5, C_6, C_8, and C_{10} can be found. When comparing median measurements at direct catheter-tissue contact, LI on tissue showed always higher results in the surroundings of the injecting pair than floating on saline. Moreover, comparing between the full contact and the close proximity settings, electrodes in the vicinity of the injecting pair also measured higher LI.

Table 10.2: Description and statistical results from all 12 comparisons $C_{1\text{-}12}$. Measurement numbers used as M_{ref}, M_{x1}, and M_{x2} are indicated, as well as the p-value obtained from the statistical analysis (N.S.: no statistical significance).

	Label	Contact Settings	Measurements			Result (p-value)
			M_{ref}	M_{x1}	M_{x2}	
C_1	Identical	Full contact	M_2	M_{11}	M_{12}	N.S.
C_2	Similar	Full contact	M_2	M_{11}	M_{13}	N.S.
C_3	Different	Full contact vs. Saline	M_2	M_{11}	M_9	$p < 0.01$
C_4	Identical	Full contact	M_5	M_{13}	M_{14}	N.S.
C_5	Similar	Full contact	M_3	M_{11}	M_{13}	$p < 0.01$
C_6	Different	Full contact vs. Close proximity	M_3	M_{11}	M_8	$p < 0.01$
C_7	Different	Full contact vs. Close proximity	M_4	M_{11}	M_7	$p < 0.01$
C_8	Different	Full contact vs. Saline	M_1	M_{10}	M_3	$p < 0.01$
C_9	Different	Full contact vs. Saline	M_2	M_3	M_{11}	$p < 0.01$
C_{10}	Similar	Saline	M_1	M_3	M_4	$p < 0.01$
C_{11}	Similar	Saline	M_1	M_2	M_{15}	N.S.
C_{12}	Different	Full contact vs. Saline	M_1	M_{14}	M_3	$p < 0.01$

Table 10.3: Median values over time from either of the four electrodes distributions (E_{2-}, E_{1-}, E_{1+}, and E_{2+}) in C_5, C_6, C_8, and C_{10}. Each electrode of interest was compared between the compared measurements M_{x1} and M_{x2} using statistical test, whose p-value is shown (N.S.: no statistical significance).

	Median LI over time P_1 (Ω)				**Median LI over time P_2 (Ω)**				**Result (p-value)**
	E_{2-}	**E_{1-}**	**E_{1+}**	**E_{2+}**	**E_{2-}**	**E_{1-}**	**E_{1+}**	**E_{2+}**	
C_5	0.92	0.89	0.23	0.65	-0.15	-0.65	7.15	-0.11	$p < 0.01$
C_6	0.84	0.74	-0.05	0.41	0.92	0.89	0.23	0.65	$p < 0.01$, N.S., N.S., $p < 0.05$
C_8	0.35	-0.88	-0.01	0	0.51	-0.71	0.01	0.44	$p < 0.01$, N.S., N.S., $p < 0.05$
C_{10}	0.35	-0.88	-0.01	0	0.14	-2.32	8.31	-0.21	N.S., $p < 0.01$, $p < 0.01$, N.S.

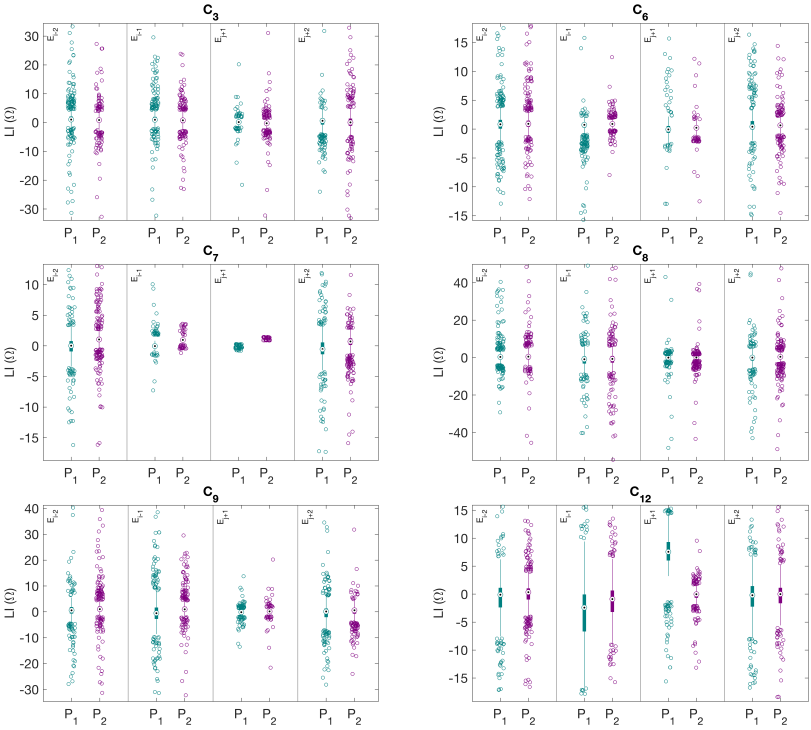

Figure 10.4: LI box-plots of various contact comparisons (P_1 and P_2) at each electrode of interest (E_{2-}, E_{1-}, E_{1+}, and E_{2+}) for different comparisons. From left to right and top to bottom: C_3, C_6, C_7, C_8, C_9, and C_{12}. All of them showed statistical significance. Results are zoomed in to show the major concentration of datapoints.

10.3.1 Limitation of this Work and Future Perspectives

The analysis of this data aims to shed some light on LI ability to detect catheter-tissue contact and set the potential to discern which type of tissue, healthy or scar, is underneath the electrodes in contact.

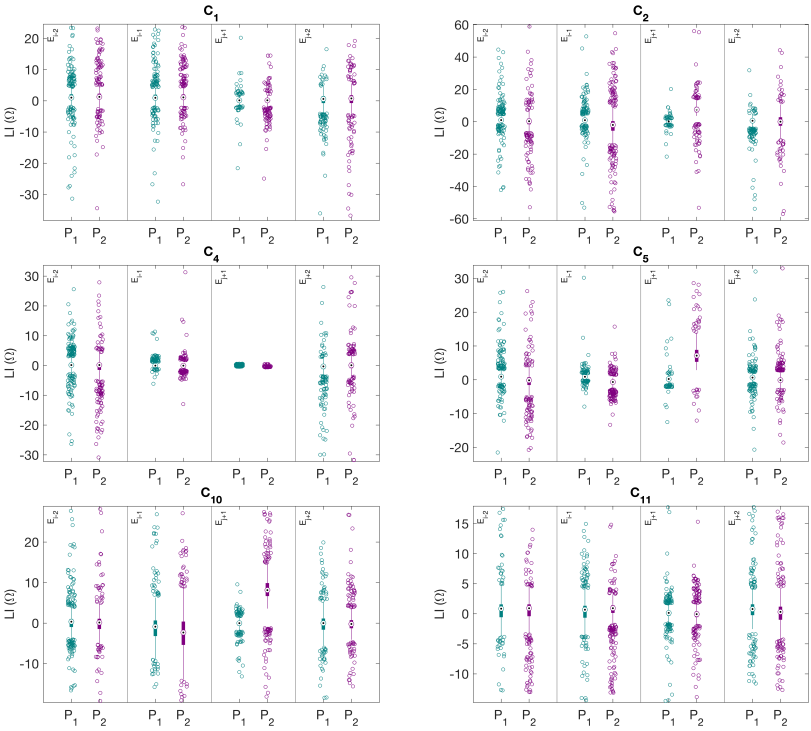

Figure 10.5: LI box-plots of various contact comparisons (P_1 and P_2) at each electrode of interest (E_{2-}, E_{1-}, E_{1+}, and E_{2+}) for similar and identical comparisons. From left to right and top to bottom: C_1, C_2, C_4, C_5, C_{10}, and C_{11}. Only C_4 and C_5 showed statistical significance. Results are zoomed in to show the major concentration of datapoints.

Following the *in silico* work presented in Chapter 8, the current analysis only explored the circular catheter arrangement. The stimulation patterns available in a basket catheter exceed those of a circular catheter, enabling the definition of horizontal, vertical, and diagonal bipoles among the various splines. Three-dimensional high-density mapping catheter, such as the IntellaMap Orion™ (Boston Scientific, Marlborough, MA, USA), or the Sphere-9™ (Medtronic, Dublin, Ireland), could offer a more solid cover by electrodes of the tissue surface, allowing for multiple measures acquired sequentially. Nevertheless, these catheters do not offer a flat surface of contact and it may be difficult to assure a full catheter-tissue contact ground truth during the *in vitro* measurements.

Although the frequency used lies in the spectrum range with a good differentiation between blood and myocardium, adipose, or connective tissue, the use of a broader spectrum that gets into the range of MHz would help giving some further insights about cardiac substrate. Within the range of MHz, the phenomenon of β-dispersion, and thus, changes in conductivity and permittivity, fades slightly, yielding to significantly higher conductivities [42]. However, achieving this frequency range in the practice using electroanatomical systems and their related signal stations is not so straightforward due to their waveform limitations.

Moreover, in this work, 10 out of 12 comparison cases yielded the expected results. Choosing the reference scenario to have the same stimulating pair as one of the compared scenarios may be of importance to not introduce differences in the measurements. However, it will make it more difficult to integrate LI measurements with sequential recordings. Introducing the possibility of recording alternatively from different stimulating pairs sequentially would clearly improve the resolution. The main drawback of impedance measurements as mapping systems have always been their reduced resolution, which may be improved with a smaller catheter radius as the *in silico* studies of Chapter 8 suggested.

As a follow-up of this work, the use of two phantoms of different conductivities, such as myocardial and adipose tissue, could present further challenges to the tissue detection by means of impedance. Hovering the catheter with half of the electrodes in contact with either tissue would extend the understanding of LI behavior and resolution. With the previously presented *in silico* tool, these *in vitro* measurements could be simulated to help confirming the findings of this study. However, *in vitro* experimentations include external factors that are not present in the "cleaned" *in silico* setup and thus, in addition, further experimentation, particularly *ex vivo* and *in vivo* measurements, should be carried out to test the future feasibility of impedance measurements in the clinics.

Overall, these findings together with the *in silico* results presented in Chapter 7, remain being promising for the implementation of this technology as complementary mapping feature.

PART VI

CONCLUSION AND OUTLOOK

Chapter 11

Conclusion and Outlook

This dissertation, "Impedance Characterization for Scar and Fibrosis Detection", served as a robust preliminary study exploring the additional potential of local impedance (LI)-based mapping. By combining *in silico* and *in vitro* experiments, significant progress towards the clinical implementation of this technology onto a multielectrode impedance mapping system has been made. This initial work in the field shed light on the advantages and possibilities of using LI as a supporting method to the already well established voltage maps and electrograms (EGMs) use.

While LI is often available in ablation catheters mainly to monitor lesion formation, the move towards multielectrode catheters could contribute to atrial substrate characterization. Thanks to its independence of depolarization fronts, LI could contribute to detection of certain fibrotic tissue structures.

This mapping modality should undergo further investigation in both modalities. For *in silico*, the use of several different catheters that provide diversity in geometric arrangement, injection and measurement current patterns, as well as the jump to a three-dimensional configuration, should be explored in the future. For this purpose, the computational method used in this work was not entirely suitable, but its improvement exceeded the scope of this work. In parallel with the *in silico* experiments, *in vitro* testing should explore more complex contact situations that yield to more realistic situations, especially in order to extend the studies to an *ex vivo* and *in vivo* setting.

Although limited, special attention needs the *in vitro* experiments. The data collection carried out, did not only serve to verify the feasibility of the simulated results, but also revealed artifacts, such as the need of a stable reference measurement, that could affect the clinical application of LI measurements. All in all, this work has contributed in progressing towards the overall objective of characterizing atrial substrate by means of LI.

List of Figures

List of Tables

References

[1] A. D. Elliott, M. E. Middeldorp, I. C. Van Gelder, C. M. Albert, and P. Sanders, "Epidemiology and modifiable risk factors for atrial fibrillation," *Nature Reviews Cardiology*, 2023. doi:10.1038/s41569-022-00820-8

[2] M. Gunawardene, P. Münkler, C. Eickholt, et al., "A novel assessment of local impedance during catheter ablation: initial experience in humans comparing local and generator measurements," *EP Europace*, vol. 21, pp. i34–i42, 2019. doi:10.1093/europace/euy273

[3] L. Segreti, A. De Simone, V. Schillaci, et al., "A novel local impedance algorithm to guide effective pulmonary vein isolation in atrial fibrillation patients: Preliminary experience across different ablation sites from the charisma pilot study," *Journal of Cardiovascular Electrophysiology*, vol. 31, pp. 2319–2327, 2020. doi:https://doi.org/10.1111/jce.14647

[4] H. Fritsch and W. Kühnel, *Color atlas of human anatomy, vol. 2: Internal organs*, vol. 2. Thieme, 2014.

[5] R. H. Anderson, R. Razavi, and A. M. Taylor, "Cardiac anatomy revisited," *Journal of Anatomy*, vol. 205, pp. 159–177, 2004. doi:https://doi.org/10.1111/j.0021-8782.2004.00330.x

[6] D. B. Tran, C. Weber, and R. A. Lopez, *Anatomy, thorax, heart muscles*. StatPearls Publishing [Internet], 2019.

[7] S. Y. Ho, "Anatomy and myoarchitecture of the left ventricular wall in normal and in disease," *European Journal of Echocardiography*, vol. 10, pp. iii3–iii7, 2009.

[8] S. Ho and P. Nihoyannopoulos, "Anatomy, echocardiography, and normal right ventricular dimensions," *Heart*, vol. 92, pp. i2–i13, 2006.

[9] S. Y. Ho, J. A. Cabrera, and D. Sanchez-Quintana, "Left atrial anatomy revisited," *Circulation: Arrhythmia and Electrophysiology*, vol. 5, pp. 220–228, 2012. doi:10.1161/CIRCEP.111.962720

[10] J. Ortale, E. Gabriel, C. Iost, and C. Marquez, "The anatomy of the coronary sinus and its tributaries," *Surgical and Radiologic Anatomy*, vol. 23, pp. 15–21, 2001.

[11] N. M. Al-Saady, O. A. Obel, and A. J. Camm, "Left atrial appendage: structure, function, and role in thromboembolism," *Heart*, vol. 82, pp. 547–554, 1999. doi:10.1136/hrt.82.5.547

[12] P. Martínez Díaz, C. Goetz, A. Dasi, et al., "Atrial Models with Personalized Effective Refractory Period," 2024. doi:10.5281/zenodo.10726677

[13] J. Betts, *Anatomy and physiology*, Open Textbook Library. OpenStax College, Rice University, 2013. https://books.google.de/books?id=dvVgngEACAAJ

[14] E. CARMELIET, "Action potential duration, rate of stimulation, and intracellular sodium," *Journal of Cardiovascular Electrophysiology*, vol. 17, pp. S2–S7, 2006. doi:https://doi.org/10.1111/j.1540-8167.2006.00378.x

[15] W. T. Clusin, "Mechanisms of calcium transient and action potential alternans in cardiac cells and tissues," *American Journal of Physiology-Heart and Circulatory Physiology*, vol. 294, pp. H1–H10, 2008.

[16] W. T. Clusin, "Mechanisms of calcium transient and action potential alternans in cardiac cells and tissues," *American Journal of Physiology-Heart and Circulatory Physiology*, vol. 294, pp. H1–H10, 2008, pMID: 17951365. doi:10.1152/ajpheart.00802.2007

[17] J. M. Nerbonne and R. S. Kass, "Molecular physiology of cardiac repolarization," *Physiological Reviews*, vol. 85, pp. 1205–1253, 2005, pMID: 16183911. doi:10.1152/physrev.00002.2005

[18] A. O. Grant, "Cardiac ion channels," *Circulation: Arrhythmia and Electrophysiology*, vol. 2, pp. 185–194, 2009.

[19] A. H. Kashou, H. Basit, and L. Chhabra, *Physiology, sinoatrial node*. StatPearls Publishing, Treasure Island (FL), 2022. http://europepmc.org/books/NBK459238

[20] P. J. Podrid, "Reentry and the development of cardiac arrhythmias," *UptoDate*, 2008.

[21] J. H. Kingma, N. M. van Hemel, and K. Lie, *Atrial fibrillation, a treatable disease?*, vol. 139. Springer Science & Business Media, 2012.

[22] N. S. Sawhney and G. K. Feld, "Diagnosis and management of typical atrial flutter," *Medical Clinics of North America*, vol. 92, pp. 65–85, 2008.

[23] M. Chard and R. Tabrizchi, "The role of pulmonary veins in atrial fibrillation: a complex yet simple story," *Pharmacology & Therapeutics*, vol. 124, pp. 207–218, 2009.

[24] "Chapter 15 - atrial flutter and atrial fibrillation," in *Chou's Electrocardiography in Clinical Practice (Sixth Edition)*, B. Surawicz and T. K. Knilans, Eds. Philadelphia: W.B. Saunders, 2008, pp. 361–383. doi:https://doi.org/10.1016/B978-141603774-3.10015-2

[25] P. Ganesan and S. M. Narayan, "Re-evaluating the multiple wavelet hypothesis for atrial fibrillation," *Heart Rhythm*, vol. 17, pp. 2219–2220, 2020.

[26] C. T. January, L. S. Wann, H. Calkins, et al., "2019 AHA/ACC/HRS focused update of the 2014 AHA/ACC/HRS guideline for the management of patients with atrial fibrillation: a report of the American College of Cardiology/American Heart Association Task Force on Clinical Practice Guidelines and the Heart Rhythm Society in collaboration with the Society of Thoracic Surgeons," *Circulation*, vol. 140, pp. e125–e151, 2019.

[27] H. Moghaddasi, R. C. Hendriks, A.-J. van der Veen, N. M. de Groot, and B. Hunyadi, "Novel rank-based features of atrial potentials for the classification between paroxysmal and persistent atrial fibrillation," in *2022 Computing in Cardiology (CinC)*, vol. 498, 2022, pp. 1–4. doi:10.22489/CinC.2022.326

[28] J. Pellman and F. Sheikh, "Atrial fibrillation: mechanisms, therapeutics, and future directions," *Comprehensive Physiology*, vol. 5, p. 649, 2015.

[29] T. P. Nguyen, Z. Qu, and J. N. Weiss, "Cardiac fibrosis and arrhythmogenesis: the road to repair is paved with perils," *Journal of Molecular and Cellular Cardiology*, vol. 70, pp. 83–91, 2014.

[30] J. Sánchez and A. Loewe, "A review of healthy and fibrotic myocardium microstructure modeling and corresponding intracardiac electrograms," *Frontiers in Physiology*, vol. 13, p. 916, 2022.

[31] B. J. Hansen, J. Zhao, and V. V. Fedorov, "Fibrosis and atrial fibrillation: computerized and optical mapping: a view into the human atria at submillimeter resolution," *JACC: Clinical Electrophysiology*, vol. 3, pp. 531–546, 2017.

[32] J. A. Reiffel, "Drug choices in the treatment of atrial fibrillation," *The American Journal of Cardiology*, vol. 85, pp. 12–19, 2000.

[33] M. Haissaguerre, P. Jaïs, D. C. Shah, et al., "Spontaneous initiation of atrial fibrillation by ectopic beats originating in the pulmonary veins," *New England Journal of Medicine*, vol. 339, pp. 659–666, 1998.

[34] K.-H. Kuck, J. Brugada, M. Schlueter, et al., "The fire and ice trial: what we know, what we can still learn, and what we need to address in the future," *Journal of the American Heart Association*, vol. 7, p. e010777, 2018.

[35] A. Luik, A. Radzewitz, M. Kieser, et al., "Cryoballoon versus open irrigated radiofrequency ablation in patients with paroxysmal atrial fibrillation: the prospective, randomized, controlled, noninferiority freezeaf study," *Circulation*, vol. 132, pp. 1311–1319, 2015.

[36] M. H. Ruwald, A. Johannessen, M. L. Hansen, M. Haugdal, R. Worck, and J. Hansen, "Pulsed field ablation in real-world atrial fibrillation patients: clinical recurrence, operator learning curve and re-do procedural findings," *Journal of Interventional Cardiac Electrophysiology*, pp. 1–12, 2023.

[37] S. Ruipérez-Campillo, M. Crespo, Á. Tormos, et al., "Evaluation and assessment of clique arrangements for the estimation of omnipolar electrograms in high density electrode arrays: an experimental animal model study," *Physical and Engineering Sciences in Medicine*, pp. 1–12, 2023.

[38] N. M. De Groot, D. Shah, P. M. Boyle, et al., "Critical appraisal of technologies to assess electrical qctivity during atrial fibrillation: a position paper from the European Heart Rhythm Association and European Society of Cardiology working group on E-Cardiology in collaboration with the Heart Rhythm Society, Asia Pacific Heart Rhythm Society, Latin American Heart Rhythm Society and Computing in Cardiology," *EP Europace*, vol. 24, pp. 313–330, 2022.

[39] F. M. Kusumoto, *Understanding intracardiac egms and ecgs*. John Wiley & Sons, 2011.

[40] M. S. Sulkin, J. I. Laughner, S. Hilbert, et al., "Novel measure of local impedance predicts catheter–tissue contact and lesion formation," *Circulation: Arrhythmia and Electrophysiology*, vol. 11, p. e005831, 2018.

[41] E. Michel, D. Hernandez, and S. Y. Lee, "Electrical conductivity and permittivity maps of brain tissues derived from water content based on t1-weighted acquisition," *Magnetic Resonance in Medicine*, vol. 77, pp. 1094–1103, 2017.

[42] S. Grimnes and O. G. Martinsen, *Bioimpedance and bioelectricity basics*. London, San Diego: Academic Press, 2000.

[43] G. H. Markx and C. L. Davey, "The dielectric properties of biological cells at radiofrequencies: applications in biotechnology," *Enzyme and Microbial Technology*, vol. 25, pp. 161–171, 1999.

[44] O. Dössel, *Bildgebende verfahren in der medizin*. Springer, 2000.

[45] W. R. AMBERSON, "Blood substitutes," *Biological Reviews*, vol. 12, pp. 48–86, 1937.

[46] L. A. Unger, "Multimodal characterization of the atrial substrate - risks and rewards of electrogram and impedance mapping," PhD thesis, Karlsruher Institut für Technologie (KIT), 2022.

[47] K. S. Cole and R. H. Cole, "Dispersion and absorption in dielectrics i. alternating current characteristics," *The Journal of Chemical Physics*, vol. 9, pp. 341–351, 1941.

[48] S. Gabriel, R. W. Lau, and C. Gabriel, "The dielectric properties of biological tissues: II. measurements in the frequency range 10 Hz to 20 GHz," *Physics in Medicine and Biology*, vol. 41, pp. 2251–2269, 1996.

[49] IT'IS Foundation, "Tissue properties database v4.0," 2018. doi:10.13099/VIP21000-04-0

[50] C. Gabriel, *Compilation of the dielectric properties of body tissues at RF and microwave frequencies*. Texas, USA: Occupational and Environmental Health Directorate, Radiofrequency Radiation Division, Brooks Air Force Base, 1996, report N.AL/OE-TR-1996-0037. doi:10.21236/ada303903

[51] A. L. Hodgkin and A. F. Huxley, "A quantitative description of membrane current and its application to conduction and excitation in nerve," *The Journal of physiology*, vol. 117, p. 500, 1952.

[52] M. Courtemanche, R. J. Ramirez, and S. Nattel, "Ionic mechanisms underlying human atrial action potential properties: insights from a mathematical model," *American Journal of Physiology-Heart and Circulatory Physiology*, vol. 275, pp. H301–H321, 1998.

[53] A. Nygren, C. Fiset, L. Firek, et al., "Mathematical model of an adult human atrial cell: the role of k+ currents in repolarization," *Circulation Research*, vol. 82, pp. 63–81, 1998.

[54] T. O'Hara, L. Virág, A. Varró, and Y. Rudy, "Simulation of the undiseased human cardiac ventricular action potential: model formulation and experimental validation," *PLoS Computational Biology*, vol. 7, p. e1002061, 2011.

[55] K. H. ten Tusscher, D. Noble, P.-J. Noble, and A. V. Panfilov, "A model for human ventricular tissue," *American Journal of Physiology-Heart and Circulatory Physiology*, vol. 286, pp. H1573–H1589, 2004.

[56] J. Tomek, A. Bueno-Orovio, E. Passini, et al., "Development, calibration, and validation of a novel human ventricular myocyte model in health, disease, and drug block," *Elife*, vol. 8, p. e48890, 2019.

[57] M. Paci, J. Hyttinen, and S. Severi, "A novel model of the action potential of ventricular-like human induced pluripotent stem cell-derived cardiomyocytes," in *2012 Computing in Cardiology*. IEEE, 2012, pp. 289–292.

[58] L. Tung, "A bi-domain model for describing ischemic myocardial dc potentials." PhD thesis, Massachusetts Institute of Technology, 1978.

[59] M. Potse, B. Dube, J. Richer, A. Vinet, and R. M. Gulrajani, "A comparison of monodomain and bidomain reaction-diffusion models for action potential propagation in the human heart," *IEEE Transactions on Biomedical Engineering*, vol. 53, pp. 2425–2435, 2006. doi:10.1109/TBME.2006.880875

[60] Y. Coudière, Y. Bourgault, and M. Rioux, "Optimal monodomain approximations of the bidomain equations used in cardiac electrophysiology," *Mathematical Models and Methods in Applied Sciences*, vol. 24, pp. 1115–1140, 2014.

[61] M. Vauhkonen, D. Vadasz, P. Karjalainen, E. Somersalo, and J. Kaipio, "Tikhonov regularization and prior information in electrical impedance tomography," *IEEE Transactions on Medical Imaging*, vol. 17, pp. 285–293, 1998. doi:10.1109/42.700740

[62] T. Dai, "Image reconstruction in eit using advanced regularization frameworks," PhD thesis, Carleton University, 2008.

[63] L. A. Unger, C. M. Antón, M. Stritt, et al., "In silico study of local electrical impedance measurements in the atria - towards understanding and quantifying dependencies in human," *IEEE Transactions on Biomedical Engineering*, vol. 70, pp. 533–543, 2023. doi:10.1109/TBME.2022.3196545

[64] M. Kircher, "Towards an efficient gas exchange monitoring with electrical impedance tomography-optimization and validation of methods to investigate and understand pulmonary blood flow with indicator dilution," PhD thesis, Karlsruher Institut für Technologie (KIT), 2021.

[65] E. P. Gerstenfeld, D. J. Callans, S. Dixit, E. Zado, and F. E. Marchlinski, "Incidence and location of focal atrial fibrillation triggers in patients undergoing repeat pulmonary vein isolation: implications for ablation strategies," *Journal of Cardiovascular Electrophysiology*, vol. 14, pp. 685–690, 2003.

[66] R. Proietti, L. Lichelli, N. Lellouche, and T. Dhanjal, "The challenge of optimising ablation lesions in catheter ablation of ventricular tachycardia," *Journal of Arrhythmia*, vol. 37, pp. 140–147, 2021.

[67] R. Cappato, H. Calkins, S.-A. Chen, et al., "Updated worldwide survey on the methods, efficacy, and safety of catheter ablation for human atrial fibrillation," *Circulation: Arrhythmia and Electrophysiology*, vol. 3, pp. 32–38, 2010.

[68] A. Wokhlu, D. O. Hodge, K. H. Monahan, et al., "Long-term outcome of atrial fibrillation ablation: impact and predictors of very late recurrence," *Journal of Cardiovascular Electrophysiology*, vol. 21, pp. 1071–1078, 2010.

[69] L.-F. Hsu, P. Jaïs, P. Sanders, et al., "Catheter ablation for atrial fibrillation in congestive heart failure," *New England Journal of Medicine*, vol. 351, pp. 2373–2383, 2004.

[70] L. O'Neill, B. De Becker, M. A. De Smet, et al., "Catheter ablation of persistent af—where are we now?" *Reviews in Cardiovascular Medicine*, vol. 24, p. 339, 2023.

[71] E. Anter, "Limitations and pitfalls of substrate mapping for ventricular tachycardia," *Clinical Electrophysiology*, vol. 7, pp. 542–560, 2021.

[72] A. Frontera, L. R. Limite, S. Pagani, et al., "Characterization of cardiac electrogram signals in atrial arrhythmias." *Minerva Cardiology and Angiology*, vol. 69, pp. 70–80, 2021.

[73] I. Sim, M. Bishop, M. O'Neill, and S. E. Williams, "Left atrial voltage mapping: defining and targeting the atrial fibrillation substrate," *Journal of Interventional Cardiac Electrophysiology*, vol. 56, pp. 213–227, 2019.

[74] P. S. Cunha, S. Laranjo, J. Heijman, and M. M. Oliveira, "The atrium in atrial fibrillation–a clinical review on how to manage atrial fibrotic substrates," *Frontiers in Cardiovascular Medicine*, vol. 9, p. 879984, 2022.

[75] D. Nairn, H. Lehrmann, B. Müller-Edenborn, et al., "Comparison of unipolar and bipolar voltage mapping for localization of left atrial arrhythmogenic substrate in patients with atrial fibrillation," *Frontiers in Physiology*, vol. 11, 2020.

[76] U. Schotten, "Mapping of atrial fibrillation-basic research and clinical applications," *Swiss Medical Weekly*, vol. 139, pp. 496–504, 2009.

[77] C. Reithmann, T. Remp, E. Hoffmann, T. Matis, R. Wakili, and G. Steinbeck, "Different patterns of the fall of impedance as the result of heating during ostial pulmonary vein ablation: Implications for power titration," *Pacing and Clinical Electrophysiology*, vol. 28, pp. 1282–1291, 2005. doi:10.1111/j.1540-8159.2005.00269.x

[78] G. S. Chu, P. Calvert, P. Futyma, W. Y. Ding, R. Snowdon, and D. Gupta, "Local impedance for the optimization of radiofrequency lesion delivery: A review of bench and clinical data," *Journal of Cardiovascular Electrophysiology*, vol. 33, pp. 389–400, 2022. doi:https://doi.org/10.1111/jce.15335

[79] P. C. Qian, D. M. Nguyen, M. A. Barry, et al., "Optimizing impedance change measurement during radiofrequency ablation enables more accurate characterization of lesion formation," *JACC: Clinical Electrophysiology*, vol. 7, pp. 471–481, 2021. doi:10.1016/j.jacep.2020.09.011

[80] R. van Es, J. Hauck, V. J. H. M. van Driel, et al., "Novel method for electrode-tissue contact measurement with multi-electrode catheters." *EP Europace*, vol. 20, pp. 149–156, 2017. doi:10.1093/europace/euw388

[81] C. Piorkowski, H. Sih, P. Sommer, et al., "First in human validation of impedance-based catheter tip-to-tissue contact assessment in the left atrium," *Journal of Cardiovascular Electrophysiology*, vol. 20, pp. 1366–1373, 2009.

[82] M. Das, J. J. Loveday, G. J. Wynn, et al., "Ablation index, a novel marker of ablation lesion quality: prediction of pulmonary vein reconnection at repeat electrophysiology study and regional differences in target values," *Europace*, vol. 19, pp. 775–783, 2017.

[83] H. Mizuno, P. Vergara, G. Maccabelli, et al., "Contact force monitoring for cardiac mapping in patients with ventricular tachycardia," *Journal of Cardiovascular Electrophysiology*, vol. 24, pp. 519–524, 2013.

[84] D. Kawano, H. Mori, K. Tsutsui, et al., "The target ablation index values for electrical isolation of the superior vena cava," *Journal of Interventional Cardiac Electrophysiology*, vol. 64, pp. 687–694, 2022.

[85] F. Bourier, "Local impedance, current, power — what should be considered in RF ablation?" *Journal of Cardiovascular Electrophysiology*, vol. 34, pp. 1681–1682, 2023.

[86] Z. F. Issa, "Radiofrequency lesion formation prediction with contact force versus local impedance," *Current Opinion in Cardiology*, vol. 39, pp. 6–14, 2024.

[87] K. Garrott, J. Laughner, S. Gutbrod, et al., "Combined local impedance and contact force for radiofrequency ablation assessment," *Heart Rhythm*, vol. 17, pp. 1371–1380, 2020. doi:10.1016/j.hrthm.2020.03.016

[88] G. S. Chu and D. Gupta, "Local impedance to guide focal radiofrequency ablation: There is life in the old dog yet," *Journal of Cardiovascular Electrophysiology*, vol. 32, pp. 1549–1552, 2021. doi:https://doi.org/10.1111/jce.15039

[89] M. Das, A. Luik, E. Shepherd, et al., "Local catheter impedance drop during pulmonary vein isolation predicts acute conduction block in patients with paroxysmal atrial fibrillation: initial results of the LOCALIZE clinical trial," *EP Europace*, vol. 23, pp. 1042–1051, 2021. doi:10.1093/europace/euab004

[90] C. A. Martin, R. Martin, P. R. Gajendragadkar, et al., "First clinical use of novel ablation catheter incorporating local impedance data," *Journal of Cardiovascular Electrophysiology*, vol. 29, pp. 1197–1206, 2018. doi:10.1111/jce.13654

[91] P. Kauppinen, J. Hyttinen, and M. J., "Sensitivity distribution visualizations of impedance tomography measurement strategies," *International Journal of Bioelectromagnetism*, vol. 8, pp. 63–71, 2006.

[92] P. C. Qian, D. M. Nguyen, M. A. Barry, et al., "Optimizing impedance change measurement during radiofrequency ablation enables more accurate characterization of lesion formation," *Clinical Electrophysiology*, vol. 7, pp. 471–481, 2021.

[93] M. H. Groen, V. J. van Driel, K. Neven, et al., "Multielectrode contact measurement can improve long-term outcome of pulmonary vein isolation using circular single-pulse electroporation ablation," *Circulation: Arrhythmia and Electrophysiology*, vol. 15, p. e010835, 2022.

[94] T. Ikenouchi, M. Takigawa, M. Goya, et al., "Requirement of larger local impedance reduction for successful lesion formation at carinal area during pulmonary vein isolation," *Journal of Interventional Cardiac Electrophysiology*, vol. 65, pp. 509–518, 2022.

[95] S. Miyazaki, K. Hasegawa, M. Mukai, et al., "Superior vena cava isolation using a novel ablation catheter incorporating local impedance monitoring," *Journal of Interventional Cardiac Electrophysiology*, pp. 1–10, 2022.

[96] E. Pesch, L. Riesinger, N. Vonderlin, et al., "Role of catheter location on local impedance measurements and clinical outcome with the new direct sense technology in cardiac ablation procedures," *IJC Heart & Vasculature*, vol. 42, p. 101109, 2022.

[97] F. Solimene, V. Schillaci, G. Stabile, et al., "Prospective evaluation of local impedance drop to guide left atrial posterior wall ablation with high power," *Journal of Interventional Cardiac Electrophysiology*, vol. 65, pp. 675–684, 2022.

[98] V. Ducceschi, G. Zingarini, G. Nigro, et al., "Optimized radiofrequency lesions through local impedance guidance for effective cti ablation in right atrial flutter," *Pacing and Clinical Electrophysiology*, vol. 45, pp. 612–618, 2022.

[99] F. Bahlke, A. Wachter, N. Erhard, et al., "The influence of electrode-tissue-coverage on rf lesion formation and local impedance: Insights from an ex vivo model," *Pacing and Clinical Electrophysiology*, vol. 46, pp. 1170–1181, 2023.

[100] M. Takigawa, T. Yamamoto, M. Amemiya, et al., "Impact of baseline pool impedance on lesion metrics and steam pops in catheter ablation," *Journal of Cardiovascular Electrophysiology*, 2023.

[101] M. Amemiya, M. Takigawa, M. Goya, et al., "Comparison of two catheters measuring local impedance: local impedance variation vs lesion characteristics and steam pops," *Journal of Interventional Cardiac Electrophysiology*, vol. 65, pp. 419–428, 2022.

[102] G. Matsuura, H. Fukaya, E. Ogawa, et al., "Catheter contact angle influences local impedance drop during radiofrequency catheter ablation: Insight from a porcine experimental study with 2 different li-sensing catheters," *Journal of Cardiovascular Electrophysiology*, vol. 33, pp. 380–388, 2022.

[103] D. Kawano, H. Mori, R. Kato, et al., "The optimal ablation setting for a local impedance guided catheter in an in vitro experimental model," *Journal of Cardiovascular Electrophysiology*, vol. 32, pp. 2069–2076, 2021.

[104] F.-A. Alken, K. Scherschel, A.-K. Kahle, M. Masjedi, and C. Meyer, "Combined contact force and local impedance dynamics during repeat atrial fibrillation catheter ablation," *Frontiers in Physiology*, p. 2144, 2022.

[105] I. García-Bolao, P. Ramos, A. Luik, et al., "Local impedance drop predicts durable conduction block in patients with paroxysmal atrial fibrillation," *Clinical Electrophysiology*, vol. 8, pp. 595–604, 2022.

[106] F. Solimene, F. Maddaluno, M. Malacrida, and G. Stabile, "How to leverage local impedance to guide effective ablation strategy: a case series," *HeartRhythm Case Reports*, vol. 7, pp. 65–68, 2021.

[107] L. Segreti, A. De Simone, V. Schillaci, et al., "A novel local impedance algorithm to guide effective pulmonary vein isolation in atrial fibrillation patients: preliminary experience across different ablation sites from the charisma pilot study," *Journal of Cardiovascular Electrophysiology*, vol. 31, pp. 2319–2327, 2020.

[108] A. Lepillier, R. Maggio, V. De Sanctis, et al., "Insight into contact force local impedance technology for predicting effective pulmonary vein isolation," *Frontiers in Cardiovascular Medicine*, vol. 10, 2023.

[109] F. Solimene, M. Giannotti Santoro, A. De Simone, et al., "Pulmonary vein isolation in atrial fibrillation patients guided by a novel local impedance algorithm: 1-year outcome from the charisma study," *Journal of Cardiovascular Electrophysiology*, vol. 32, pp. 1540–1548, 2021.

[110] N. Szegedi, Z. Salló, P. Perge, et al., "The role of local impedance drop in the acute lesion efficacy during pulmonary vein isolation performed with a new contact force sensing catheter—a pilot study," *PLoS One*, vol. 16, p. e0257050, 2021.

[111] H. Fukaya, H. Mori, J. Oikawa, et al., "Optimal local impedance parameters for successful pulmonary vein isolation in patients with atrial fibrillation," *Journal of Cardiovascular Electrophysiology*, vol. 34, pp. 71–81, 2023.

[112] T. Sasaki, K. Nakamura, M. Inoue, et al., "Optimal local impedance drops for an effective radiofrequency ablation during cavo-tricuspid isthmus ablation," *Journal of Arrhythmia*, vol. 36, pp. 905–911, 2020.

[113] T. Sasaki, K. Nakamura, K. Minami, et al., "Local impedance measurements during contact force-guided cavotricuspid isthmus ablation for predicting an effective radiofrequency ablation," *Journal of Arrhythmia*, vol. 38, pp. 245–252, 2022.

[114] M. Masuda, T. Kanda, N. Kurata, et al., "Clinical utility of local impedance monitoring during pulmonary vein isolation," *Journal of Cardiovascular Electrophysiology*, vol. 31, pp. 2584–2591, 2020.

[115] S. R. Gutbrod, A. Shuros, V. Koya, et al., "Improved ablation efficiency in pvi guided by contact force and local impedance: Chronic canine model," *Frontiers in Physiology*, vol. 12, p. 2451, 2022.

[116] F. Solimene, V. De Sanctis, R. Maggio, et al., "When local impedance meets contact force: preliminary experience from the charisma registry," *Journal of Interventional Cardiac Electrophysiology*, vol. 63, pp. 749–758, 2022.

[117] D. Kawano, H. Mori, K. Tsutsui, et al., "Time dependency in the radiofrequency lesion formation for a local impedance guided catheter in an ex vivo experimental model," *Journal of Arrhythmia*, vol. 38, pp. 1080–1087, 2022.

[118] S. Yamashita, A. Mizukami, M. Ono, et al., "Higher power achieves greater local impedance drop, shorter ablation time, and more transmural lesion formation in comparison to lower power in local impedance guided radiofrequency ablation of atrial fibrillation," *Journal of Cardiovascular Electrophysiology*, vol. 34, pp. 1869–1877, 2023.

[119] K. Tsutsui, D. Kawano, H. Mori, et al., "Characteristics and optimal ablation settings of a novel, contact-force sensing and local impedance-enabled catheter in an ex vivo perfused swine ventricle model," *Journal of Cardiovascular Electrophysiology*, vol. 32, pp. 3187–3194, 2021.

[120] V. Schillaci, A. Arestia, F. Maddaluno, et al., "Combining contact force and local impedance to treat idiopathic premature ventricular contractions from the outflow tracts: impact of ablation strategy on outcomes," *Journal of Interventional Cardiac Electrophysiology*, pp. 1–10, 2023.

[121] K. Saraf, N. Black, C. J. Garratt, S. A. Muhyaldeen, and G. M. Morris, "Local impedance-guided ablation and ultra-high density mapping versus conventional or contact force-guided ablation with mapping for treatment of cavotricuspid isthmus dependent atrial flutter," *Indian Pacing and Electrophysiology Journal*, vol. 22, pp. 188–194, 2022.

[122] K. Osei, M. S. Sulkin, J. J. Hamann, et al., "Local impedance-guided radiofrequency ablation with standard and high power: Results of a preclinical investigation," *Journal of Cardiovascular Electrophysiology*, vol. 32, pp. 2060–2068, 2021.

[123] S. Iacopino, P. Filannino, P. Artale, F. Placentino, F. Pesce, and A. Petretta, "Antral lesion characterization of a new cryoballoon ablation system in terms of local impedance drop: the first reported case," *HeartRhythm Case Reports*, vol. 7, pp. 182–185, 2021.

[124] S. Iacopino, G. Fabiano, M. Malacrida, and A. Petretta, "Lesion effects in terms of local impedance variations after pulsed-field ablation during pulmonary vein isolation: a case report," *European Heart Journal-Case Reports*, vol. 7, p. ytad187, 2023.

[125] M. Takigawa, M. Goya, H. Iwakawa, et al., "Impact of a formula combining local impedance and conventional parameters on lesion size prediction," *Journal of Interventional Cardiac Electrophysiology*, vol. 63, pp. 389–398, 2022.

[126] K. Yasumoto, Y. Egami, S. Kawanami, et al., "The correlation between local impedance drop and catheter contact in clinical pulmonary vein isolation use," *Pacing and Clinical Electrophysiology*, vol. 45, pp. 984–992, 2022. doi:https://doi.org/10.1111/pace.14500

[127] A. Pedrote, E. Arana-Rueda, L. García-Riesco, et al., "Three-dimensional impedance mapping as an aid to circumferential pulmonary vein isolation in paroxysmal atrial fibrillation," *Revista Española de Cardiología (English Edition)*, vol. 62, pp. 315–319, 2009.

[128] L. A. Unger, L. Schicketanz, T. Oesterlein, et al., "Local electrical impedance mapping of the atria: Conclusions on substrate properties and confounding factors," *Frontiers in Physiology*, vol. 12, p. 788885, 2022.

[129] J. Aranyó, D. Martínez-Falguera, V. Bazan, et al., "Biophysical tissue characterization of ventricular tachycardia substrate with local impedance mapping to predict critical sites," *JACC: Clinical Electrophysiology*, 2023.

[130] G. Amorós-Figueras, E. Jorge, T. García-Sánchez, R. Bragós, J. Rosell-Ferrer, and J. Cinca, "Recognition of fibrotic infarct density by the pattern of local systolic-diastolic myocardial electrical impedance," *Frontiers in Physiology*, vol. 7, p. 389, 2016.

[131] G. Amorós-Figueras, S. Casabella-Ramon, D. Arzamendi, et al., "Electrophysiological and histological characterization of atrial scarring in a model of isolated atrial myocardial infarction," *Frontiers in Physiology*, vol. 13, p. 1104327, 2023.

[132] D. Nairn, M. Eichenlaub, H. Lehrmann, et al., "Spatial correlation of left atrial low voltage substrate in sinus rhythm versus atrial fibrillation: The rhythm specificity of atrial low voltage substrate," *Journal of Cardiovascular Electrophysiology*, vol. 34, pp. 1613–1621, 2023. doi:10.1111/jce.15984

[133] D. A. Bates, D. J. Paisey, D. A. Yue, M. P. Banks, P. Roberts, and D. W. Ullah, "Refinement of voltage-based atrial scar assessment using pacing thresholds and local impedance," *Europace*, vol. 25, 2023.

[134] A. Bates, J. Paisey, A. Yue, P. Banks, P. Roberts, and W. Ullah, "Determinants of left atrial local impedance: relationships with contact force, atrial fibrosis and rhythm," *Europace*, vol. 25, pp. euad122–730, 2023.

[135] S. Kawakami, E. Ogawa, H. Fukaya, G. Matsuura, S. Aiga, and H. Kumagai, "Estimation of mechanical properties by transcatheter monitoring using local impedance and contact force," *Journal of Medical Engineering & Technology*, vol. 47, pp. 141–146, 2023.

[136] C. M. Antón, J. Sánchez, A. Heinkele, et al., "Effect of contact force on local electrical impedance in atrial tissue - an in silico evaluation," in *2022 Computing in Cardiology (CinC)*, vol. 498, 2022, pp. 1–4. doi:10.22489/CinC.2022.337

[137] C. Martínez Antón, J. Sánchez, N. Caslli, et al., "In silico computation of electrograms and local electrical impedance to assess non-transmural fibrosis," in *2023 Computing in Cardiology (CinC)*, vol. 50, 2023, pp. 1–4. doi:10.22489/CinC.2023.283

[138] D. Nairn, M. Eichenlaub, B. Müller-Edenborn, et al., "Differences in atrial substrate localization using late gadolinium enhancement-magnetic resonance imaging, electrogram voltage, and conduction velocity: a cohort study using a consistent anatomical reference frame in patients with persistent atrial fibrillation." *Europace*, vol. 25, 2023. doi:10.1093/europace/euad278

[139] K. Nakamura, T. Sasaki, Y. Take, et al., "Incidence and characteristics of silent cerebral embolisms after radiofrequency-based atrial fibrillation ablation: A propensity score-matched analysis between different mapping catheters and indices for guiding ablation," *Journal of Cardiovascular Electrophysiology*, vol. 32, pp. 16–26, 2021.

[140] E. Lyan, R. Pantlik, V. Maslova, D. Frank, and T. Demming, "Local impedance drop guided versus lesion size index guided pulmonary vein isolation: acute success and reconnections," *Europace*, vol. 25, pp. euad122–683, 2023.

[141] B. G. Abeln, V. F. van Dijk, J. C. Balt, M. C. Wijffels, and L. V. Boersma, "Dielectric response as a novel marker for ablation lesion quality: Relation to conventional ablation parameters," *Journal of Arrhythmia*, vol. 39, pp. 776–783, 2023.

[142] G. S. Chu, P. Calvert, P. Futyma, W. Y. Ding, R. Snowdon, and D. Gupta, "Local impedance for the optimization of radiofrequency lesion delivery: A review of bench and clinical data," *Journal of Cardiovascular Electrophysiology*, 2021. doi:10.1111/jce.15335

[143] "INTELLANAV MIFI™ OPEN-IRRIGATED ABLATION CATHETER, Boston Scientific Corporation," *https://www.bostonscientific.com/content/dam/bostonscientific/Rhythm%20Management/general/EP-479201-AB_IntellaNav%20MiFi%20OI%20Spec%20Sheet%20FINAL.pdf*, 2018, accessed: 2022-01-05.

[144] "INTELLANAV STABLEPOINT™ ABLATION CATHETER, Boston Scientific Corporation," *https://www.bostonscientific.com/content/dam/bostonscientific/ep/Electrophysiology%20Portfolio/Rhythmia/intellanav-stablepoint/EP-815001-AB_STABLEPOINT_SPECSHEET.pdf*, 2020, accessed: 2022-01-05.

[145] C. Geuzaine and J.-F. Remacle, "Gmsh: A three-dimensional finite element mesh generator with built-in pre- and post-processing facilities," *International Journal for Numerical Methods in Engineering*, vol. 79, pp. 1309–1331, 2009. doi:10.1002/nme.2579

[146] P. G. Platonov, V. Ivanov, S. Y. Ho, and L. Mitrofanova, "Left atrial posterior wall thickness in patients with and without atrial fibrillation: data from 298 consecutive autopsies," *Journal of Cardiovascular Electrophysiology*, vol. 19, pp. 689–692, 2008. doi:10.1111/j.1540-8167.2008.01102.x

[147] D. R. Lide and T. J. Bruno, *CRC handbook of chemistry and physics*, vol. 99, J. R. Rumble, Ed. Boca Raton, FL: CRC Press, 2018.

[148] "The effect of temperature on conductivity measurement; CONDUCTIVITY METER 4520 application note: A002-001A," *http://www.jenway.com/adminimages/A02_001A_Effect_of_temperature_on_conductivity.pdf*, accessed: 2022-04-12.

[149] H. Cao, M. Speidel, J.-Z. Tsai, M. Van Lysel, V. Vorperian, and J. Webster, "FEM analysis of predicting electrode-myocardium contact from RF cardiac catheter ablation system impedance," *IEEE Transactions on Biomedical Engineering*, vol. 49, pp. 520–526, 2002. doi:10.1109/TBME.2002.1001965

[150] A. Adler and W. R. B. Lionheart, "Uses and abuses of EIDORS: an extensible software base for EIT," *Physiological Measurement*, vol. 27, pp. S25–42, 2006. doi:10.1088/0967-3334/27/5/S03

[151] K.-S. Cheng, D. Isaacson, J. Newell, and D. Gisser, "Electrode models for electric current computed tomography," *IEEE Transactions on Biomedical Engineering*, vol. 36, pp. 918–924, 1989. doi:10.1109/10.35300

[152] D. Bennett, "NaCl doping and the conductivity of agar phantoms," *Materials Science and Engineering: C*, vol. 31, pp. 494–498, 2011. doi:10.1016/j.msec.2010.08.018

[153] M. A. Kandadai, J. L. Raymond, and G. J. Shaw, "Comparison of electrical conductivities of various brain phantom gels: Developing a 'brain gel model'," *Materials Science and Engineering: C*, vol. 32, pp. 2664–2667, 2012.

[154] L. Segreti, A. De Simone, V. Schillaci, et al., "A novel local impedance algorithm to guide effective pulmonary vein isolation in atrial fibrillation patients: Preliminary experience across different ablation sites from the CHARISMA pilot study." *Journal of Cardiovascular Electrophysiology*, 2020. doi:10.1111/jce.14647

[155] M. Gunawardene, P. Münkler, C. Eickholt, et al., "A novel assessment of local impedance during catheter ablation: initial experience in humans comparing local and generator measurements." *EP Europace*, vol. 21, pp. i34–i42, 2019. doi:10.1093/europace/euy273

[156] C. Gianni, G. J. Gallinghouse, A. Al-Ahmad, et al., "Half-normal saline versus normal saline for irrigation of open-irrigated radiofrequency catheters in atrial fibrillation ablation," *Journal of Cardiovascular Electrophysiology*, vol. 32, pp. 973–981, 2021. doi:10.1111/jce.14885

[157] D. T. Nguyen, M. Olson, L. Zheng, W. Barham, J. D. Moss, and W. H. Sauer, "Effect of irrigant characteristics on lesion formation after radiofrequency energy delivery using

ablation catheters with actively cooled tips," *Journal of Cardiovascular Electrophysiology*, vol. 26, pp. 792–798, 2015. doi:10.1111/jce.12682

[158] D. T. Nguyen, K. Nguyen, L. Zheng, et al., "Effect of environmental impedance surrounding a radiofrequency ablation catheter electrode on lesion characteristics," *Journal of Cardiovascular Electrophysiology*, vol. 28, pp. 564–569, 2017. doi:10.1111/jce.13185

[159] D. T. Nguyen, E. P. Gerstenfeld, W. S. Tzou, et al., "Radiofrequency ablation using an open irrigated electrode cooled with half-normal saline," *JACC: Clinical Electrophysiology*, vol. 3, pp. 1103–1110, 2017. doi:10.1016/j.jacep.2017.03.006

[160] C. Martinez Anton, L. Unger, A. Haas, et al., "Impact of contact force on local impedance measurements in different atrial locations," *EP Europace*, vol. 24, p. euac053.259, 2022. doi:10.1093/europace/euac053.259

[161] C. M. Antón, J. Sánchez, A. Heinkele, et al., "Effect of contact force on local electrical impedance in atrial tissue - an in silico evaluation," in *2022 Computing in Cardiology (CinC)*, vol. 498, 2022, pp. 1–4. doi:10.22489/CinC.2022.337

[162] A. D. Heinkele, "Impact of contact force in local impedance characterization of cardiac tissue," Master's thesis, Institute of Biomedical Engineering, Karlsruhe Institute of Technology (KIT), 2022.

[163] S. R. Gutbrod, A. Shuros, V. Koya, et al., "Improved ablation efficiency in pvi guided by contact force and local impedance: Chronic canine model," *Frontiers in Physiology*, vol. 12, 2022. doi:10.3389/fphys.2021.808541

[164] S. Pollnow, J. Greiner, T. Oesterlein, E. M. Wülfers, A. Loewe, and O. Dössel, "Mini electrodes on ablation catheters: Valuable addition or redundant information? insights from a computational study," *Computational and Mathematical Methods in Medicine*, p. 13, 2017.

[165] C. Bellini, E. S. Di Martino, and S. Federico, "Mechanical behaviour of the human atria," *Ann Biomed Eng*, vol. 41, pp. 1478–1490, 2013. doi:10.1007/s10439-012-0699-9

[166] O. Villemain, M. Correia, D. Khraiche, et al., "Myocardial stiffness assessment using shear wave imaging in pediatric hypertrophic cardiomyopathy," *JACC: Cardiovascular Imaging*, vol. 11, pp. 779–781, 2018. doi:10.1016/j.jcmg.2017.08.018

[167] F. Alken, K. Scherschel, M. Masjedi, O. Grebe, and C. Meyer, "Novel simultaneous assessment of contact force and local impedance for radiofrequency catheter ablation guidance," *EP Europace*, vol. 23, 2021. doi:10.1093/europace/euab116.046

[168] D. M. Nguyen, T. Andersen, P. Qian, T. Barry, and A. McEwan, "Electrical impedance tomography for monitoring cardiac radiofrequency ablation: a scoping review of an emerging technology," *Medical Engineering & Physics*, vol. 84, pp. 36–50, 2020.

[169] D. M. Nguyen, P. Qian, T. Barry, and A. McEwan, "Cardiac radiofrequency ablation tracking using electrical impedance tomography," *Biomedical Physics & Engineering Express*, vol. 6, p. 015015, 2020.

[170] D. M. Nguyen, P. Qian, T. Barry, and A. McEwan, "Self-weighted NOSER-prior electrical impedance tomography using internal electrodes in cardiac radiofrequency ablation," *Physiological Measurement*, vol. 40, p. 065006, 2019.

[171] N. Caslli, "Electrogram and local impedance in non fully transmural fibrosis configurations," Bachelor's thesis, Institute of Biomedical Engineering, Karlsruhe Institute of Technology (KIT), 2023.

[172] C. Jellis, J. Martin, J. Narula, and T. H. Marwick, "Assessment of nonischemic myocardial fibrosis," *Journal of the American College of Cardiology*, vol. 56, pp. 89–97, 2010.

[173] J. Sánchez Arciniegas, B. Trénor, J. Saiz, O. Dössel, and A. Loewe, "Fibrotic remodeling during persistent atrial fibrillation: In silico investigation of the role of calcium for human atrial myofibroblast electrophysiology," *Cells*, vol. 10, p. 2852, 2021. doi:10.3390/cells10112852

[174] G. Plank, A. Loewe, A. Neic, et al., "The opencarp simulation environment for cardiac electrophysiology," *Computer Methods and Programs in Biomedicine*, vol. 208, p. 106223, 2021. doi:https://doi.org/10.1016/j.cmpb.2021.106223

[175] D. Nairn, D. Hunyar, J. Sánchez, O. Dössel, and A. Loewe, "Impact of electrode size on electrogram voltage in healthy and diseased tissue," in *2020 Computing in Cardiology*, 2020, pp. 1–4. doi:10.22489/CinC.2020.146

[176] S. Abdalla, "Low frequency dielectric properties of human blood," *IEEE Transactions on NanoBioscience*, vol. 10, 2011.

[177] "Orbiter™ PV, Boston Scientific Corporation," *https://www.watchman.com/content/dam/bostonscientific/ep/portfolio-group/catheters-diagnostic/Advanced%20Mapping%20Catheters/ORBITER%20PV/resources/ORBITER_PV_Mapping_catheter_EN_RM_30OCT18_EP-464702-AA_MAR2017.pdf*, 2017, accessed: 2023-01-03.

List of Publications and Supervised Theses

Journal Articles

- Laura Anna Unger, **Carmen Martínez Antón**, Michael Stritt, Reza Wakili, Annika Haas, Michael Kircher, Olaf Dössel, Armin Luik, *In Silico Study of Local Electrical Impedance Measurements in the Atria - Towards Understanding and Quantifying Dependencies in Human*, IEEE Transactions on Biomedical Engineering vol. 70, pp. 533–543, 2023.
- Laura Anna Unger, Leonie Schicketanz, Tobias Oesterlein, Michael Stritt, Annika Haas, **Carmen Martínez Antón**, Kerstin Schmidt, Olaf Dössel, Armin Luik, *Local Electrical Impedance Mapping of the Atria: Conclusions on Substrate Properties and Confounding Factors*, Frontiers in Physiology 2022, 12:788885.

Refereed Conference Articles

- **Carmen Martínez Antón**, Jorge Sánchez, Andreas Heinkele, Laura Anna Unger, Annika Haas, Kerstin Schmidt, Armin Luik, Axel Loewe, Olaf Dössel, *In Silico Evaluation of the Effect of Contact Force on Local Electrical Impedance in the Atria*, Computing in Cardiology 2022.
- **Carmen Martínez Antón**, Jorge Sánchez, Nansi Caslli, Lena Heinemann, Laura Anna Unger, Axel Loewe, Olaf Dössel, *In Silico Computation of Electrograms and Local Electrical Impedance to Assess Non-Transmural Fibrosis*, Computing in Cardiology 2023.

Refereed Conference Abstracts

- Laura Anna Unger, **Carmen Martínez Antón**, Tobias Oesterlein, Carina Jäger, Claus Schmitt, Olaf Doessel, Reza Wakili, Armin Luik, *Local Impedance Measurements with the INTELLANAV*

MIFI OI and the INTELLANAV STABLEPOINT Ablation Catheter are Linearly Related, Heart Rhythm 2021, 21-A-6595

- **Carmen Martínez Antón**, Laura Anna Unger, Olaf Dössel, *Analyzing the Effect of Catheter-Sheath Overlapping Status in Local Impedance Simulations*, 4th Atrial Signals 2021:10.
- **Carmen Martínez Antón**, Laura Anna Unger, Annika Haas, Kerstin Schmidt, Carina Jäger, Olaf Dössel, Armin Luik, *Impact of contact force on local impedance measurements in different atrial locations*, EP Europace 24, 10.1093/europace/euac053.259.

Conference Presentations

- Poster Contribution: *Analyzing the Effect of Catheter-Sheath Overlapping Status in Local Impedance Simulations*, Atrial Signals 2021, Karlsruhe (Germany)
- Poster Contribution: *Impact of contact force on local impedance measurements in different atrial locations*, European Heart Rhythm Association (EHRA) 2022, Copenhagen (Denmark)
- Scientific Talk: *In Silico Evaluation of the Effect of Contact Force on Local Electrical Impedance in the Atria*, Computing in Cardiology (CinC) Conference 2022, Tampere (Finland)
- Scientific Talk: *In Silico Computation of Electrograms and Local Electrical Impedance to Assess Non-Transmural Fibrosis*, Computing in Cardiology (CinC) Conference 2023, Atlanta (GA, USA)

Invited Talks

- **Carmen Martinez Anton** *In Silico Framework to Evaluate Local Impedance Measurements in Atrial Tissue*, 2023 Special Semester of Mathematical Methods in Medicine at the Radon Institute for Computational and Applied Mathematics (RICAM) of the Austrian Academy of Science, Linz (Austria), 1st of December 2023

Data Publication

- Dataset: Laura Anna Unger, **Carmen Martínez Antón**, Michael Stritt, Reza Wakili, Annika Haas, Michael Kircher, Olaf Dössel, and Armin Luik. *In Silico Local Electrical Impedance Measurements in the Atria*. Zenodo, February 29, 2024. https://doi.org/10.5281/zenodo.10726486.
- Dataset: **Carmen Martínez Antón**, Jorge Sánchez, Nansi Caslli, Lena Heinemann, Laura Anna Unger, Axel Loewe, and Olaf Dössel. *Impedance Reconstruction of Non-transmural Cardiac Fibrosis*. Zenodo, February 29, 2024. https://doi.org/10.5281/zenodo.10727271.
- Dataset: **Carmen Martínez Antón**, Jorge Sánchez, Andreas Heinkele, Laura Anna Unger, Annika Haas, Kerstin Schmidt, Armin Luik, Axel Loewe, and Olaf Dössel. *Simulated Local*

Electrical Impedance in Atrial Tissue with Varying Contact Force. Zenodo, February 29, 2024. https://doi.org/10.5281/zenodo.10726581.

Supervised Students

- Andreas Heinkele, *In Silico Evaluation of the Effect of Contact Force on Local Electrical Impedance in the Atria*, Master Thesis, Institute of Biomedical Engineering, Karlsruhe Institute of Technology (KIT), 2022
- Lena Heinemann, *Local Impedance Measurements in the Atria*, Student Research Project, Institute of Biomedical Engineering, Karlsruhe Institute of Technology (KIT), June 2021-December 2022
- Nansi Caslli, *Electrograms and Local Impedance in Non-Transmural Fibrosis Configurations*, Bachelor Thesis, Institute of Biomedical Engineering, Karlsruhe Institute of Technology (KIT), 2023
- Franziska Sophia Stolte, *Comparing Left Atrial Substrate Properties with Different Modalities: LGE-MRI and Local Impedance*, Bachelor Thesis, Institute of Biomedical Engineering, Karlsruhe Institute of Technology (KIT), 2023

Awards & Grants

- Semi-Finalist at the Young Investigator Award (YIA), *In Silico Evaluation of the Effect of Contact Force on Local Electrical Impedance in the Atria*, Computing in Cardiology (CinC) Conference 2022, Tampere (Finland)
- Semi-Finalist at the Young Investigator Award (YIA), *In Silico Computation of Electrograms and Local Electrical Impedance to Assess Non-Transmural Fibrosis*, Computing in Cardiology (CinC) Conference 2023, Atlanta (GA, USA)

Karlsruhe Transactions on Biomedical Engineering (ISSN 1864-5933)

Karlsruhe Institute of Technology / Institute of Biomedical Engineering (Ed.)

Band 2 Matthias Reumann
Computer assisted optimisation on non-pharmacological treatment of congestive heart failure and supraventricular arrhythmia.
ISBN 978-3-86644-122-4

Band 3 Antoun Khawaja
Automatic ECG analysis using principal component analysis and wavelet transformation.
ISBN 978-3-86644-132-3

Band 4 Dmytro Farina
Forward and inverse problems of electrocardiography: clinical investigations.
ISBN 978-3-86644-219-1

Band 5 Jörn Thiele
Optische und mechanische Messungen von elektrophysiologischen Vorgängen im Myokardgewebe.
ISBN 978-3-86644-240-5

Band 6 Raz Miri
Computer assisted optimization of cardiac resynchronization therapy.
ISBN 978-3-86644-360-0

Band 7 Frank Kreuder
2D-3D-Registrierung mit Parameterentkopplung für die Patientenlagerung in der Strahlentherapie.
ISBN 978-3-86644-376-1

Die Bände sind unter www.ksp.kit.edu als PDF frei verfügbar oder als Druckausgabe bestellbar.

Band 8 Daniel Unholtz
Optische Oberflächensignalmessung mit Mikrolinsen-Detektoren für die Kleintierbildgebung.
ISBN 978-3-86644-423-2

Band 9 Yuan Jiang
Solving the inverse problem of electrocardiography in a realistic environment.
ISBN 978-3-86644-486-7

Band 10 Sebastian Seitz
Magnetic Resonance Imaging on Patients with Implanted Cardiac Pacemakers.
ISBN 978-3-86644-610-6

Band 11 Tobias Voigt
Quantitative MR Imaging of the Electric Properties and Local SAR based on Improved RF Transmit Field Mapping.
ISBN 978-3-86644-598-7

Band 12 Frank Michael Weber
Personalizing Simulations of the Human Atria: Intracardiac Measurements, Tissue Conductivities, and Cellular Electrophysiology.
ISBN 978-3-86644-646-5

Band 13 David Urs Josef Keller
Multiscale Modeling of the Ventricles: from Cellular Electrophysio-logy to Body Surface Electrocardiograms.
ISBN 978-3-86644-714-1

Band 14 Oussama Jarrousse
Modified Mass-Spring System for Physically Based Deformation Modeling.
ISBN 978-3-86644-742-4

Band 15 Julia Bohnert
Effects of Time-Varying Magnetic Fields in the Frequency Range1 kHz to 100 kHz upon the Human Body: Numerical Studies and Stimulation Experiment.
ISBN 978-3-86644-782-0

Band 16 Hanno Homann
SAR Prediction and SAR Management for Parallel Transmit MRI.
ISBN 978-3-86644-800-1

Band 17 Christopher Schilling
Analysis of Atrial Electrograms.
ISBN 978-3-86644-894-0

Band 18 Tobias Baas
ECG Based Analysis of the Ventricular Repolarisation in the Human Heart.
ISBN 978-3-86644-882-7

Band 19 Martin Wolfgang Krüger
Personalized Multi-Scale Modeling of the Atria: Heterogeneities, Fiber Architecture, Hemodialysis and Ablation Therapy.
ISBN 978-3-86644-948-0

Band 20 Mathias Wilhelms
Multiscale Modeling of Cardiac Electrophysiology: Adaptation to Atrial and Ventricular Rhythm Disorders and Pharmacological Treatment.
ISBN 978-3-7315-0045-2

Band 21 Matthias Keller
Formation of Intracardiac Electrograms under Physiological and Pathological Conditions.
ISBN 978-3-7315-0228-9

Band 22 Walther H. W. Schulze
ECG Imaging of Ventricular Activity in Clinical Applications.
ISBN 978-3-7315-0374-3

Band 23 Axel Loewe
Modeling Human Atrial Patho-Electrophysiology from Ion Channels to ECG. Substrates, Pharmacology, Vulnerability, and P-Waves.
ISBN 978-3-7315-0528-0

Band 24 Stefan Pollnow
Characterizing Cardiac Electrophysiology during Radiofrequency Ablation: An Integrative *Ex vivo*, *In silico*, and *In vivo* Approach.
ISBN 978-3-7315-0886-1

Band 25 Jorge Patricio Sánchez Arciniegas
A Multiscale In Silico Study to Characterize the Atrial Electrical Activity of Patients With Atrial Fibrillation: A Translational Study to Guide Ablation Therapy.
ISBN 978-3-7315-1170-0

Band 26 Nicht erschienen

Band 27 Claudia Nagel
Multiscale Cohort Modeling of Atrial Electrophysiology: Risk Stratification for Atrial Fibrillation through Machine Learning on Electrocardiograms.
ISBN 978-3-7315-1281-3

Band 28 María del Carmen Martínez Antón
Local Impedance Characterization for Scar and Fibrosis Detection: Towards a New Substrate Assessment for Atrial Mapping.
ISBN 978-3-7315-1368-1

INSTITUTE OF BIOMEDICAL ENGINEERING
KARLSRUHE INSTITUTE OF TECHNOLOGY (KIT)

Regions of scar and fibrotic tissue have been identified as a potential driving region of arrhythmic activity during Atrial Fibrillation (AF), so the ablation of these areas represents a standard treatment. High density mapping techniques can provide important information about low voltage and slow conduction zones, both characteristics of arrhythmogenic areas. Local Impedance (LI) has gained attention as another modality for atrial substrate assessment as it does not rely on the dynamically changing electrical activity of the heart. To extend this technology towards a mapping system implementation, a better understanding on how different factors are influencing LI measurements is needed. A 3D model of the ablation catheters with the LI technology was employed in different scenarios reported in the clinics, and in vitro experiments were used to support simulated studies. During this work, the potential capabilities of LI measurements were proven and paved the way towards its use as a surrogate for detection of fibrotic areas in cardiac mapping, complementing commonly used techniques based on electrogram analysis.

ISSN 1864-5933
ISBN 978-3-7315-1368-1

Gedruckt auf FSC-zertifiziertem Papier